

Field driven domain wall dynamics in ferromagnetic nanostripes

Dissertation

zur Erlangung des akademischen Grades

doctor rerum naturalium (Dr. rer. net.)

vorgelegt dem Rat der Physikalisch-Astronomischen

Fakultät der Friedrich-Schiller-Universität Jena

von Dipl. Ing. Sascha Glathe

geboren am 27.12.1981 in Leipzig

Gutachter

1. Prof. Dr. rer. nat. habil. Paul Seidel
2. Prof. Dr. rer. nat. Mathias Kläui
3. Dr. Dan Allwood

Tag der Disputation: 08.12.2011

Ehrenwörtliche Erklärung

Ich erkläre hiermit ehrenwörtlich, dass ich die vorliegende Arbeit selbständig, ohne unzulässige Hilfe Dritter und ohne Benutzung anderer als der angegebenen Hilfsmittel und Literatur angefertigt habe. Die aus anderen Quellen direkt oder indirekt übernommenen Daten und Konzepte sind unter Angabe der Quelle gekennzeichnet.

Bei der Auswahl und Auswertung folgenden Materials haben mit nachstehend aufgeführte Personen in der jeweils beschriebenen Weise unentgeltlich geholfen:

1. Durchführung der Micromagnetischen Simulation in Fig. 2.6 durch M. Zeisberger (IPHT Jena e.V., Jena, Germany).
2. Durchführung der Micromagnetischen Simulationen in Figs. 4.6 und 4.11, sowie Erstellung des Fig. 4.11 a-f durch D.V. Berkov (Innovent e.V., Jena, Germany)

Weitere Personen waren an der inhaltlich-materiellen Erstellung der vorliegenden Arbeit nicht beteiligt. Insbesondere habe ich hierfür nicht die entgeltliche Hilfe von Vermittlungs- und Beratungsdiensten (Promotionsberater oder andere Personen) in Anspruch genommen. Niemand hat von mir unmittelbar oder mittelbar geldwerte Leistungen für Arbeiten erhalten, die im Zusammenhang mit dem Inhalt der vorgelegten Dissertation stehen.

Die Arbeit wurde bisher weder im In- noch im Ausland in gleicher oder ähnlicher Form einer anderen Prüfungsbehörde vorgelegt.

Die geltende Promotionsordnung der Physikalisch-Astronomischen Fakultät ist mit bekannt.

Ich versichere ehrenwörtlich, dass ich nach bestem Wissen die reine Wahrheit gesagt und nichts verschwiegen habe.

Jena, 22.06.2001

Sascha Glathe

Contents

List of Figures	iii
List of Tables	v
List of Symbols and Abbreviations	vi
1 Introduction	1
2 Theoretical Background	5
2.1 Micromagnetism	5
2.1.1 The path to the LLG equation	5
2.1.2 Micromagnetic simulations	9
2.1.3 Domain wall statics	10
2.1.4 Domain wall dynamics	15
2.2 Thin film magnetism	22
2.2.1 Giant magnetoresistance	22
2.2.2 Anisotropic magnetoresistance	24
2.2.3 Direct exchange coupling	25
2.2.4 Oscillatory exchange coupling	26
3 GMR samples	29
3.1 Composition of the GMR stack	29
3.2 Fabrication of the GMR nanostripes	32
3.3 Magneto-resistive characterization of the GMR stack	34
4 Results	37
4.1 Domain wall dynamics	37
4.1.1 Experimental instrumentation	40
4.1.2 Nucleation of a DW	43

4.1.3	Visualization of the Walker breakdown process	46
4.1.4	Splitting of a dynamic DW	55
4.1.5	Influence of an in-plane transverse field on the DW dynamics	61
4.1.6	Influence of the real shape on the DW dynamics	72
4.2	Pinning of DWs	79
4.2.1	Experimental instrumentation	79
4.2.2	Influence of a transverse field on DW pinning.	81
4.2.3	Conclusion	86
5	Summary and Outlook	87
	Bibliography	I

List of Figures

1.1	Schematic of a multiturn counter.	2
1.2	Schematic of domain wall control by a rotating magnetic field.	3
2.1	Formation of magnetic domains and domain walls.	10
2.2	Orientation of a nanostripe in a Cartesian coordinate system.	11
2.3	Phase diagram for domain walls in a nanostripe.	13
2.4	Edge defect theory.	15
2.5	Schematic representation of the DW dynamics of a transverse domain wall in a nanostripe.	17
2.6	Micromagnetic simulation of the dynamics of a transverse domain wall in a nanostripe.	18
2.7	Velocity field dependence according to the 1-d model.	21
2.8	Schematic of the band structure of a ferromagnetic and nonmagnetic metal.	23
2.9	Two channel model of the GMR.	24
2.10	Exchange Bias field	25
2.11	Oscillatory exchange coupling.	26
3.1	Magnetic behavior of spin valves	30
3.2	Schematic of the GMR stack.	31
3.3	TEM image of the GMR stack cross section.	32
3.4	Optical micrograph of a chip	33
3.5	Magneto-resistive characterization of the GMR stack.	34
3.6	Current distribution in the GMR stack.	35
4.1	Definition of the field orientation and schematic of measurement cycle.	40
4.2	Measurement setup for quasi static fields.	41
4.3	Sample measurement of domain wall movement.	42

4.4	Statistics of the nucleation field.	43
4.5	Micromagnetic simulation of the in-plane magnetization direction during the DW nucleation process.	45
4.6	Micromagnetic simulation of the DW dynamics in perfect and rough nanostripes.	47
4.7	Visualization of the Walker breakdown process.	49
4.8	Influence of a transverse field on the Walker breakdown process.	52
4.9	Walker frequency as a function of the applied transverse field for several nanostripe width.	53
4.10	Visualization of the DW splitting	56
4.11	Snapshots of the DW Splitting.	57
4.12	Influence of a transverse field in the static DW profile.	62
4.13	Longitudinal component of the nucleation field in dependence on the applied transverse field.	63
4.14	Dependence of the DW velocity on the applied longitudinal field.	64
4.15	Velocity field dependence for small transverse fields.	65
4.16	Velocity field dependency for intermediate transverse fields.	67
4.17	Single shot measurements of the suppression of the Walker process.	68
4.18	DW mobility as a function of the transverse field.	70
4.19	Possible magnetization configurations for the directions of H_{long} and H_{tr}	73
4.20	Measurement of the influence of slanted edges on the DW dynamics.	74
4.21	Estimation of the stray field energy in the nanostripe edge region.	76
4.22	Stray field energy for slanted edges.	78
4.23	Dark field image of a multiturn chip.	79
4.24	Measurement scheme for the investigations of DW pinning.	80
4.25	Pinning probability in a multiturn sensor.	81
4.26	Depinning fields for a strong pinning site.	82
4.27	Depinning fields and pinning probability in dependence on H_{tr}	83
4.28	Voltage bridge level of pinned DWs.	85

List of Tables

2.1	Energy contributions in a $\text{Ni}_{81}\text{Fe}_{19}$ nanostripe.	7
3.1	Magneto-resistive and magnetic properties of the used GMR stacks for a different nanostripe cross sections.	36
4.1	Specifications of the oscilloscopes.	42
4.2	Walker field and frequency.	50

List of Symbols and Abbreviations

Symbols

A	Exchange stiffness constant.
α	Gilbert damping parameter.
C	Shear Modulus.
χ	Chirality of a vortex domain wall.
d	Thickness of a nanostripe.
Δ	Domain wall width.
E	Energy.
e	Energy density.
e_d	Demagnetizing energy or stray field energy density.
E_x	Exchange energy.
E_d	Demagnetizing energy or stray field energy.
E_{ext}	Zeeman energy due to an external magnetic field.
E_F	Fermi level.
E_k	Magneto crystalline anisotropy energy.
E_m	Magneto-elastic energy.
f_{WBD}	Frequency of the Walker breakdown process.
H_{cr}	Critical field above which a vortex wall is transformed to a transverse wall.
H_d	Demagnetizing field.
H_{eff}	Effective field.
H_{long}	In plane longitudinal magnetic field.
H_{long}^{nuc}	Longitudinal component of the domain wall nucleation field.
H_{nuc}	Nucleation field of a domain wall.
H_{tr}	In plane transverse magnetic field.
H_w	Walker breakdown field - critical field in domain wall dynamics.
J_1	Coupling constant.

l	Length of a nanostripe.
λ	Magnetostrictive constant.
λ_s	Magnetic volume charge density.
Λ	Exchange length.
m	$m = \frac{M}{M_s}$ reduced magnetization.
M	Magnetization.
m_{core}	Reduced core magnetization of a transverse domain wall.
M_s	Saturation magnetization.
μ	$\mu = dv/dH$ mobility of a domain wall.
n	Winding number of a topological defect.
\vec{N}	Demagnetizing tensor.
p	Polarity of a vortex domain wall.
R	Resistivity.
R_{ap}	Resistivity for an antiparallel alignment of the FM layers in a GMR stack.
R_p	Resistivity for a parallel alignment of the FM layers in a GMR stack.
R_{\uparrow}	Resistivity for a majority electron in a FM metal.
R_{\downarrow}	Resistivity for a minority electron in a FM metal.
r	Position vector.
σ_s	Magnetic surface charge density.
t	Time.
T	Period of a Walker breakdown process.
T_C	Curie temperature.
T_N	Néel temperature.
Θ	Domain wall angle.
ϕ	Out of plane angle of the DW core magnetization.
V	Volume.
v	Velocity of a domain wall.
v_w	Walker velocity - velocity of the domain wall at the Walker field H_w .
w	Width of a nanostripe.
X_{GMR}	Ratio of the giant magnetoresistance.
X_{AMR}	Ratio of the anisotropic magnetoresistance.

Acronyms

AAF	Artificial antiferromagnet.
AFM	Antiferromagnet, antiferromagnetic.
AV	Antivortex.
cw	Clockwise rotation.
ccw	Counter clockwise rotation.
CPW	Coplanar waveguide.
DOS	Density of States.
DW	Magnetic domain wall.
DWG	Domain wall generator.
EA	Easy axis.
FFT	Fast Fourier transform.
FM	Ferromagnet, ferromagnetic.
GMR	Giant magnetoresistance.
HA	Hard axis.
HAV	Half antivortex.
HH	Head-to-head.
LLG	Landau-Lifshits-Gilbert equation.
MOKE	Magneto optical Kerr effect.
MR	Magnetoresistance.
NM	Non magnet.
oop	Out-of-plane
PEEM	Photoemission electron microscopy.
Py	Permalloy - alloy composed of Ni ₈₁ Py ₁₉ .
RF	Radio frequency - frequency band between approximately 30 kHz and 300 GHz.
TDW	Transverse domain wall.
TT	Tail-to-tail.
WBD	Walker breakdown process - periodic change in the domain wall configuration, occurring above H_w .
VW	Vortex domain wall.
XMCD	X-ray magnetic circular dichroism.

1 Introduction

Manipulating magnetic domain walls (DW) has been an issue since the early 1930s, when Sixtus and Tonks showed single DW motion for the first time [1, 2]. In a really simple but clever experiment they measured the propagation of a large Barkhausen discontinuity (today know as DW) in a NiFeMn alloy by two pick up coils. From the time delay between the inductions in both coils and their distances they estimated DW velocities between 5 – 400 m/s. This comparable high DW velocities opens the door for implementations in the storage and information technology as the operation speed of possible applications depends on the velocity of a DW.

30 years later the first proposal for an application using magnetic DWs in magnetic wires as key element was given by Spain et al. in the 1960-70s [3, 4]. They proposed a DW logic which is based on DWs moving through magnetic conduits. These conduits where composed of a magnetic softer channel in a hard magnetic material. The channels where fabricated by changing the coercivity of a magnetic thin film (thickness ≈ 150 nm) by the choice of the locally varying under layer. The width of the channels were comparably large with 25 – 100 μm . The problem of these devices was the small operation margins in the range of $H \leq 1$ kA/m.

For the following 20 years the topic of single DW movement in magnetic stripes was out of the scope because of the lack of preparation techniques for much smaller stripes, which would give rise to much larger operation margins. In the course of the improvement of thin film patterning the topic was revived roughly 15 years ago, when it became possible to fabricate magnetic nanostripes in the mesoscopic dimension by electron beam lithography or the focused ion beam technique. Ono et al. showed for the first time DW propagation in sub μm nanostripes [5, 6]. Starting with these experiments the first application of DWs in nanostripes was again a DW logic proposed by Allwood et al. [7, 8]. Here cusps, fan outs and crosses were used to move DWs through a complex system of nanostripes in order to perform logic operations. The DWs were controlled by means of a rotating magnetic field. The characteristics of this type of

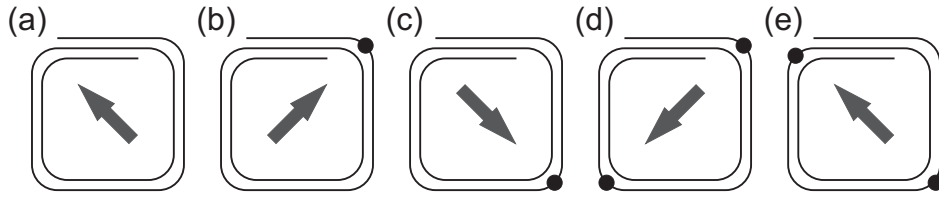


Figure 1.1: Schematic of the functionality for a multiturn counter which is able to count two rotations. The arrow indicate the magnetic field direction and the black circle represent the DW position.

DW control is discussed below.

Today the most popular proposal, for an application of single DW control in magnetic nanostripes, is the racetrack memory proposed by Parkin [9]. Here the DWs are moved through a racetrack like geometry and the domains between the DW store the bits. In contrast to the DW logic the DWs are manipulated and controlled by means of a spin polarized current. As this topic is out of the scope of this thesis, the interested reader is referred to the following references [10–15].

For biological applications DWs can be used to control the position of super paramagnetic nanobeads [16–18]. The nanobeads can be functionalized by e.g. cells or proteins and thus their position can be controlled, too. These devices require a control of the DW position by means of a complex sequence of field [16] or a rotating magnetic field [18].

To the author's knowledge the first implemented application [19], using magnetic DWs as key element, is the so-called multiturn counter [20, 21]. This sensor is able to count the number of rotations of an external rotating magnetic field. Beside the measurement functionality the multiturn sensor also provides a storage functionality, i.e. the sensor works powerless and energy is only required for the read out. Further advantages of the multiturn are the contactless and wearless operation. The multiturn counter consists of a magnetic nanostripe in the shape of a spiral like its shown schematically in Fig. 1.1. The first picture shows a multiturn with no DW in the spiral. If the magnetic field is rotated by 90° , a single DW will be moved into the spiral to the first corner Fig. 1.1b. A further field rotation by 90° displaces the DW to the next corner as shown in Fig. 1.1c. In the next rotation step a new DW is moved into the spiral, and the first DW moves to the next corner again. Thus, for every half turn of the external field a new DW is moved into the spiral. As a consequence the number

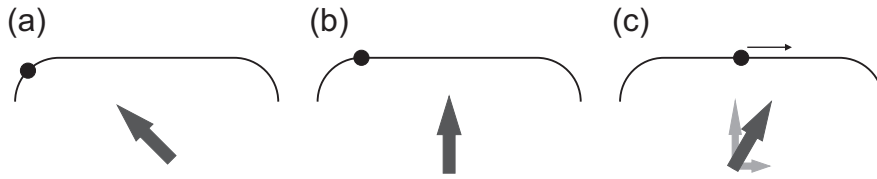


Figure 1.2: Cutout of the multiturn spiral shown in Fig. 1.1. The figure shows a schematic of the DW movement under the influence of a rotating magnetic field. The arrow indicate the magnetic field direction and the black circle represent the DW position.

of rotations of the external field is one-to-one correlated to the number of DWs in the spiral. Using the giant magnetoresistance effect (for explanation see section 2.2.1) the number of DWs in the spiral can be determined.

Concluding, in all applications proposed or realized until now, which rely on field driven DW dynamics, the DWs are controlled by means of a rotating magnetic field. For this type of DW control the magnetic field configuration differs crucially from the one which is typical used for field driven DW dynamics, i.e. a field parallel to the DW propagation direction. The equilibrium position of the DW for a field direction shown in Fig. 1.2a is indicated by the black circles. If the field is rotated by 45° , the DW will move to the intersection of the circular shaped nanostripes and the straight part of the spiral. In order to move the DW in the straight part the external field has to be rotated by a certain angle. However, the DW will move considerable before the magnetic field vector points parallel to the DW propagation direction. Therefore, there are two in-plane field components during DW motion along the nanostripe: a longitudinal and a transverse field.

It was already pointed out, that the experimental studies up to now dealt solely with DW dynamics under the influence of a magnetic field which is parallel to the moving direction of the DWs [5, 6, 22–36]. A detailed experimental analysis concerning the impact of a magnetic field, directed perpendicular to the moving direction of the DW, is lacking. There are up to now only studies using micromagnetic simulations to investigate the influence of such a transverse field on the DW behavior [37–39]. Closing this gap with an experimental study is one of the main concerns of this thesis. Thereby the experimental data will be compared and explained by the few theoretical studies which were given up to now.

Driven by the potential applications there is of course an interest in a fundamental

understanding of field driven DW dynamics. However, most of the present contributions used techniques which required a averaging over many thousand experiments [22–25, 28–35]. As a consequence solely highly periodic phenomena can be investigated by these techniques. Only few papers presented single shot measurements of the DW dynamics [6, 26, 27]. Though the Walker breakdown process, which is a key feature of field driven DW dynamics, could not be investigated by single shot measurements before. Thus, the characterization of the DW dynamics by means of a single shot measurements technique is essential. One target of this thesis is, therefore, the visualization and characterization of the Walker breakdown process by single shot measurements. Beside this, the technique can be used to search and identify new modes of DW motion, that cannot be discovered by averaging techniques.

This thesis is organized as follows. First the basics of magnetism in nanostripes with the geometric feature of large aspect ratios in all three dimensions is explained. Furthermore, thin film phenomena like the giant magnetoresistance effect, the oscillatory exchange coupling and the exchange bias are described phenomenologically in the theory section. In the third section the samples used in the experiments are introduced and characterized. The outcome of this thesis is given in the results section and the paper is closed with a summary and outlook.

2 Theoretical Background

In this chapter the theoretical basis needed to understand this study is given. The first part concentrates on the ferromagnetism in confined geometries in the nanometer range. The focus will be on magnetic nanostripes which have a length of some μm , the width of some hundreds of nm and the thickness of tens of nm. In the second part selected topics of thin film magnetism are explained.

2.1 Micromagnetism

2.1.1 The path to the LLG equation

The theoretical considerations for ferromagnetic materials started at the beginning of the last century with the theory of Weiss [40]. He proposed a model that introduced a molecular force acting on an atom which is produced by the surrounding atoms. This force tries to align the magnetic moment of the atom in parallel to the others and was proposed to be proportional to the number of already aligned atoms. However, the origin of this molecular force was unclear at this time. Nevertheless, this model could explain the remanent behavior of ferromagnets and described the temperature dependence of the magnetization. Several attempts were made to understand the enormous molecular force which could not be explained by a simple dipole interaction. Ising [41] showed that a linear row of atoms with a sufficiently large aligning force between neighboring atoms is not adequate to explain ferromagnetism. In 1928 Heisenberg proposed the exchange interaction by suggesting a interaction between the spins of two neighboring atoms \mathbf{S}_i and \mathbf{S}_j [42]. The energy of this interaction was $E_{ij} = -2J\mathbf{S}_i \cdot \mathbf{S}_j$, whereby J is the exchange integral. This theory could account for the large molecular field, that is necessary for ferromagnetic behavior.

The first step towards today's understanding of magnetic domains (regions of constant magnetization direction) separated by a so-called domain wall (DW) was derived

by Bloch [43] in 1932 and 3 years later by Landau and Lifshits [44]. Landau and Lifshits explained the occurrence of magnetic domains magnetized in opposite direction by the minimization of surface charges and thus stray field energy. Therefore, they concluded that the number of domains depends mainly on the dimensions of the ferromagnetic body. Based on these considerations they came up with the famous Landau pattern (see section 2.1.3). Between these domains they introduced an intermediate region (today known as DW). By minimization of the sum of the exchange and the magnetic anisotropy energy they calculated the magnetization distribution inside the DW and the width of this intermediate region. More generally one should consider the following energy contribution:

- exchange interaction E_x
- demagnetizing or stray field energy E_d
- Zeeman energy due to an external magnetic field E_{ext}
- magneto-crystalline anisotropy energy E_k
- magneto-elastic energy E_m .

In the present study solely soft magnetic layers of Ni₈₁Fe₁₉ (hereafter called Permalloy - Py) are of interest. Because of its small crystalline anisotropy and magneto-elastic energy as compared to the demagnetizing energy (see table 2.1) the last two can be omitted. The following considerations are restricted to the three remaining energies. Thus, the total energy can be written as:

$$E_{tot} = E_x + E_d + E_{ext}. \quad (2.1)$$

The three energy contributions can be calculated as follows:

E_x

The exchange energy arises from any deviation of the magnetic moment direction $\mathbf{m}(\mathbf{r}_i) = \mathbf{M}(\mathbf{r}_i)/M_s$ (M_s - saturation magnetization, $M_s = 800$ kA/m for Py) from the direction of the neighboring moment $\mathbf{m}(\mathbf{r}_{i+1})$. It can be calculated with the exchange stiffness constant A ($A = 1.3 \times 10^{-11}$ J/m for Py) and V as

Table 2.1: Comparison for different energy contributions. The magneto-elastic coefficient is calculated as $K \approx C\lambda^2$ with C and λ as shear modulus and magnetostriction constant, respectively [45]. The material constants for $\text{Ni}_{81}\text{Fe}_{19}$ are taken from [46]. For the calculation of the shape anisotropy see eq. (2.5) and (2.6).

energy contribution	K in J/m^3
magneto-crystalline	10^3
magneto-elastic	10^1
shape anisotropy	10^5

volume by eq. (2.2).

$$\begin{aligned}
 E_x &= A \int (\nabla \cdot \mathbf{m})^2 dV \\
 &= A \int [(\nabla m_x)^2 + (\nabla m_y)^2 + (\nabla m_z)^2] dV
 \end{aligned} \tag{2.2}$$

E_{ext}

The Zeeman energy originates from a deviation of the magnetization in the body from the direction of the external applied field \mathbf{H}_{ext} and can be expressed by eq. (2.3).

$$E_{ext} = -\mu_0 M_s \int \mathbf{H}_{ext} \cdot \mathbf{m} dV \tag{2.3}$$

E_d

The demagnetizing energy is comparably difficult to compute, because of its nonlocal character. It arises from any surface charges $\sigma_s = \mathbf{m} \cdot \mathbf{n}$ (σ_s - surface charge density, \mathbf{n} - surface normal) of the magnetization at the boundary of the samples or from any volume charges $\lambda_s = -\nabla \cdot \mathbf{m}$ (λ_s - volume charge density) due to deviations of the magnetization. One has to solve eq. (2.4) and (2.5) to get the demagnetizing energy. As this can be very complex, the interested reader is referred to Refs. [45, 47] for more information.

$$\nabla \cdot \mathbf{H}_d = -M_s \nabla \cdot \mathbf{m} \tag{2.4}$$

$$E_d = \frac{1}{2} \mu_0 \int_{\text{all space}} \mathbf{H}_d^2 dV = -\frac{1}{2} \mu_0 M_s \int_{\text{sample}} \mathbf{H}_d \cdot \mathbf{m} dV \tag{2.5}$$

Here, the simple case of a uniformly magnetized ellipsoid is treated only. The demagnetizing field can be computed by eq. (2.6) with \vec{N} as demagnetizing tensor. The sum of all components of N is always 1. For the simplest case of a sphere the three components of \vec{N} are $N_x = N_y = N_z = \frac{1}{3}$. For a general calculation of \vec{N} see Ref. [45].

$$\mathbf{H}_d = -M_s \vec{N} \cdot \mathbf{m} \quad (2.6)$$

The summation of (2.2), (2.3) and (2.5) gives the total energy under the assumption of vanishing crystalline anisotropy and magneto-strictive effects:

$$E_{tot} = \int \left[A(\nabla \cdot \mathbf{m})^2 - \mu_0 M_s \left(\mathbf{H}_{ext} \cdot \mathbf{m} + \frac{1}{2} \mathbf{H}_d \cdot \mathbf{m} \right) \right] dV \quad (2.7)$$

To find the distribution of the magnetic moments $\mathbf{m}(\mathbf{r})$ a variational calculus with the condition $\mathbf{m}^2 = 1$ has to be performed (eq. (2.8)). Solving this problem one can define an effective magnetic field H_{eff} (see e.g. [44, 45, 48]) by eq. (2.9), leading to eq. (2.10) with Δ as Laplace operator.

$$\frac{\delta E_{tot}}{\delta \mathbf{m}} = 0 \quad (2.8)$$

$$\mathbf{H}_{eff} = -\frac{1}{\mu_0 M_s} \frac{\delta E_{tot}}{\delta \mathbf{m}} \quad (2.9)$$

$$\mathbf{H}_{eff} = \mathbf{H}_{ext} + \mathbf{H}_d + \frac{2A\Delta\mathbf{m}}{\mu_0 M_s} \quad (2.10)$$

From this point of view the interpretation is straightforward: The effective field has to be zero at every position \mathbf{r} . If this field is $H_{eff} \neq 0$ it exerts a torque on the magnetization in the form of eq. (2.11), whereby $\dot{\mathbf{m}}$ is the derivative with respect to time. Thus, the change of the magnetization $\dot{\mathbf{m}}$ is always perpendicular to the plane of the effective field and the magnetization vector. Here γ_0 (2.12) is the gyromagnetic ratio with e - elementary electric charge, m_e - electron mass, g - Landé-Faktor. For a 20 nm thick Py layer the Landé factor is $g \approx 2$ [49] and the gyromagnetic ratio accounts for $\gamma_0 = 2.21 \cdot 10^5 \frac{\text{m}}{\text{As}}$.

$$\dot{\mathbf{m}} = -\gamma_0 \mathbf{m} \times \mathbf{H}_{eff} \quad (2.11)$$

$$\gamma_0 = \frac{\mu_0 g e}{2m_e} \quad (2.12)$$

Dynamically spoken the magnetization rotates around the effective field, or in other words the magnetization performs a gyrotropic motion. Solely this torque will not cause the parallel alignment of \mathbf{m} and \mathbf{H}_{eff} (with the consequence $H_{eff} = 0$). The damping towards the direction of the effective field during this precession was added to the equation by Landau and Lifshits by a term treating the "approach of s [in our notation M] to f [in our notation \mathbf{H}_{eff}]" [44]. The resulting vector is directed from the magnetization \mathbf{m} to the effective field \mathbf{H}_{eff} . 20 years later Gilbert reformulated the Landau-Lifshits formula and introduced a new phenomenological damping parameter α ([50], this reference is not available, see [51] instead), which is nowadays named after him. The need for a new damping formulation arose from the fact that the original damping term given by Landau and Lifshits could only be used for weak damping.

The result of the considerations in this section is the so-called Landau-Lifshits-Gilbert (LLG) eq. (2.13) which is the commonly used micromagnetic equation for quasi-static as well as dynamic calculations.

$$\dot{\mathbf{m}} = -\gamma_0 \mathbf{m} \times \mathbf{H}_{eff} + \alpha \mathbf{m} \times \dot{\mathbf{m}} \quad (2.13)$$

Here, the first term at the right side induces a rotational motion of the magnetic moment around the effective field as long as $\mathbf{m} \neq \mathbf{H}_{eff}$ and the second term damps this rotation in the direction of the effective field.

2.1.2 Micromagnetic simulations

The LLG equation (2.13) can be solved numerically by means of micromagnetic simulations. In this thesis the commercially available program MICROMAGUS was used [52]. The material parameters were those of Py, namely $M_s = 800 \text{ kA/m}$, $A = 1.3 \times 10^{-11} \text{ J/m}$ and $\alpha = 0.01$, with zero crystalline anisotropy and magnetostriction. The cell discretization was $10 \times 5 \times 5 \text{ nm}^3$ if not stated differently. I performed quasistatic simulations, to find a magnetization configuration with a (not imperative global) energy minimum. The dynamic simulations, including the temporal evolution

of the magnetization components, were performed by M. Zeisberger (IPHT e.V. Jena, Germany) or D.V. Berkov (Innovent e.V. Jena, Germany) using a cluster with 64 nodes.

2.1.3 Domain wall statics

In this section I will first treat the magneto-statics, i.e. I will deal with the energy minimum of a magnetic vector field. In terms of the previously defined effective field the energy minimum is reached with a magnetic distribution which satisfies $H_{eff} = 0$.

Kittel reviewed in 1949 the origin of magnetic domains and DW in ferromagnetic crystals [53]. According to eqs. (2.4) and (2.6) an uniformly magnetized ferromagnetic body (e.g. Fig. 2.1a) generates a stray field energy density in the order of $e_d = \frac{\mu_0}{2} N M_s^2 \approx 10^5 \text{ J/m}^3$ (N as demagnetizing factor in the direction of the magnetization). In order to reduce this energy one can add another domain (see Fig. 2.1b) with a DW in between. The magneto-static energy density e_d is approximately halved (for a calculation see e.g. [45]) and an additional DW energy density of the order of $e_{dw} = 2\pi\sqrt{AK_u} \approx 7 \times 10^{-4} \text{ J/m}^2$ is needed (for K_u the magneto-crystalline anisotropy energy from table 2.1 is used): the total energy decreases drastically. Fig. 2.1c shows a possibility to avoid any surface charges: the Lifshits-Landau pattern proposed in 1935 [44].

In conclusion the occurrence of magnetic domains and domain walls in between is driven by the minimization the two competing energies: demagnetizing and DW energy.

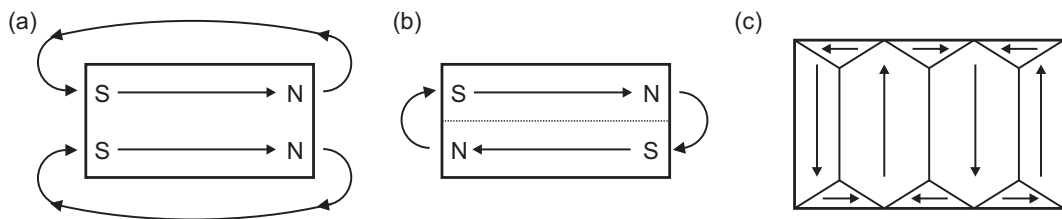


Figure 2.1: (a) Uniformly magnetized body with the stray field emanating from the magnetic poles. (b) Reduction of the stray field for the two domain state. (c) Landau-Lifshits pattern with no stray field.

It has already been stated that this study will be restricted to magnetic phenomena in so-called nanostripes with the geometric property $l \gg w > d$ (l - length, w - width, d - thickness). Fig. 2.2 shows the orientation of such a nanostripe in a Cartesian coordinate

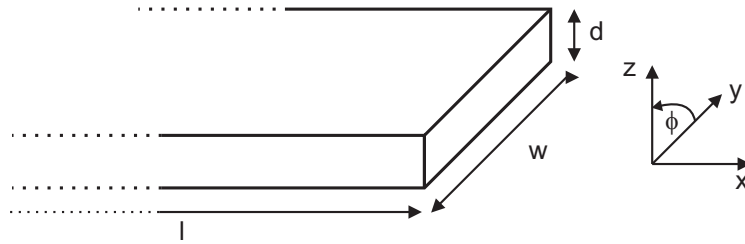


Figure 2.2: Orientation of the nanostripe in a Cartesian coordinate system and definition of the out-of-plane angle ϕ .

system as it will be used in this report. Due to the large aspect ratios $\frac{l}{w}$ and $\frac{w}{d}$, there are large demagnetizing fields and, therefore, large energy increases for any deviation from a magnetization parallel to the x -axis. This gives rise to a strong shape anisotropy. The demagnetizing factors for such a geometry are given by Porter et al. [54] with equation (2.14) and (2.15) whereby $N_x = 0$ because of $l \gg w$. For an aspect ratio of $w/d = 8$ one obtains $N_z \approx 0.9$, $N_y \approx 0.1$.

As the demagnetizing field in the x -direction is zero (see eq. (2.6)), the magnetization will be parallel to this axis in the ground state. Thereby it can point in the positive or negative x -direction. The reversal of the magnetic moments between these two energy minima is not done by coherent rotation of all magnetic moments, in order to avoid large stray fields. The magnetization direction is reversed by nucleation of a DW at one end of the nanostripe and the propagation of this DW through the nanostripe. The DW separates two magnetic domains which are magnetized antiparallel to each other. Accordingly there will be a 180° DW in the nanostripe, so that the magnetic moment rotates by 180° inside the DW.

$$N_y(w, t) = 1 - \frac{2}{\pi} \arctan\left(\frac{w}{t}\right) + \frac{1}{2\pi} \frac{t}{w} \log\left(1 + \left(\frac{w}{d}\right)^2\right) - \frac{1}{2\pi} \frac{w}{d} \log\left(1 + \left(\frac{t}{w}\right)^2\right) \quad (2.14)$$

$$N_z(w, t) = N_y(t, w) \quad (2.15)$$

For the abovementioned thickness ($d = 20$ nm) of ferromagnetic layers one expects so-called Néel walls as stable DW structure [45]. In 1997 Donahue et al. calculated

the stable DW configuration for Py, neglecting any magneto-crystalline and magneto-strictive energies [55]. They found two stable DW types, a transverse DW (Fig. 2.3b) and a vortex wall (Fig. 2.3d), hereafter abbreviated by TDW and VW, respectively.

The transverse wall is characterized by a transverse magnetized core region with a nearly triangular shape. The wider part of the triangle is on the edge of the nanostripe where the magnetic flux lines are closed. In Fig. 2.3b this is at the upper edge, where the three heads of the arrows meet. It is obvious that a large stray field is generated at this edge. The magnetization in a VW (Fig. 2.3d) curls around the center of the vortex where the magnetization points out-of-plane (oop) in the $\pm z$ -direction. This configuration costs more exchange energy compared to the TDW, but this is compensated by the gain in E_d . In larger nanostripes with enough space for the formation of a vortex, this wall type is energetically more stable. For smaller ones the angle between adjacent spins would be larger because of the lesser space. As a result the exchange energy required to build a VW would overcome the strayfield energy of a TDW which is the preferred DW type in small nanostripes. For an analytical calculation of the phase boundary see [55].

The calculated phase diagram was refined by Nakatani et al. [56]. It includes a region for an asymmetric transverse DW (Fig. 2.3c) and is shown in Fig. 2.3a. One finds a phase boundary between a VW and a TDW for $d = 61.3 \times \Lambda^2/w$. According to Ref. [45] the exchange length Λ is defined with eq. (2.16) and accounts for $\Lambda = 5.69$ nm with typical values for Py ($M_s = 800$ kA/m, $A = 1.3 \times 10^{-11}$ J/m).

$$\Lambda = \sqrt{\frac{2A}{\mu_0 M_s^2}} \quad (2.16)$$

Recently the phase diagram was experimentally verified by Laufenberg et al. [57]. They reported, however, that the experimentally found phase boundary is shifted to higher width and thicknesses as compared to the theory. They explained this behavior with metastable local energy minima for TDW. In the experiment they first saturated a nm-sized ring by means of an external field and they released the field subsequently, so that the magnetic ring could relax. After relaxation the ring will be in the so-called onion state containing two DWs [58]. Owing to the large field necessary for the saturation of the ring two TDW will be present when the field is applied. These TDWs could remain in a metastable state after the field was removed. Even though the VW would

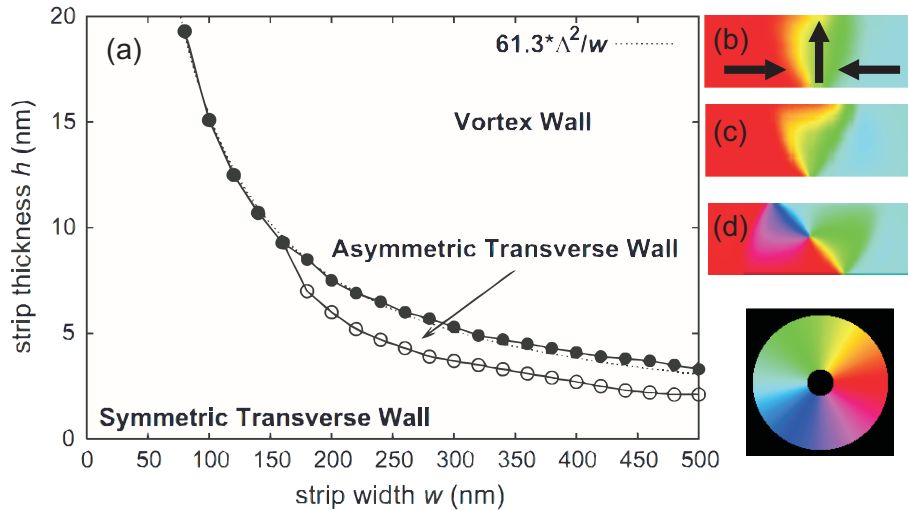


Figure 2.3: (a) Phase diagram of the DW structure in Py nanostripes as a function of the stripe thickness (denoted as h in this graph) and width. Source: [56] (b) Transverse domain wall in a $5 \times 100 \text{ nm}^2$ nanostripe. (c) Asymmetric transverse domain wall in a $5 \times 250 \text{ nm}^2$ nanostripe. (d) Vortex domain wall in a $5 \times 500 \text{ nm}^2$ nanostripe. The magnetization directions are visualized by the color wheel. The micromagnetic simulations for b,c,d were performed with a cell discretization of $5 \times 5 \times 5 \text{ nm}^3$ using [52].

be in a lower energy state, a TDW can be stable if there is an energy barrier between the metastable state and the energy minimum.

Note that the TDW pictured in Fig. 2.3b is a head-to-head (HH) DW. An energetically equal configuration would be a tail-to-tail (TT) DW, where the arrows in the domains (representing the magnetic moment of the domains) point away from each other. Moreover, the direction of the magnetic moment in the TDW core region can be in positive or negative y -direction. Thus, we have 4 different energetically equal configurations of a TDW (requirement is an external field of $H_{ext} = 0$). For the VW one gets even more possibilities. Beside the domain magnetization (HH or TT DW) a VW is characterized by its chirality $\chi = \pm 1$ (clockwise - cw or counterclockwise - ccw rotation of the magnetic moments) and polarity $p = \pm 1$ (direction of the core magnetization in $\pm z$ -direction). In total one gets 8 different VWs which are energetically degenerated in zero external field.

An important parameter of DW dynamics is the width DW Δ . A simple analytical expression is given by $\Delta = \pi \sqrt{A/K}$. Here K is the anisotropy constant which is in

our case equal to the shape anisotropy and thus $K_d = N_y \mu_0 / 2M_s^2$. For a permalloy nanostripe with a cross section of $w/d = 8$ one gets a DW width of $\Delta \approx 50$ nm. However, the exact description of the width is difficult, owing to the complex 2-dimensional spin structure of TDWs or VWs. For example the triangular profile of a TDW (see Fig. 2.3b) hinders a definition of a wall width. One possibility is the calculation of the magnetization in the x and y averaged over the y -position. This was discussed by Thiaville et al. [48] and one finds different DW widths for both magnetization components. This again shows the difficulty of an exact description of Δ . A detailed theoretical treatment of the DW width can be found in [45].

Kläui [59] derived Δ experimentally from a fit of the m_x along the x -axis. The magnetization was determined by electron holography [60] and XMCD-PEEM (X-ray magnetic circular dichroism - photoemission electron microscopy) [61] and the magnetization was averaged across the nanostripe. It was shown that the DW width approximately scales with the nanostripe width.

Edge defect theory

Another approach to describe a DW was given by Tchernyshyov et al. [62–64]. They proposed the assembling of a DW by topological defects, i.e. edge defects and topological charges in the bulk. These defects are described by means of a winding number n which can have values of ± 1 for bulk defects and $\pm \frac{1}{2}$ for edge defects. Fig. 2.4 shows the magnetic configuration for these winding numbers. The winding number of $n = +\frac{1}{2}$ corresponds to an edge defect, that can be named with half antivortex (HAV). The magnetic moments around the core of the HAV are all pointing to and away from the core, respectively. It is noteworthy that the core of a HAV is outside the nanostripe, so that the magnetization is still in plane, contrary to the oop magnetization of a full vortex or antivortex. Accordingly there are edge defects with $n = -\frac{1}{2}$, which is shown in Fig. 2.4b. These also consist of three magnetic moments arranged around a HAV, however, only two moments point towards or away from the core and the third one points in the opposite direction. For the case of $wd < \Lambda^2$ both edge defects are energetically equal. For the more realistic cases of $wd \geq \Lambda^2$ and $wd \gg \Lambda^2$ the demagnetizing energy breaks the symmetry and the edge defect with the positive winding number contains more stray field energy than the negative one. A TDW like in Fig. 2.3b is a composition of these both defects. The positive winding is always located at

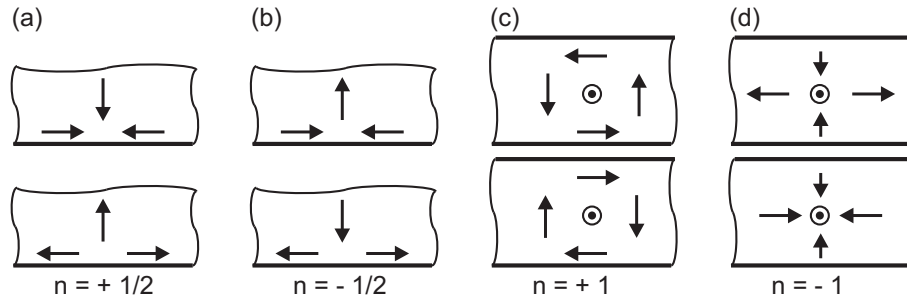


Figure 2.4: Magnetic configuration for the different winding numbers. The magnetization direction is visualized by the arrows. (a) $n = +\frac{1}{2}$ - half antivortex with three arrows pointing towards or away from the core. (b) $n = -\frac{1}{2}$ - half antivortex with two arrows pointing towards or away from the core, and one arrow pointing in the other direction. (c), (d) $n = +1$ and $n = -1$ - vortex and antivortex, respectively, each with any of the 8 possible magnetic configurations. Two of these are schematically depicted.

the wider side of the triangular shaped wall and the negative n sits at the apex.

The two remaining defects are volume charges. Fig. 2.4c shows two possibilities of the vortex having a positive winding number of $+1$. All eight possible magnetization configurations of a vortex (core polarity, chirality and domain magnetization direction) have the same winding number. The last defect is the antivortex, having a winding number of $n = -1$, whereby the exact magnetic configuration of the antivortex is nonrelevant, too. Two of the possible magnetization configuration for an antivortex are shown in Fig. 2.4d.

According to Tchernyshyov [63] the sum of all winding numbers in a nanostripe has to be zero. Now it is immediately clear that the VW shown in Fig. 2.3d cannot only consist of a vortex with a winding number of $+1$. There are two edge defects with $n = -\frac{1}{2}$ at the edges of the nanostripe, so that the sum of all winding numbers is zero $\sum n_i = 1 + 2 \times (-\frac{1}{2})$. The same holds for the antivortex, where additionally two edge defects with a positive winding number are required.

2.1.4 Domain wall dynamics

In the following section I want to cover the DW dynamics, whereby the considerations are restricted to the dynamics of TDWs and VWs in nanostripes. The starting point for the upcoming considerations is a DW in a nanostripe (the creation of this DW will be treated later) and an applied field in the x -direction.

In 1974 Walker et al. [65] derived a 1-d model from the LLG eq. (2.13). This model describes the qualitative features of the DW dynamics with three characteristic regimes: First, a low field regime, where the DW velocity is approximately linear dependent on the applied external field. Above a critical field, the so-called Walker field H_w , the time-averaged velocity decreases. In this regime the DW movement oscillatory and periodic. In even higher fields $H \gg H_w$ the DW movement is not any more periodic but becomes chaotic. These principle features hold for both DW types, TDW and VW. However, there are of course some differences which will be explained in the following sections.

Transverse wall

In this section I will explain the dynamics of a TDW in a nanostripe. We start with a situation shown in Fig. 2.5a and apply a field in the positive x -direction. According to eq. (2.11), the external field H_{ext} exerts no torque on the magnetization in the domains which is parallel and antiparallel to H_{ext} , respectively. The magnetization in the TDW core region is, however, perpendicular to the external field and a torque in the negative z -direction is induced (blue arrow in Fig. 2.5b). This torque causes a tilt of the magnetization in this direction, generating a locally confined but large demagnetizing field $H_{dem}^z = -N_z M_s \sin \phi$ (for a definition of the oop angle ϕ see Fig. 2.2, $N_z = 0.9$ for a typical aspect ratio of $w/d = 8$). The effective field \mathbf{H}_{eff} is dominated by H_{dem}^z and points in the positive z -direction. This field exerts a torque on the y -projection of the TDW core magnetization m_y and points in the positive x -direction (see Fig. 2.5c). As a consequence the magnetization is rotated in the direction of the applied external field and the DW moves along the x -direction as it is shown in Fig. 2.5d. Note that the actual driving field of the DW is the large demagnetizing field in the z -direction which gives rise to very large velocities in the range of 100 m/s [23].

To leave the simple picture of DW dynamics drawn in Fig. 2.5, a micromagnetic simulation of the dynamics of a DW below the Walker field is shown in Fig. 2.6a-d. The colored panels show the direction of in-plane magnetization according to the color wheel and the gray panels show the oop magnetization with a positive and negative z -direction coded in white and black, respectively. The configuration is the same as in Fig. 2.5a. The oop magnetization at the position of the TDW is clearly observed. Contrary to the simple sketch in Fig. 2.5 ϕ is constant during DW motion (see Figl.

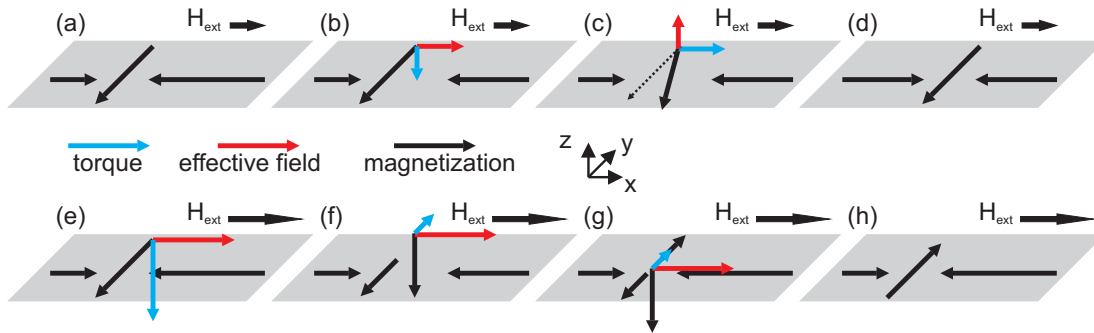


Figure 2.5: Schematic representation of steps occurring during the DW dynamics of a TDW for (a-d) $H < H_w$ and (e-h) $H > H_w$.

2.6c and d). However, the constant oop angle is obviously not achieved immediately after the application of the field. There is clearly a difference in the oop magnetization between 0.2 ns, 1.1 ns and 1.9 ns suggesting a acceleration period of the DW (the velocity of the DW depends on the oop magnetization) and thus an inertia of the DW.

As one increases H_{ext} , ϕ becomes larger, increasing H_{dem} and thus the velocity of the DW. From these considerations it is immediately obvious that there is a critical field above which the situation changes: if the external field equals the critical Walker field H_w , the maximum oop magnetization is reached. For the following considerations we have to take account of the 3-d character of the DW. The oop angle ϕ is not constant along the y -axis in the TDW core region. It is largest at the apex of the TDW at the position of the HAV with a negative winding number $n = -\frac{1}{2}$. This can be seen in Fig. 2.6c and d. If the maximum oop angle $-\pi/2$ is reached at this edge of the nanostripe, a antivortex (AV) core exists (Figs. 2.5f and 2.6g). Using micromagnetic simulation Choi et al. showed that the critical diameter of this vortex core is approximately equal to the exchange length Λ which is ≈ 5 nm in Py [66]. As there is no m_y -component of the magnetization ($m_z = -1$) the large demagnetizing field generated by the vortex core cannot exert a torque on the magnetization. Thus, the effective field acting on the AV core is still determined by H_{ext} which points in the $+x$ -direction. The torque, exerted by H_{ext} and acting on the core, points towards the positive y -direction pushing the AV in the nanostripe (Figs. 2.5g and 2.6g-i). The corresponding force is also-called the gyrotropic force [48]. The chirality of the TDW changes after the AV has left the nanostripe at the other edge as it can be seen from a comparison of Figs. 2.5a and h and 2.6e and k, respectively.

It is worth mentioning that the DW does not effectively move in the x -direction

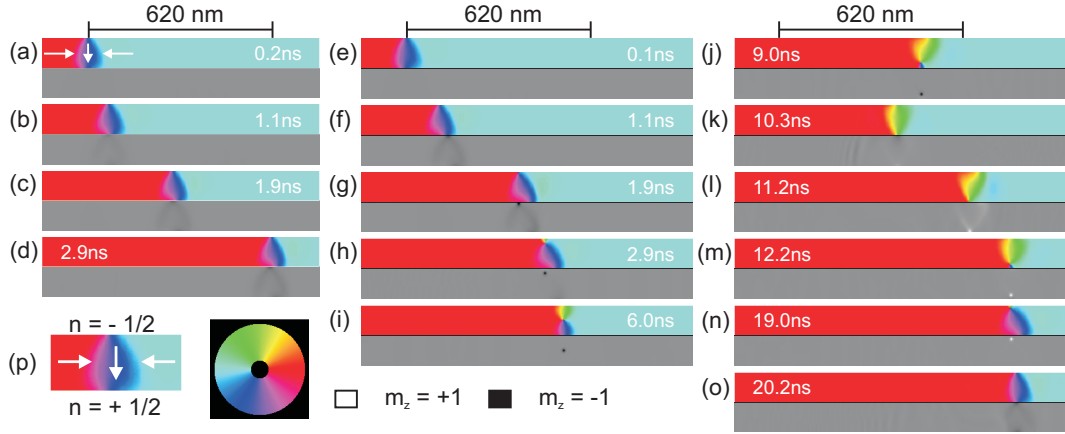


Figure 2.6: Micromagnetic simulation of the DW dynamics in a $5 \times 100 \text{ nm}^2$ nanostripe (cell discretization $5 \times 5 \times 5 \text{ nm}^3$) of a TDW for (a-d) $H = 0.8 \text{ kA/m} < H_w$ and (e-o) $H = 1.6 \text{ kA/m} > H_w$. (p) shows a blow up of the DW from (a) and the positions of the HAVs with its winding numbers are indicated according to the edge defect theory. The colored panel shows the in-plane magnetization direction corresponding to the color wheel, and the gray panels show the oop magnetization with black and white pointing in the negative and positive z -direction, respectively.

during the crossing of the antivortex. Up to the middle of the nanostripe the core moves forward (Fig. 2.6h-i), but from the middle to the lower edge of the nanostripe the core moves backwards again (Fig. 2.6i-k). Before and after this process the DW is approximately at the same position as can be seen by comparing Fig. 2.6g and k.

Now $|\phi|$ starts to increase again, accelerating the TDW in the x -direction. However, the torque is now directed in the positive z -direction and thus ϕ becomes positive, see Fig. 2.6l. If $\phi = \pi/2$ (Fig. 2.6m) a new antivortex is nucleated at the opposite edge of the nanostripe and with an opposite polarity as compared to Fig. 2.6g. Under the influence of the external field the core crosses and leaves the nanostripe, reversing the chirality of the TDW again to the starting configuration of Figs. 2.5a and 2.6e. This process, which is named after Walker - the Walker breakdown process (WBD) - is repeated periodically.

In comparison of Fig. 2.6a, c and e, g one can see, that the TDW is faster as the field is higher. However, due to the periodic Walker process the mean velocity of the DW significantly reduces for fields $H_{ext} > H_w$. Below H_w the TDW needs 2.9 ns for the marked 620 nm (Fig. 2.6d) and above H_w the TDW travels nearly four times longer for

the same distance Fig. 2.6l.

The theory of the topological defects composing the DW can be adopted to the Walker breakdown process very well. As explained in 2.1.3 the TDW is composed of two winding numbers of $n_1 = +\frac{1}{2}$ and $n_2 = -\frac{1}{2}$ like it is indicated in Fig. 2.6p. As the antivortex possesses a winding number of -1 it will be nucleated at the edge defect with a winding number of $-\frac{1}{2}$, namely the HAV at the upper edge, creating an edge defect with $n = +\frac{1}{2}$ at this edge. Thus, the sum of the winding numbers is still zero $\sum n = -1 + 2 \times \frac{1}{2}$ as it can be seen in Fig. 2.6i.

The antivortex appears only in small structures. For $wt > 4000 \text{ nm}^2$ vortex walls will be nucleated during the Walker process [67]. The Vortex wall has a positive winding number of $+1$ and thus it will be nucleated at the other edge where $n = +\frac{1}{2}$. The path of the vortex wall through the nanostripe is contrary to the antivortex first backwards (until the vortex wall reaches the middle of the nanostripe) and then forward [67].

1-D model The 1-d model derived by Walker [65] treats the core magnetization of the TDW as a macrospin and describes the dynamics of a TDW with three parameters: The DW width Δ , the out-of-plane angle ϕ and the DW position in the nanostripe q . I will only give the important equations of this model. Their derivation from the LLG eq. (2.13) can be found in e.g. [48, 65, 68].

The critical Walker field above which the periodic motion of the DW starts can be calculated by:

$$H_w = \frac{\alpha}{2} H_k^z = \frac{\alpha}{2} M_s (N_z - N_y) \quad (2.17)$$

The Walker field depends strongly on the shape of the nanostripe (for a calculation of N_z and N_y see equations (2.14) and (2.15)). The larger the transverse anisotropy field in the z -direction H_k^z the larger the Walker field is. This can be understood by the higher field required to turn the magnetization out-of-plane if the transverse anisotropy is larger.

For the regime below the Walker field ($H_{ext} < H_w$) one gets an equilibrium oop angle ϕ^* for a constant field which reads:

$$\sin 2\phi^* = \frac{H_{ext}}{H_w}. \quad (2.18)$$

The critical oop angle at $H_{ext} = H_w$ is $\phi = \frac{\pi}{4}$ for this 1-d model. As explained

above, the DW motion is in a steady-state regime below H_w and the constant velocity $v = \dot{q}$ is determined by:

$$\dot{q} = \frac{\gamma_0}{\alpha} \Delta(\phi^*) H_{ext}. \quad (2.19)$$

According to the previous section there is no equilibrium value of ϕ for $H > H_w$, but it precesses with a period T given by (2.20). The higher the field above the Walker field the smaller the period of the Walker process is.

$$T = \frac{2\pi(1 + \alpha^2)}{\gamma_0 \sqrt{H_{ext}^2 - H_w^2}} \quad (2.20)$$

The sharp drop of the mean velocity $\langle \dot{q} \rangle$ above H_w can be reproduced by eq. (2.21) [48].

$$\left\langle \frac{\dot{q}}{\Delta} \right\rangle = \frac{\gamma_0 H_{ext}}{\alpha} - \frac{\gamma_0}{\alpha(1 + \alpha^2)} \sqrt{H_{ext}^2 - H_w^2} \quad (2.21)$$

For $H_{ext} \gg H_w$ we get a linear dependence of the velocity and the field again.

$$\dot{q} \approx \frac{\gamma_0}{\alpha + \alpha^{-1}} \Delta H_{ext} \quad (2.22)$$

Comparing equations (2.19) and (2.22) one finds a difference of the DW mobility $\mu = d\dot{q}/dH_{ext}$ of α^2 for $\alpha \ll 1$ for the two linear regimes. The dependence of the velocity on the applied field is shown in Fig. 2.7 in a double logarithmic plot for $\alpha = 0.1$. The curve was plotted using equations (2.19), (2.21) and (2.22). The velocity is normalized to the Walker velocity v_w , the velocity calculated with (2.19) for $H_{ext} = H_w$.

This graph very well reveals the three characteristic features of DW dynamics. However, it only gives a qualitative explanation of the dynamics. Quantitatively the 1-d model can only be used for nanostripes with $w \cong \Lambda$ and $d < w$, where the approximation of the DW as one macrospin is completely fulfilled. This constraint is violated above the Walker field, where an antivortex is present. This two dimensional magnetic structure cannot be described with the 1-d model. Moreover, mostly the experimentally used nanostripes are much larger than the exchange length Λ .

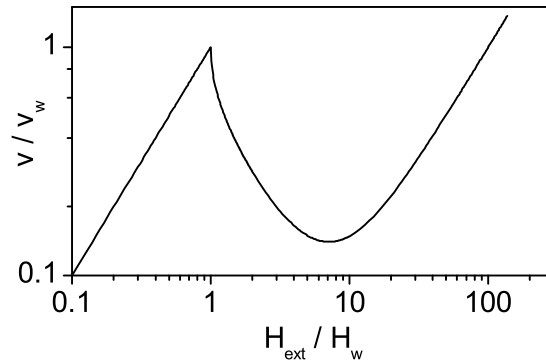


Figure 2.7: Velocity field dependence calculated with equations (2.19), (2.21) and (2.22) for $\alpha = 0.1$ in a double logarithmic plot.

Vortex wall

The dynamics of VWs above the Walker field are identical to the above described dynamics of a TDW. However, one will find a VW during the Walker breakdown process and not an AV. There is only a difference in the behavior between both walls below H_w . Starting with a VW having its core in the middle of the nanostripe (see e.g. Fig. 2.3d) an external field will exert a gyrotropic force on the VW core, pushing the core outwards of the nanostripe. The driving force of the VW in the x -direction stems from the deformation of the VW as the core is moving away from its energetic minimum in the middle of the nanostripe [48]. As it has already been stated in 2.1.4 the VW core moves forwards (with respect to the direction of the applied H_{ext}) when it passed the middle of the nanostripe and therefore leaving the potential well. The more the VW core departs from the middle position the faster the VW moves in the x -direction. But the highest velocity of a VW is much slower compared to the TDW [48].

The VW core eventually leaves the nanostripe if a field larger than a critical field $H_{ext} > H_{cr}$ is applied. In general this critical field is smaller than the Walker field, so that there is a field region below the Walker field where a TDW is dynamically stable, although a VW is stable in the ground state. In conclusion, a VW is dynamically stable only for $H_{ext} < H_{cr}$. For $H_{ext} > H_{cr}$ the dynamics are the same as discussed in the previous section 2.1.4.

2.2 Thin film magnetism

In this section the magnetism of thin films will be treated. It will, however, only cover the phenomena which are important for this study, i.e. giant magnetoresistance, oscillatory exchange coupling and direct exchange coupling. Even though the anisotropic magnetoresistance is not limited to thin films it will be treated in this section, too. Thereby these topics will mostly be described phenomenologically, because a theoretical treatment would go beyond the scope of this thesis.

2.2.1 Giant magnetoresistance

The giant magnetoresistance (GMR) effect was discovered in 1988 independently by the groups of Grünberg and Fert [69, 70] in Fe/Cr multilayers. They found that a parallel alignment of the Fe layers gives a significant lower resistance of the stack as compared to an antiparallel alignment. The change in resistance X_{GMR} can be expressed by eq. (2.23) with the resistance R_p (R_{ap}) in a parallel (antiparallel) alignment of the FM layers.

$$X_{GMR} = \frac{R_{ap} - R_p}{R_p} \quad (2.23)$$

Several theoretical treatments of this phenomenon followed after the discovery (e.g. [71–74]). The models are based on the assumption of spin dependent scattering of the spin polarized electrons at the interface between the FM and the non magnet (NM) as well as in the FM layers. The existence of spin dependent scattering in FM can be understood by means of the density of states (DOS) of a FM. Fig. 2.8 shows the DOS schematically for Ni as a FM metal (a) and a NM metal (b). For Ni the d-bands are shifted with respect to each other by E_x due to the exchange interaction of the d electrons. For the majority spin band the entire $d\uparrow$ -band is below the Fermi level and thus completely filled with electrons, whereby in the minority band the $d\downarrow$ -band is only partly filled at E_F . As a consequence the conduction $s\uparrow$ -electrons in the majority band cannot be scattered in the fully occupied $d\uparrow$ -band. However, the $s\downarrow$ -electrons of the minority spin band can be scattered in the partially unoccupied $d\downarrow$ -band, giving rise to a higher effective mass of these electrons at the Fermi level. Therefore, the resistivity of the minority spin electrons is higher as compared to the majority spin electrons $R_\uparrow < R_\downarrow$. The same holds for the transition of an electron from NM layer to a FM

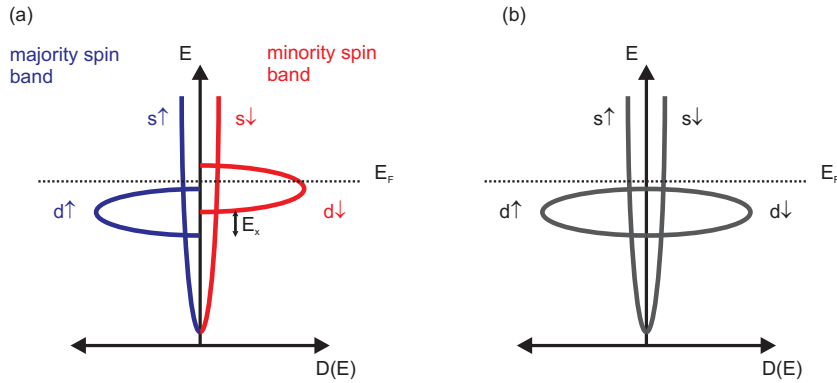


Figure 2.8: Schematic of the band structure of a (a) Ni and a (b) Cu as NM metal.

layer, as one can see in comparison of the DOS of both metals in Fig. 2.8a,b. Note, that the GMR effect is dominated by the spin dependent scattering at the magnet/nonmagnet interface.

Neglecting any spin flip processes in the NM layer (the spin flip length of e.g. a Cu layer is larger than its thickness [75]) one can assume two parallel channels of different resistances for the two spin directions. Fig. 2.9 illustrates this two channel model, which was first introduced by Mott [76], for a FM/NM/FM sandwich. For clearness the GMR stack is depicted in the CPP (current perpendicular to plane) geometry, whereas in this study the CIP (current in plane) geometry will be used.

For a parallel alignment of the FM layers (Fig. 2.9a) the spin-up electron (blue) is the majority electron in both FM layers giving rise to a small resistance R_{\uparrow} in both layers and consequently the spin-down electron (red) is the minority electron giving rise to a high resistance R_{\downarrow} . The total resistance is given by $R_p = (\frac{1}{2R_{\uparrow}} + \frac{1}{2R_{\downarrow}})^{-1} = \frac{2R_{\uparrow}R_{\downarrow}}{R_{\uparrow}+R_{\downarrow}}$ and is for $R_{\uparrow} < R_{\downarrow}$ determined by the smaller R_{\uparrow} ($R_p \approx 2R_{\uparrow}$).

For the case of antiparallel alignment of the FM layers (Fig. 2.9b) both electrons are the majority electron in one layer and the minority electron in the other layer. The total resistance is, therefore, $R_{ap} = \frac{1}{2}(R_{\uparrow} + R_{\downarrow})$, which is, again for $R_{\uparrow} < R_{\downarrow}$, significant larger as compared to R_p . Using eq. (2.23) the GMR ratio can be expressed as eq. (2.24), which is positive for $R_{\uparrow} < R_{\downarrow}$.

$$X_{GMR} = \frac{(R_{\downarrow} - R_{\uparrow})^2}{4R_{\uparrow}R_{\downarrow}} \quad (2.24)$$

In such a three layer system shown in Fig. 2.9 the resistance R of this stack depends

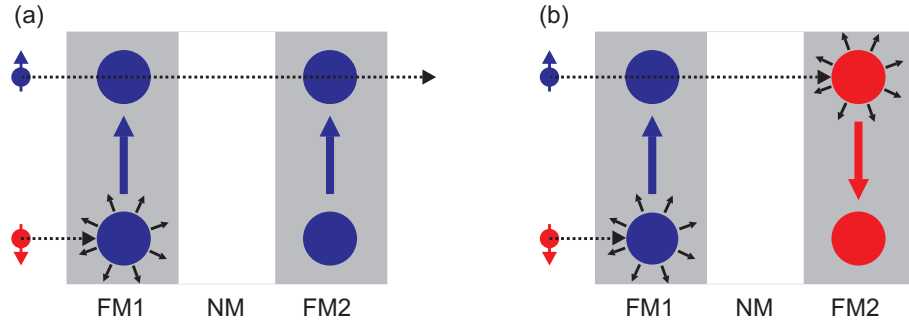


Figure 2.9: Model of the GMR effect in the CPP geometry. (a) Parallel alignment of the two FM layers and (b) antiparallel alignment of the Fm layers

on the angle between the magnetization of the two magnetic layers $\angle(\vec{m}_{FM1}, \vec{m}_{FM2})$. R can be calculated by eq. (2.25) [74], having its maximum and minimum value for $\angle(\vec{m}_{FM1}, \vec{m}_{FM2}) = \pi$ and 0, respectively.

$$R = R_p + \frac{(R_{ap} - R_p)}{2} [1 - \cos \angle(\vec{m}_{FM1}, \vec{m}_{FM2})] \quad (2.25)$$

2.2.2 Anisotropic magnetoresistance

In ferromagnetic layers another effect occurs, which is named anisotropic magnetoresistance (AMR). It is, however, not restricted to multilayer, as e.g. the GMR. The AMR was discovered in the 19th century by Thomson [77]. A different conductivity of iron was observed, depending on the direction of the magnetization of the FM and the direction of the electric current flow: namely a higher resistance for parallel arrangement ρ_l and a lower resistance $\rho_p < \rho_l$ for perpendicular directions of \vec{m} and \vec{j} .

The total resistance can be expressed as a function of the angle between the current and the magnetization [78]:

$$\rho = \rho_l - (\rho_l - \rho_p) \sin^2 \angle(\vec{j}, \vec{m}). \quad (2.26)$$

A theoretical treatment of this effect can be found in e.g. [78] and the references herein.

2.2.3 Direct exchange coupling

The direct exchange coupling was discovered in 1956 by Meiklejohn and Bean [79–81] in ferromagnetic cobalt nanoparticles with an antiferromagnetic cobalt oxide shell. They described this phenomenon as a new unidirectional anisotropy of the ferromagnetic material, giving rise to a shift of the hysteresis loop, which is schematically shown in Fig. 2.10a. For a ferromagnetic material one expects a hysteresis loop shown in the black curve: A symmetric curve with respect to $H = 0$, whereby the magnetic moments switch at the coercive field $\pm H_c$. If one adds a unidirectional anisotropy this curve is shifted by a field, called the exchange bias field H_{eb} .

The reason for this phenomenon is shown in Fig. 2.10b. The interface spins of the ferromagnetic (FM) and the antiferromagnetic (AFM) layer are parallel due to exchange coupling between these spins. If one now applies a negative field antiparallel to these spins the FM will reverse at a higher field as compared to a single FM layer. The AFM exerts an additional torque on the FM spins hindering the reversal for $|H| < |H_{eb} + H_c|$. Analogously the additional torque reverses the FM earlier as soon as $|H| < |H_{eb} - H_c|$.

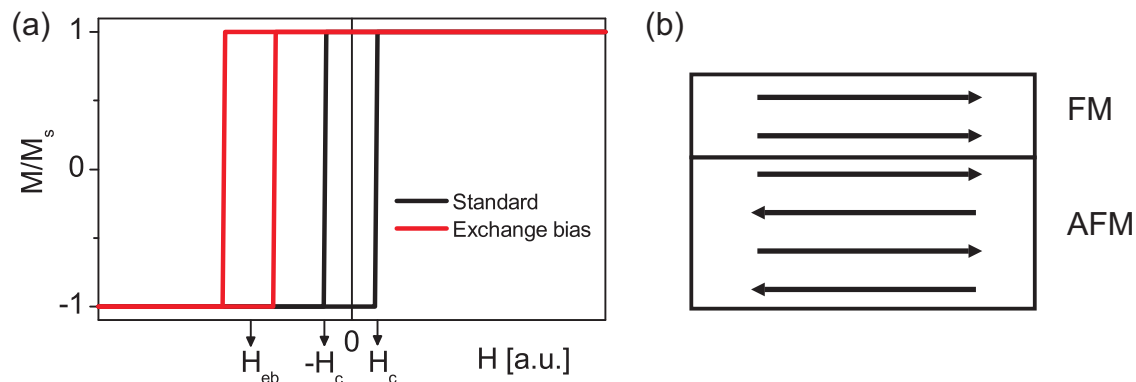


Figure 2.10: (a) Schematic representation of the hysteresis loops of a standard ferromagnetic material (black) and a ferromagnet with an unidirectional anisotropy (red), e.g. due to direct exchange coupling by a antiferromagnet. (b) Schematic of the coupling between a ferromagnetic (FM) layer and an antiferromagnetic (AFM) layer. The interface spins of both layers are parallel due to exchange coupling.

To generate such a situation one first heats a FM/AFM stack to a temperature between the Néel temperature (T_N - temperature above which an AFM becomes param-

agnetic) of the AFM and the Curie temperature (T_C - temperature above which a FM becomes paramagnetic) of the FM $T_N < T < T_C$. If this system is cooled down in a magnetic field, setting the direction of the FM, the interfacial spins of the AFM will couple to the FM spins. After this procedure a unidirectional anisotropy is frozen into this bilayer.

For polycrystalline films the interfacial spins of the AFM are nearly completely compensated leading to a strong reduction of the unidirectional anisotropy compared to the ideal case depicted in Fig. 2.10b. A detailed theoretical treatment of exchange bias and the accompanying effects can be found in [82–87].

2.2.4 Oscillatory exchange coupling

Parkin et al. [88] discovered in 1990 another coupling effect, the oscillatory exchange coupling. They showed that the saturation field as well as the saturation magnetoresistance of Co/Cr and Co/Ru multilayer oscillates with the thickness of the Cr and Ru spacer layer, respectively. They explained this behavior by an oscillatory change of the interlayer antiferromagnetic coupling strength J_1 .

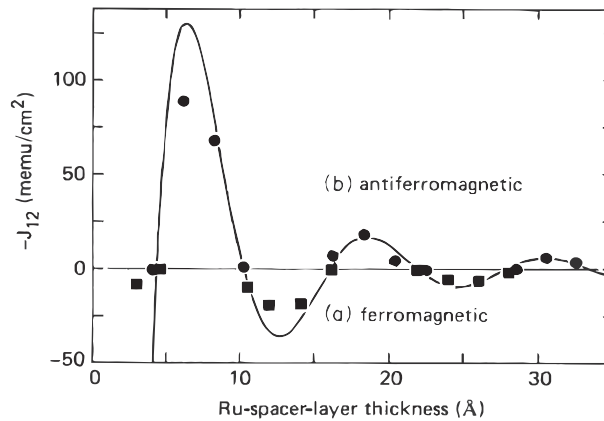


Figure 2.11: Interlayer exchange coupling strength J_{12} (notation of Parkin et al. [89]) as a function of the Ru-spacer-layer thickness in a $\text{Ni}_{80}\text{Co}_{20}/\text{Ru}/\text{Ni}_{80}\text{Co}_{20}$ sandwich. Source: [89] ($1 \text{ \AA} = 10^{-10} \text{ m}$, $1 \frac{\text{emu}}{\text{cm}^2} = 10^{-6} \frac{\text{J}}{\text{m}^2}$)

Interlayer coupling can be phenomenological described by the two coupling parameters J_1 and J_2 , whereas a positive and negative J_1 gives rise to a ferromagnetic and antiferromagnetic coupling, respectively. The second parameter J_2 describes a perpendicular coupling of the adjacent FM layers. The total energy density of the interlayer

coupling of a FM1/NM/FM2 sandwich can be expressed as [90]:

$$e_i = -J_1 \cos \angle(\vec{m}_{FM1}, \vec{m}_{FM2}) - J_2 [\cos \angle(\vec{m}_{FM1}, \vec{m}_{FM2})]^2. \quad (2.27)$$

Fig. 2.11 shows the oscillatory dependence of J_1/A (denoted as J_{12} in Fig. 2.11) on the interlayer thickness in a $\text{Ni}_{80}\text{Co}_{20}/\text{Ru}/\text{Ni}_{80}\text{Co}_{20}$ sandwich, including an oscillatory change in the sign of J_1 . Thus, the interlayer coupling changes between parallel and antiparallel alignment of the FM layers [89].

There have been several attempts to describe this phenomenon theoretically. A comparative review is given by Jones [91]. Today, the accepted theory is based on spin-dependent confinement of electron waves in the NM spacer layer and was given by Bruno et al. [92].

3 GMR samples

In the following section the samples, used in this thesis, are introduced. In the first part of this chapter different possibilities of creating a GMR device are treated. Two kinds of GMR stack compositions are used for the experiments and introduced in the next part. These are characterized by magneto-resistive measurements at the end of this section.

3.1 Composition of the GMR stack

To make use of the GMR effect it is essential to control the magnetization of the two FM layers separately. There are different ways to build such a device which is generally called spin-valve.

The simplest possibility is to use two ferromagnetic layers (separated by a NM layer) with different coercive fields (switching field of the FM layer), e.g. by FM layers of different thicknesses. This was first proposed by Shinjo et al. [93]. One obtains a hysteresis loop and a MR signal, which is schematically shown in Fig. 3.1a and b, respectively. Starting with a negative field and both layers magnetized parallel, and thus a low resistance, the FM layer with the lower coercivity switches its magnetic moment first as the magnetic field is increased above H_{c1} . The FM layers are antiparallel aligned and the resistance is highest. Increasing the field above the coercive field of the second layer H_{c2} , both layers are parallel magnetized and thus in the low resistance state.

As the working range of this spin valve is limited by the coercive field of the magnetically harder layer H_{c2} , one had to find possibilities to increase this field. One way was the use of the exchange bias effect by means of direct exchange coupling, which was first proposed by Dieny et al. [94]. Here, the magnetization of one FM layers was pinned by the exchange coupling to an antiferromagnetic layer as it was described in section 2.2.3. The second layer is the free layer and can be switched by the external field. With this GMR stack (free layer / NM layer / pinned layer) it is possible

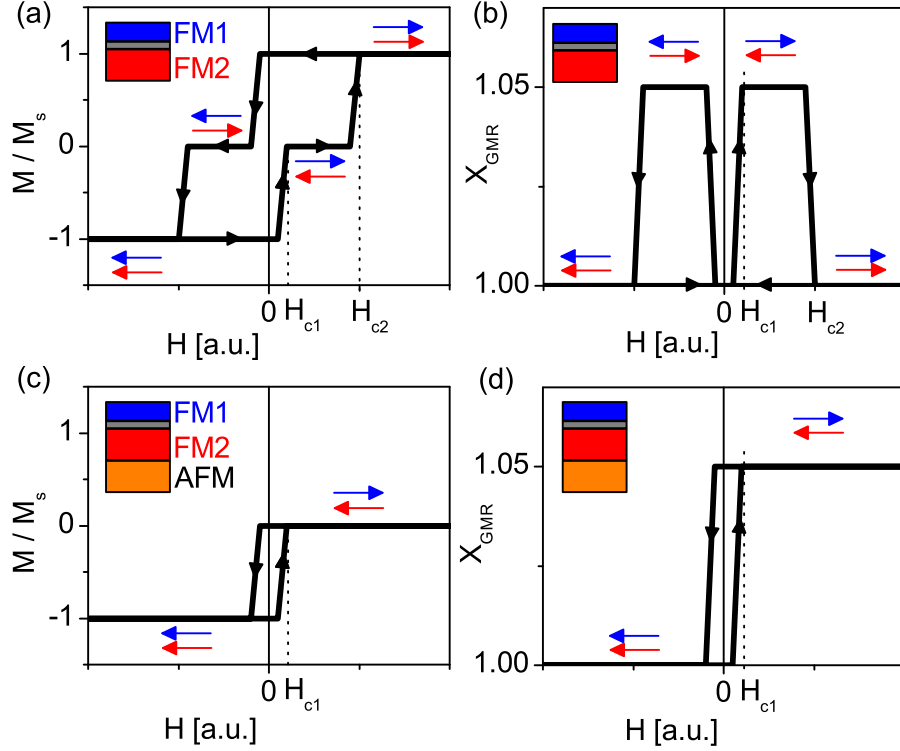


Figure 3.1: Magnetization (a) and X_{GMR} (b) in dependence on the applied field for a FM1/NM/FM2 sandwich with different coercivities of both FM layers. And magnetization (c) and X_{GMR} (d) in dependence on the applied field for a FM1/NM/FM2/AFM exchanged biased GMR stack for $H < H_{eb}$.

to apply external fields as high as the exchange bias field H_{eb} without reversing the magnetization direction of the pinned layer. Thus, the hysteresis and MR loops only show the switching of one FM layer for $H < H_{eb}$, as it is shown in Fig. 3.1c,d. The working window of such a stack is determined by H_{eb} which is typically in the range of 30 – 40 kA/m [74]. Increasing H_{eb} is hampered by the fact already discussed in section 2.2.3. The unidirectional anisotropy (which determines H_{eb}) is reduced due to a remarkable compensation of the interfacial spins of the antiferromagnet.

Another disadvantage of this technique of generating a pinned layer is the magneto static coupling of the pinned and the free layer in patterned GMR structures. To avoid this coupling and to increase the magnetic field range, one makes use of the oscillatory exchange coupling. Two FM layers and a NM interlayer are designed in a way, that the FM layers couple antiferromagnetically due to oscillatory exchange coupling. Moreover, the FM layers are chosen with the same thickness, so that the magnetic flux

of both layers is compensated. This three layer stack is called an artificial antiferromagnet (AAF) and was first proposed by van den Berg et al. [95]. Magnetic fields as high as 300 kA/m [96] are required to saturate such a AAF, i.e. to force the FM layers to be parallel to each other. Using the comparable weak direct exchange coupling to a natural AFM one can set the direction of the AAF and thus a reference direction.

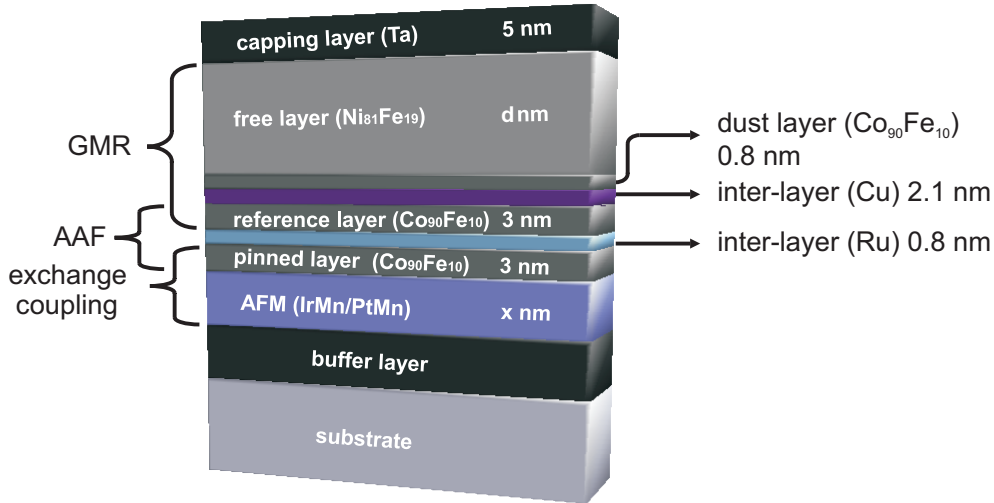


Figure 3.2: Schematic picture of the GMR stack, composed of the GMR unit, an artificial antiferromagnet (AAF) and a natural antiferromagnet responsible for the determination of the pinned layer reference direction. Two sets of samples were fabricated. One stack has a $x = 15$ nm PtMn AFM and $d = 20$ nm thick Py layer. The Py layer thickness of the other stack was $d = 10$ nm and the IrMn AFM was $x = 7$ nm.

Fig. 3.2 shows a schematic of the GMR stack used in this study. The composition was adapted from the spin valve proposed by Leal et al. [96]. The 5 nm Ta buffer layer on the substrate is the seed for the GMR stack. The first functional layer from bottom to top is the natural antiferromagnet which was either PtMn or IrMn with the thickness 15 nm and 7 nm, respectively. This layer pins the lower FM layer of a AAF which is composed of $\text{Co}_{90}\text{Fe}_{10}(3)/\text{Ru}(0.8)/\text{Co}_{90}\text{Fe}_{10}(3)$ (numbers in brackets denote the layer thickness in nm). The Ru thickness is chosen to be in the first maximum for antiferromagnetic coupling due to oscillatory exchange coupling (see Fig. 2.11) for a Ru inter-layer [89]. Because of the same thicknesses of both FM layers the magneto-static stray field is reduced to a minimum and is located in the space between both FM layers of the AAF. The upper FM layer of the AAF acts as the reference layer for the GMR

part of the spin valve $\text{Co}_{90}\text{Fe}_{10}(3)/\text{Cu}(2.1)/\text{Co}_{90}\text{Fe}_{10}(0.8)/\text{Ni}_{81}\text{Fe}_{19}(d)$. The thickness d of the Py ($\text{Ni}_{81}\text{Fe}_{19}$) layer determines, naturally, the thickness of the nanostripe where the DWs are propagating. The thickness of the Cu layer corresponds to zero coupling between the Py and the $\text{Co}_{90}\text{Fe}_{10}$ layer for a Cu inter-layer [97]. Additionally a 0.8 nm thick $\text{Co}_{90}\text{Fe}_{10}$ dust layer was added to the free layer in order to enhance the interfacial spin-dependent scattering and thus the GMR ratio [98].

3.2 Fabrication of the GMR nanostripes

There were two different sets of samples: First, samples having a 4" sapphire wafer and IrMn (7 nm) as substrate and natural antiferromagnet in the stack, respectively. These samples were fabricated at the Institute of Photonic Technology Jena e.V. [99]. The second set of samples were deposited on a 5" oxidized Si wafer with a 15 nm thick PtMn antiferromagnet in the stack. The fabrication of this set was performed by Sensitec [100].

The GMR stacks, produced at the IPHT, were deposited using dc sputter deposition in a ten target sputter machine with a base pressure of $< 2 \times 10^{-6}$ Pa. The accuracy of the layer thicknesses was better than $\pm 1\%$. The patterning of the films was conducted by electron beam lithography (resist ZEP520, base dose $100 \mu\text{C}/\text{cm}^2$ with a proximity correction) and Ar ion etching (Ar pressure 3.7×10^{-2} Pa, acceleration voltage 400 V, power 75 W).

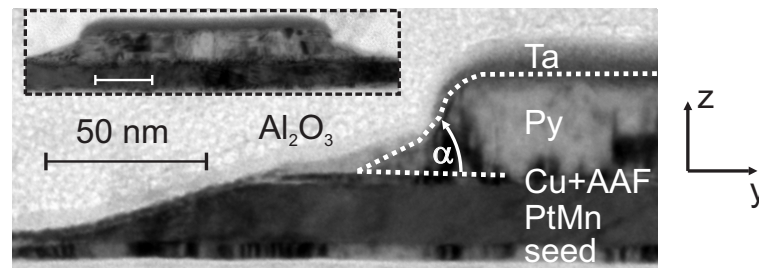


Figure 3.3: TEM image of the cross section of a nominal 250 nm wide GMR stack which was etched with Ar ions under tilt. The different layers composing the GMR stack are labeled. The dotted line is a guide to the eye, showing the profile of the Py layer. α denotes the angle of the slanted edge with respect to the substrate surface. Inset: overview of the cross section.

The second set of samples were in principle fabricated in the same way, however,

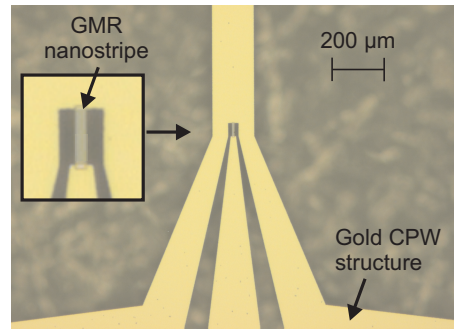


Figure 3.4: Optical micrograph of a chip. The electrical contact is provided by a coplanar waveguide made of Au. The inset shows a magnification of the nanostripe.

details are beyond the author's knowledge. Though the edge process was performed in a two step process under an angle of $\neq 90^\circ$ with a rotating substrate. This procedure was found to be favorable for the fabrication of the multiturn counter in terms of a reduced edge roughness. The cross section of such a nanostripe was imaged using a transmission electron microscope (TEM) and is shown in Fig. 3.3. The imaging and the preparation of the TEM lamella of the nanostripe by focused ion beam (FIB) was performed at the Max Planck Institute for Microstructure Physics (Halle) [101].

Due to the etching under tilt the free Py layer has a complex cross section with a trapezoidal form. The base angle α , which determines the edge steepness of the trapezoid, varies with the z-coordinate between 30° and 80° . Beside the Py layer the reference layer, composed of the AAF and the natural AFM, has a trapezoidal cross section, too. Here the base angle is constant and accounts for $\approx 18^\circ$.

For some samples the nanostripe had a so-called DW generator (DWG) at one end, which is an area of strongly increased width ($w_{DWG} = 10 \mu\text{m}$). Due to the much lower shape anisotropy in this area, the nucleation field is significantly reduced and thus the position of the DW nucleation is well defined. If no DWG is added to the nanostripe, both ends of the nanostripe have comparable nucleation fields and therefore the DW can be nucleated at either end.

After the patterning of the nanostripes, they were capped by a Al_2O_3 layer and electrically contacted by means of Au contact pads. The pads were designed in a coplanar waveguide (CPW) geometry [102] using the formulas provided in [103]. The CPW geometry ensures a low loss signal transmission of RF signals. An optical microscope

image of a chip is shown in Fig. 3.4.

For convenience the two sets of samples will be named according to the used natural AFM in the stack: PtMn- and IrMn-GMR stacks, respectively.

3.3 Magneto-resistive characterization of the GMR stack

The PtMn-GMR stack was characterized by means of magneto-resistive measurements using magnetic fields up to $H = 10^3$ kA/m. Fig. 3.5 shows the dependence of the resistance, normalized to the zero field resistance, as a function of the applied field. The nanostripe dimensions were $d \times w \times l = 20 \times 160 \times 45000$ nm³. Two measurements were conducted, a easy (EA) and a hard axis (HA) loop, where the applied field is parallel to the x - and y -axis, respectively (see Fig. 2.2 for definition of the orientations). For the HA loop two starting configuration were used: the parallel (low R) and antiparallel (high R) alignment of free and reference magnetization direction.

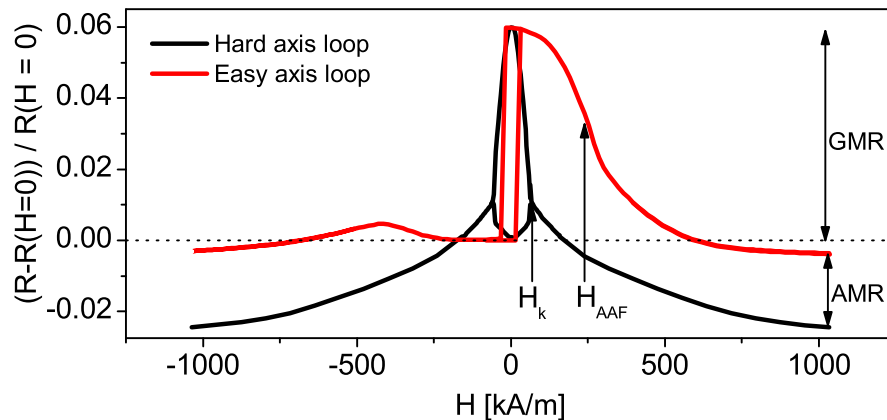


Figure 3.5: Magnetoresistance as a function of the applied field for a $45000 \times 160 \times 20$ nm³ nanostripe. The easy axis loop was measured for a field parallel to the x -axis (parallel to the long axis of the nanostripe, see Fig. 2.2) and the hard axis loop for a field in the y -direction (in-plane perpendicular to the nanostripe long axis).

From these measurements one can extract several quantities characterizing the GMR stack. First, the difference in the resistance for zero applied field gives the GMR ratio

of the stack, which accounts for 5.6%. The AMR can be extracted from a comparison of both measurements at high fields. The magnetization of the whole stack is parallel to the x -axis (y -axis) for the highest applied fields in the EA (HA) loop. The current flows in the x -direction and thus the resistance is lower for the hard axis loop, where magnetization and current are perpendicular to each other (see section 2.2.2). The AMR effect accounts for $X_{AMR} \approx 2\%$.

Fig. 3.6 shows the current distribution in the GMR stack if one considers ideal reflective interfaces between the single layers. This is of course only a rough estimation, however, the principle trend will be the same for a more realistic model. The resistivity of the different layers were determined by 4 point measurements of thicker single thin films. According to Fig. 3.6b the Py layer is the ferromagnetic layer, where most of the electric current is flowing. Therefore, the main contribution to the AMR stems from the Py layer.

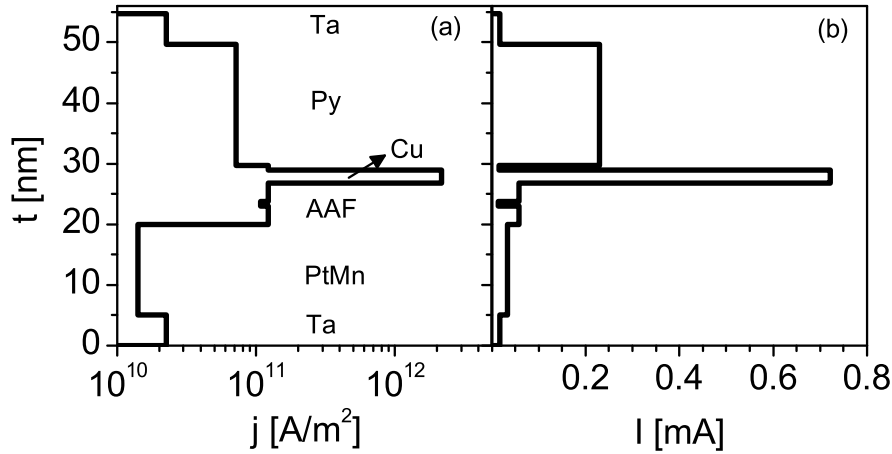


Figure 3.6: Current distribution in the GMR stack for the simple model of ideal reflective interfaces between the single layers. (a) and (b) shows the current density and the current in the layers for $I = 1.2$ mA which was used in the experiments (see section 4.1.1).

Beside this magneto-resistive quantities, one can extract magnetic properties of the stack, too. The transverse anisotropy field H_k^y (the transverse field H_{tr} , where the free layer Py magnetization is completely tilted in the y -direction) can be determined by the HA loop. Given a small deviation of the magnetization inside the AAF and the natural antiferromagnet the resistance of the stack should be $\frac{X_{GMR}}{2} - X_{AMR}$ if the Py magnetization is completely rotated in the y -direction at $H = H_k^y$. With a adequate

Table 3.1: Magneto-resistive and magnetic properties of the used GMR stacks for a different nanostripe cross sections.

Natural AFM	PtMn	PtMn	PtMn	PtMn
nominal cross section [nm ²]	20 × 160	20 × 250	20 × 500	20 × 1000
X_{GMR} [%]	5.6	5.5	5.3	5.1
X_{AMR} [%]	2.0	2.4	2.4	2.4
H_k^y [kA/m]	53	43	29	17
H_{AAF} [kA/m]	250	236	233	224

fit of the high resistance HA loop the transverse anisotropy field can be estimated by $H_k^y = 53$ kA/m.

The last quantity is the field which is necessary to overcome the AFM exchange coupling of the AAF H_{AAF} . It is determined by the inflection point at the EA loop for a positive field [74] and amounts to $H_{AAF} = 250$ kA/m.

This characterization was performed for all PtMn GMR stacks used in the experiments. Table 3.1 summarizes the extracted quantities for four PtMn-stacks of different nanostripe width. Note that the denoted widths are nominal widths only. A determination of the exact width was difficult for two reasons: first the 500 nm thick Al₂O₃ capping layer hinders a determination of the nanostripe width by scanning electron microscopy or atomic force microscopy. And second the complex cross section shown in Fig. 3.3 do not allow for an identification of an absolute DW width. From the TEM image of the nominal 250 nm wide nanostripe one can deduce a width being between $w = 200 - 275$ nm, whereby the actual width depends on the z -position. The same arguments hold for the 3 other PtMn nanostripes.

Both fields H_k^y and H_{AAF} decreases with the nanostripe width. This is in line with the theory. A quantitative comparison to theoretical values, obtained by the demagnetizing factors (see eqs. (2.14) and (2.15)) is difficult, because of the complex cross section shown in Fig. 3.3. The variation of the MR ratios could not be understood from the theoretical point of view. Perhaps the differences stem from statistical distribution of the MR ratios over the samples.

4 Results

In this chapter the results of the measurements, accompanying micromagnetic simulations and their interpretation are presented. As stated in the introduction the focus will be on the influence of a transverse field on the behavior of DWs in nanostripes. In the first part the dynamics of a DW, driven by a magnetic field, is treated and the second section covers the influence of a transverse field on DW pinning.

4.1 Domain wall dynamics

Since the beginning of the experimental verification of magnetization reversal in magnetic nanostripes by means of DW nucleation and propagation via the GMR technique [5, 6] in the late 1990s there have been numerous papers on field driven DW dynamics [22–35]. Most of these papers use the AMR and magneto-optical Kerr effect (MOKE) [104] in the following manner. The AMR is to detect the presence of a DW in the nanostripe. With the time period, the DW is in the nanostripe, and the length of the nanostripe one can calculate a mean velocity of the DW. The MOKE technique, which is sensitive to the magnetization direction in a magnetic material illuminated by a laser spot, is mostly used in a time of flight experiment. Here two laser spots with a defined distance are used to detect the time that is needed by the DW to travel the distance between the spots. Both measurement techniques have the poor signal to noise ratio in common:

- For the MOKE technique a laser spot with a diameter of typically several μm is used. The nanostripes, on the other hand, have a width below $1 \mu\text{m}$. The contrast only arises from magnetic changes in the nanostripe and as most of the laser spot illuminates nonmagnetic surrounding material the signal to noise ratio is bad.
- The AMR technique is sensitive to magnetic moments being parallel or perpendicular to the measurement current. Mostly the current flows parallel to the long

axis of a nanostripe which is the easy magnetization axis, too. Hence, the magnetization is in absence of a DW parallel to the current. Only in presence of a DW a perpendicular component of the magnetization exists. However, the width of the DW is much smaller as compared to the length of the nanostripe, giving rise to a tiny change in resistance if a DW is present.

In order to get a significant signal to noise ratio one has to average over many thousands of experiments. These experiments, therefore, had to be highly periodic, which is only partly true for field driven DW dynamics.

The theory of field driven DW dynamics predicts three modes of TDW movement for $H < H_w$, $H > H_w$ and $H \gg H_w$ (section 2.1.4). For $H < H_w$ the DW moves in a steady state mode, whereby this regime is characterized by a constant mobility $\mu = dv/dH$. In theory this motion type should be reproducible and thus accessible by measurement techniques that require averaging over many thousands of experiments. For $H > H_w$ the DW starts to precess, which in theory is periodic. However, it has been shown that an edge roughness of the nanostripe significantly influences the Walker process. Thiaville et al. reported a suppression of the Walker field H_w due to a roughness of the nanostripe edges [105]. It will be shown that the Walker field is increased by means of an edge roughness. Given a distribution of the edge roughness along the nanostripe, one can assume a dependence of the Walker field on the position of the DW in the nanostripe. Whether a vortex or antivortex is nucleated at a certain position depends on the Walker field at this position. Thus, in real nanostripes the Walker process must not necessarily be periodic. For $H \gg H_w$ the DW dynamics became very complex as shown by Lee et al. [106], which again gives rise to a stochastic process in real nanostripes.

In order to examine stochastic processes, e.g. the WBD in rough nanostripes, it is essential to perform single shot experiments. The good signal to noise ratio of the GMR technique enables us to examine these processes in detail. The following sections treat selected topics of field driven DW dynamics. It is organized as follows: At the beginning the experimental instrumentation used for the characterization of the DW movement in a single shot mode is introduced. The second part deals with the nucleation of DWs in nanostripes under the special condition of an in-plane transverse field. Next the Walker process is examined in detail. I will show, that this process is not periodic in GMR nanostripes [107], contrary to the theory for perfect nanostripes [105]. The second part will explain the influence of a transverse field on the Walker

process.

The next part introduces a new kind of DW motion below the Walker field: a split transverse DW that is only dynamically stable. This DW propagation mode was discovered by single shot experiments and will be explained by micromagnetic simulations [108]. The influence of a transverse field on the DW dynamics will be treated in the following part [109]. Thereby the impact on the dynamics in the three regimes of DW movement are discussed in detail. After treating the influence of the edge roughness and a transverse field on the DW behavior in the first parts, the last part will deal with the impact of the cross section shape on DW movement [110]. At the end I will give a conclusion.

4.1.1 Experimental instrumentation

For the characterization of the DW dynamics in this thesis I used a magnetic field composed of two perpendicular components: the longitudinal field H_{long} and the transverse field H_{tr} . As is shown in Fig. 4.1a both fields and the nanostripe are in the $x - y$ plane. A system with two coils arranged perpendicular to each other were used to generate the magnetic field of arbitrary in-plane angle.

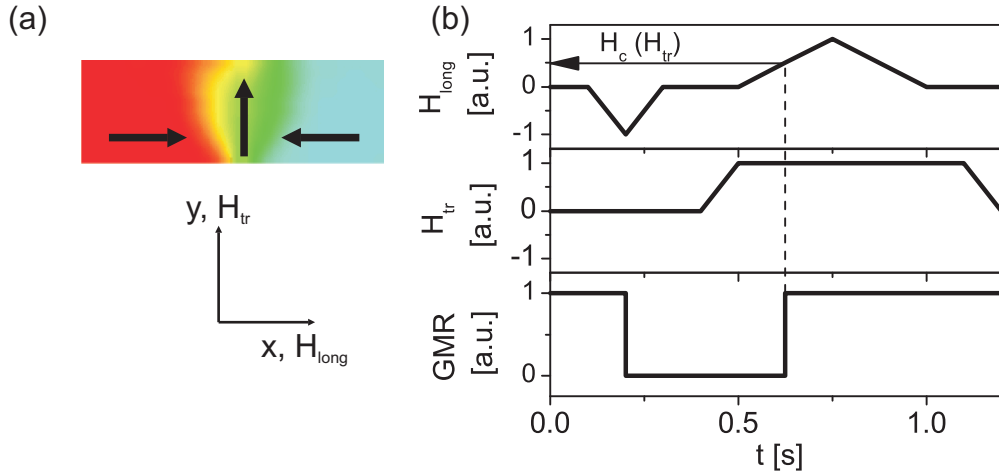


Figure 4.1: (a) Definition of the two field components H_{tr} and H_{long} with respect to the orientation of the nanostripe. Both fields are generated by two coil systems arranged perpendicular to each other. (b) Schematic of the measurement cycle.

The measurement cycle is shown schematically in Fig. 4.1b. First a field pulse of the amplitude $|H_{pulse}| > H_c$ saturates the nanostripe in $\pm x$ -direction (Fig. 4.1b shows the case for a negative direction). Eventually a constant transverse field of arbitrary amplitude is applied during the forthcoming measurement. To nucleate and propagate a DW in the nanostripe a longitudinal field opposite to the field pulse is increased linearly with a slew rate of $\frac{\Delta H_{long}}{\Delta t} = 160 \frac{kA/m}{s} = 0.16 \frac{A/m}{\mu s}$. If the coercive field H_c of the free Py layer is reached a DW is nucleated and propagates through the nanostripe. The resistance of the GMR stack will change. As the velocity of a DW is in the order of 100 m/s [23], the DW travels $0.5 \mu s$ for a $50 \mu m$ long nanostripe. In this time period the longitudinal field is practically constant compared to the applied field in the range of $H_{long} = 0.5 - 20$ kA/m.

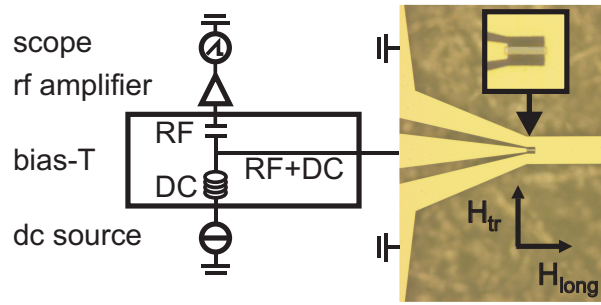


Figure 4.2: Measurement setup used for the characterization of the DW dynamics with quasi static fields.

In order to measure the change in the nanostripe resistance time dependently, I used the measurement setup shown schematically in Fig. 4.2. To obtain a better signal to noise ratio the RF part of the signal is separated from the DC part by means of a bias-T: a three terminal device with a DC path, RF path and a mixed path. This device is normally used to add a DC power to a RF signal. In this study the bias-T 5575A of the company Picosecond Pulse Labs was used in the following manner. The CPW structure of the GMR chip is connected to this mixed connector. The DC path was used to supply the system with a continuous current which is generated by a DC source build with a voltage reference IC (see manual page 20 [111]). The current source is fed by a battery in order to reduce noise. The current generates a voltage drop over the GMR nanostripe. If the magnetization state of the GMR stack changes, its resistance will alter due to the GMR effect. The corresponding change in the voltage will be conducted through the RF path of the bias-T, whereby the DC part is filtered by the capacitance of this path. The signal is amplified by a RF amplifier (HSA-X-1-40 High-Speed-Amplifier, Femto) and detected by means of an oscilloscope.

The current, which was used to fed the system, corresponds to a current density of $j = 1.3 \times 10^{11}$ A/m² for a uniform current distribution in the stack. Considering the different conductivities of the layers a current density of $j \approx 7 \times 10^{10}$ A/m² in the Py layer is obtained (Fig. 3.6a). The critical current for current induced DW motion in a 20×200 nm² Py nanostripe was determined by Heyne et al. to be $j \approx 3 \times 10^{12}$ A/m² [112]. Assuming the more realistic nonuniform current distribution, the current is about two orders of magnitude below the critical current.

Another impact of the current on the DW dynamics could stem from the magnetic field produced by the nonhomogeneous current distribution. The higher current in the

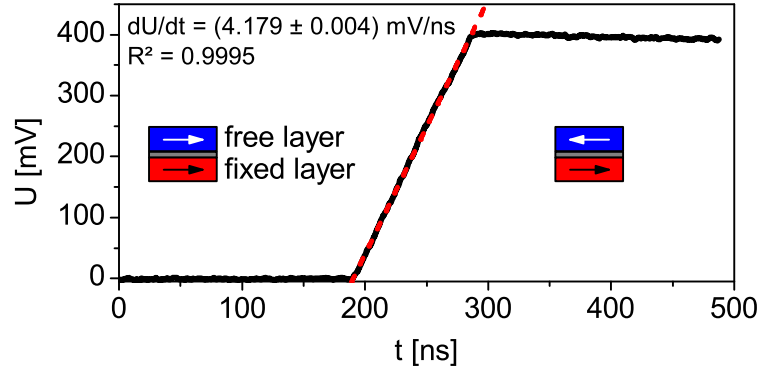


Figure 4.3: Sample measurement for a $20 \times 160 \text{ nm}^2$ nanostripe without a nucleation pad in a driving field of $H_{long} = 11.3 \text{ kA/m}$. The velocity is calculated from the slope and accounts for $v = (467 \pm 7) \text{ m/s}$.

Cu layer as compared to the Py layer gives rise to a transverse field acting on the Py layer. A control measurement with a positive and negative current of $I = \pm 1 \text{ mA}$ (not shown here) indicated no significant difference in the DW velocity. Thus, the current has no significant influence on our experimental results of field driven DW motion.

Fig. 4.3 shows a single shot sample measurement of the free layer switching for a $20 \times 160 \text{ nm}^2$ nanostripe in a driving field of $H_{long} = 11.3 \text{ kA/m}$. The velocity of a DW, which switches the magnetization by moving through the nanostripe, can be deduced from the slope of the $U(t)$ -curve. The example yields a velocity of $v = (467 \pm 7) \text{ m/s}$. The error is determined by using the specifications of the oscilloscope, namely the vertical and horizontal resolution. For the measurements two different oscilloscopes were used, whose parameters are given in table 4.1. For the results presented below the error of the v determination is with 1.5% below the resolution of the graphs and thus is omitted in the discussions. In the following sections the $U(t)$ data are used to calculate the temporal evolution of the DW position x under the assumption of a rigid DW, which is fulfilled in most cases.

Table 4.1: Specifications of the two oscilloscopes used in the experiments.

quantity	Tektronix DPO 4032	Agilent DSO
vertical resolution [bit]	8	8
bandwidth [GHz]	0.4	4
sampling rate [GSa/s]	2.5	40

4.1.2 Nucleation of a DW

For the study with quasi-static fields the nucleation field H_{nuc} of the DW, or more precisely the longitudinal component of the nucleation field H_{long}^{nuc} , represents the driving field of the DW. Therefore, the determination of this field it is essential. Using a 1Ω shunt resistance the current generating the longitudinal field was monitored with the oscilloscope and thus the nucleation field could be determined. Fig. 4.4 shows the nucleation field for 25 consecutive measurements, performed for $H_{tr} = 0$ and $H_{tr} = 30$ kA/m, respectively. The error of the H_{long}^{nuc} determination can again be estimated by specification of the used oscilloscope. It is below 1% and thus smaller than the symbol size. Fig. 4.4 indicates a significant influence by a transverse field on the longitudinal component of the nucleation field. First it is decreased to roughly one third and second the statistical variation is reduced. For $H_{tr} = 0$ ($H_{tr} = 30$ kA/m) one finds a nucleation field of $H_{long}^{nuc} = (11.25 \pm 0.13)$ kA/m ($H_{long}^{nuc} = (3.82 \pm 0.02)$ kA/m). These values are the arithmetic mean and the standard deviation of the 25 measurements.

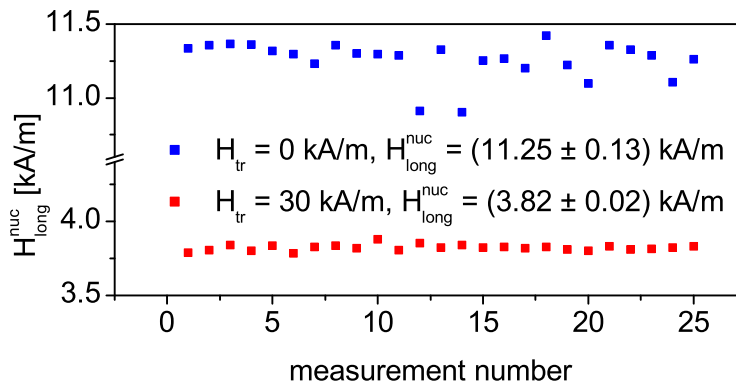


Figure 4.4: Longitudinal component of the nucleation field for 25 consecutive measurements for a 20×160 nm² nanostripe. H_{long}^{nuc} as well as its statistical variation is decreased due to an applied transverse field. The error of the H_{long}^{nuc} values is smaller than the symbol size.

The reason for the decrease of H_{long}^{nuc} can be understood intuitively. For $H_{tr} = 0$ the domain magnetization is antiparallel to the applied longitudinal field and according to the LLG equation (2.13) no torque is exerted on the magnetization. Deviations from this situation only arise from thermal fluctuation. For $H_{tr} = 30$ kA/m the magnetizations of the domain magnetization will be tilted in the direction of the transverse field

and a torque is exerted by H_{long} . The larger H_{tr} , the larger is the tilt of the magnetization and as a consequence the torque acting by H_{long} . The longitudinal component of the nucleation field will, therefore, decrease as H_{tr} increases.

In order to obtain a better understanding of the processes involved in DW nucleation, quasistatic micromagnetic simulations were performed. A $10 \times 160 \times 1800 \text{ nm}^3$ nanostripe was saturated with a negative longitudinal field and afterwards relaxed in zero field. Fig. 4.5a shows the relaxed magnetization state for the left 650 nm of the nanostripe. To reduce the stray field energy two closure domains are formed at the edge of the nanostripe, pointing in the positive and negative y -direction, respectively. In the simulation the nanostripe is perfect concerning its geometry and magnetic parameter distribution. Therefore, the closure domains are symmetric with respect to the middle position of the nanostripe. This configuration is stable for longitudinal fields smaller than $H_{long} < 17.5 \text{ kA/m}$ as it can be seen in Fig. 4.5b. For $H_{long} = 17.5 \text{ kA/m}$ only one closure domain is left, which already has the form of a half transverse wall (see Fig. 2.3b). Thus, a torque is exerted on the closure domain by the applied longitudinal field and the magnetization inside this domain is tilted in the field direction (see Fig. 4.5d, e). If the nucleation seed is large enough a DW is nucleated and reverses the magnetization of the nanostripe.

The simulations were carried out for $T = 0 \text{ K}$. In contrast the experiment was conducted at room temperature. Thus, the switching from two closure domains to only one closure domain will be for smaller fields in the experiment due to thermal activation. Moreover, the y -magnetization of the remained closure domain will change statistically for several experiments. Because of geometric imperfections of the nanostripe, the nucleation field of a DW can be different for both y -magnetizations of the closure domain, giving rise to a statistical variation of H_{long}^{nuc} .

For $H_{tr} \neq 0$ the situation changes. The transverse field breaks the symmetry of the two closure domains and the closure domain with a y -magnetization parallel to the applied field is stable. The statistical variation of H_{long}^{nuc} should be smaller, as it is observed in the experiment. Moreover the closure domain is larger because its magnetization is stabilized by the transverse field. The critical size of the nucleation seed will be achieved for smaller longitudinal fields and the H_{long}^{nuc} will be smaller accordingly. The micromagnetic simulations yield a nucleation field of $H_{long}^{nuc} = 16.7 \text{ kA/m}$ for $H_{tr} = 23.8 \text{ kA/m}$ which is roughly one half of H_{long}^{nuc} for $H_{tr} = 0$. Note that the

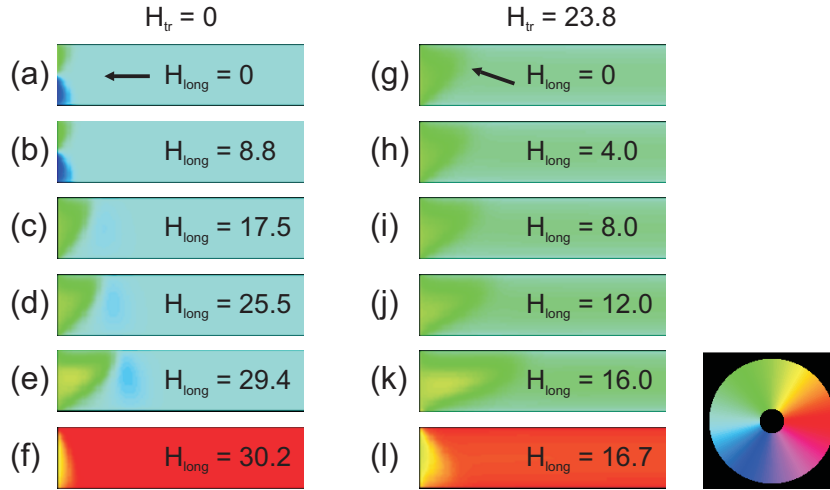


Figure 4.5: Micromagnetic simulation of the relaxed in-plane magnetization direction during the DW nucleation process in a $10 \times 160 \times 1800 \text{ nm}^3$ nanostripe for (a-f) $H_{tr} = 0$ and (g-l) $H_{tr} = 23.8 \text{ kA/m}$. Plotted is the 650 nm long left part of the nanostripes. The nucleation field of a DW is $H_{long}^{nuc} = 30.2 \text{ kA/m}$ for $H_{tr} = 0$ and $H_{long}^{nuc} = 16.7 \text{ kA/m}$ for $H_{tr} = 23.8 \text{ kA/m}$. The magnetic fields are given in kA/m and the black arrows in the first row indicate the magnetization direction of the domain.

transverse field prefers a nucleation of a DW with a core magnetization parallel to the H_{tr} direction.

In conclusion the transverse field is a tool to manipulate the nucleation conditions of a DW. This is necessary because of the dependence of the quasi-static experiments on the longitudinal component of the nucleation field H_{long}^{nuc} which is concurrently the driving field of the DW. Note that although the simulations were carried out for time-saving reason with 10 nm nanostripes, the same arguments also hold for the 20 nm thick nanostripes.

4.1.3 Visualization of the Walker breakdown process

Introduction After the prediction of the Walker breakdown process by Walker et al. in the 1970s [65] a deeper understanding of this phenomenon has been gained by micromagnetic simulations during the past years [48, 66, 67, 105, 113–117].

Several attempts have been conducted to verify the WBD experimentally. Beach et al. [23] showed for the first time the typical velocity field dependence, predicted by the 1-d model by Walker (see Fig. 2.7). The significant drop of the mean velocity above the critical Walker field indicated the occurrence of the WBD. These measurements were carried out using the magneto-optical Kerr effect (MOKE) [104] in a time of flight (TOF) experiment. They used two MOKE laser spots separated by a defined distance and measured the time which the DW needs to travel the distance between both laser spots. By analyzing the transition time, the DW needs to travel through *one* laser spot, they found an increased time above the Walker field [29]. This transient broadening was attributed to the oscillatory movement of the DW above H_w . The group of Parkin et al. used the AMR effect to investigate the DW dynamics. Due to the sensitivity of the AMR on the transverse magnetization, they found oscillations of the resistance in Py nanostripes [24, 25].

Both groups used single Py nanostripes patterned with the focused ion beam technique. The edges of these Py stripe will be contaminated with Ga ions, which reduces the saturation magnetization of the Py in this region [118]. Therefore, the influence of the nanostripe edges on the DW dynamics will be reduced. The group of Parkin reported a highly periodic WBD in their nanostripes [24]. Only this periodicity enabled both groups to investigate the WBD. As explained in section 3.1 our Py nanostripe is part of a complex magnetic multilayer fabricated by e-beam lithography and Ar ion etching. This technique produces a larger edge roughness compared to the focused ion beam technique.

Beside the edge roughness nanostripes show a surface and interfacial roughness, respectively. If the magnetic layers are not perfectly plane the magnetizations of adjacent layers will interact with each other via the stray field energy. This effect is called orange peel coupling [45], e.g. between the Py layer and the magnetic layer beneath. Mascaro et al. reported an interaction between a 360° DW in the reference layer and a 180° DW in the Py layer in a GMR stack [119]. It is not due that a 360° DW will be situated in the AAF. However, it is most likely that perturbations in the reference layer alignment along the long axis will have an influence of the DW dynamics in the

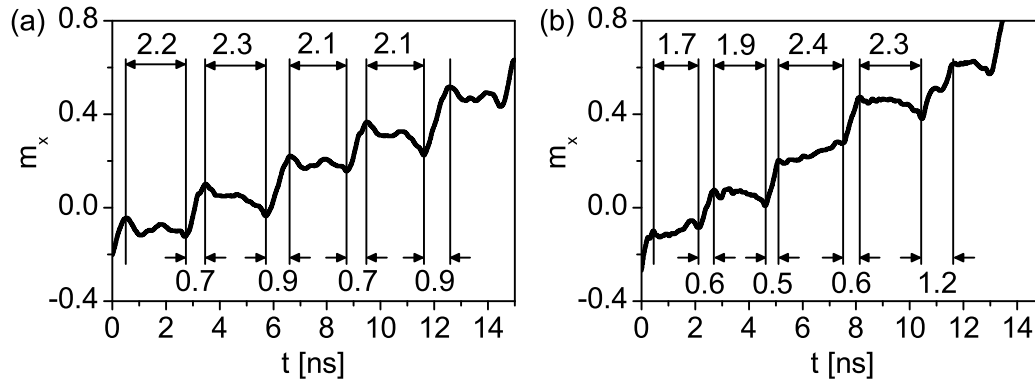


Figure 4.6: Micromagnetic simulation of the DW dynamics in a $10 \times 200 \times 2000 \text{ nm}^3$ nanostripe with (a) perfect borders ($H_{long} = 4 \text{ kA/m}$) and (b) disturbed borders ($H_{long} = 6.3 \text{ kA/m}$). For the 20 nm wide disturbed edge area a Gaussian distributed roughness with a correlation length of 20 nm was introduced. The times of DW forward propagation are given at the bottom. The periods, where an antivortex crosses the nanostripe are plotted at the top of the graph. All times are denoted in ns. Source: [107]

Py layer by means of the produced stray field.

These considerations suggest a stochastic distributed frequency of the WBD. This is investigated by both, micromagnetic simulations and by single shot measurements. After the characterization of this process in GMR nanostripes the influence of H_{tr} on the WBD will be explained. Therefore, the measurements for nanostripes with different dimensions will be presented.

Characterization of the WBD In order to characterize the influence of an edge roughness on the Walker process micromagnetic simulations were carried out for a $10 \times 200 \times 2000 \text{ nm}^3$ nanostripe ($M_s = 800 \text{ kA/m}$, $A = 1.3 \times 10^{-13} \text{ J/m}$, $\alpha = 0.01$) [107]. Two separate simulations were performed: one nanostripe with perfect borders and another one with a stochastic edge roughness. The edge roughness was introduced to a 20 nm wide area at the edge. This area was disturbed by a Gaussian distribution with a correlation length of 20 nm , which is comparable to the grain size of the Py layer [107].

Fig. 4.6 shows the temporal evolution of the x -component of the magnetization for perfect (a) and disturbed (b) borders. Both graphs indicate the typical behavior of a DW during the WBD: a periodic change between forward and backward movement.

Note that the driving field is higher in the case with an edge roughness. Thiaville et al. [105] reported a suppression of the WBD in a rough nanostripe. This is, however, only partially true. In fact the Walker field is increased and one has to apply a higher field in order to get a comparable behavior, i.e. a WBD frequency in the same range. During the forward movement the TDW moves with a high constant velocity after a short acceleration process. If an antivortex is nucleated at the edge of the nanostripe, it will cross the nanostripe, causing a back- and forward movement with a marginal net forward displacement (see Fig. 2.6). The time of TDW forward movement, as well as the time an antivortex crosses the nanostripe are depicted at the bottom and at the top of the graph. For the nanostripe with perfect edges the WBD is highly periodic showing small deviation of both times. One period of the WBD accounts for $T_{WBD} = 6$ ns (two stop-and-go periods) corresponding to a frequency of $f_{WBD} \approx 167$ MHz. The Walker field for this geometry can be approximated with the formula (4.1) found by Bryan et al. [117] by micromagnetic simulation and accounts for $H_w = 0.53$ kA/m. Within the framework of the 1-d model eq. (2.20) predicts a frequency for Py of 139 MHz (eq. (4.2)), which is in good agreement with the simulation. In contrast to this case, the nanostripe with disturbed borders shows stochastic DW dynamics. The backward motion during the crossing of the antivortex which is found for perfect borders is not observed for every WBD. The times of the two parts of the WBD show a larger variation. The mean WBD period accounts for $T_{WBD} = 5.6$ ns, which yields $f_{WBD} \approx 179$ MHz.

$$H_w(kA/m) = 3.66e^{-0.007w/nm-0.09t/nm} + 0.159 \quad (4.1)$$

$$f_{1d} = 35174.16 \frac{m}{As} \sqrt{H_{long}^2 - H_w^2} \quad (4.2)$$

It is obvious that, for nanostripes with a certain edge and interface roughness, the characterization of this process can only be done by single shot measurements. Fig. 4.7a shows a single shot measurement obtained with the 4 GS/s oscilloscope. The PtMn GMR stack (all measurements in this paragraph are done using this sample type) was 20×1000 nm² in cross section having a nucleation pad at one nanostripe end in order to reduce the nucleation and thus the driving field of the DW. The grey and the black curves represent the original and smoothed data, respectively. For the smoothing a Hamming filter with the normalized cut off frequency of $f_n/f_s = 0.2$ and a length

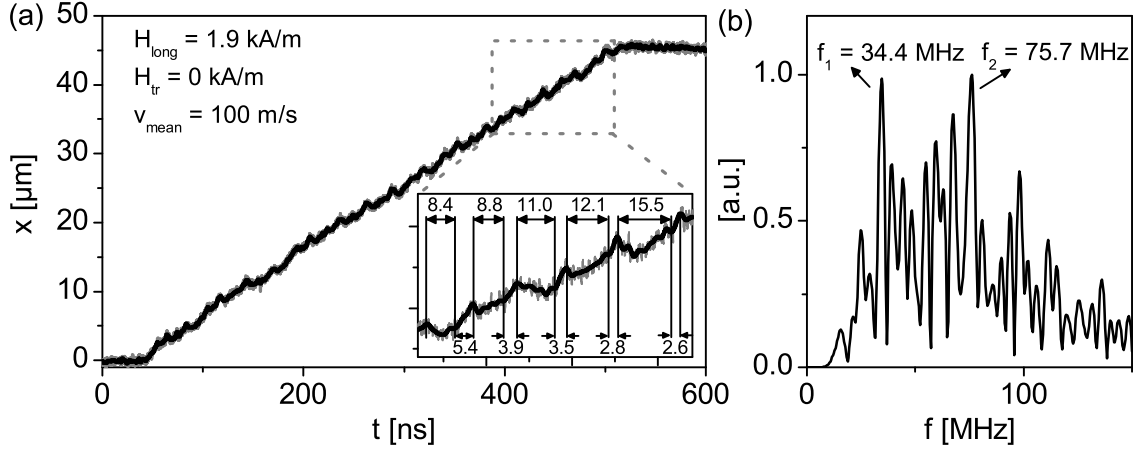


Figure 4.7: (a) DW movement in a $20 \times 1000 \text{ nm}^2$ nanostripe for $H_{long} = 1.9 \text{ kA/m}$ and $H_{tr} = 0$. The gray curve represents the original data and the black one is obtained using a Hamming filter with a normalized cut off frequency of $f_n/f_s = 0.2$ and a length $N = 400$. The sample frequency was $f_s = 40 \text{ GHz}$ (see table 4.1). Inset: Blow up, with the periods of motion and halt during the WBD. (b) shows the frequency spectrum of the WBD obtained by a FFT.

$N = 400$ was used [120].

The typical features of the WBD are clearly observed. The DW moves back- and forward periodically, however, the process shows a distinct stochasticity. The frequency of this process is plotted in Fig. 4.7b. The spectrum was obtained by an FFT of the $x(t)$ data during DW movement after subtraction of the mean slope $\langle \frac{dx}{dt} \rangle$. The bandwidth is $\Delta f \approx 80 \text{ MHz}$. This is roughly a factor of four larger as compared to the case of smooth nanostripes. Hayashi et al. [25] obtained a rather narrow frequency range $\Delta f \approx 20 \text{ MHz}$. The higher bandwidth in our samples reflects the stochasticity of the WBD in rough nanostripes.

The band is split into several peaks, whereby the two main peaks are located at $2f_{exp1} = 34.4 \text{ MHz}$ and $2f_{exp2} = 75.7 \text{ MHz}$. Note that the experimentally determined frequencies correspond to only half the Walker period as it is described by the 1-d model. Since one stop-and-go period during the measurement changes the TDW core magnetization only by 180° (see Fig. 2.6e and k), whereby the 1-d model calculates the precession frequency of the DW core magnetization and thus a change by 360° (see Fig. 2.6e and o). Therefore, the experimentally determined Walker frequencies

are between $f_{exp1} = 17.2$ MHz and $f_{exp2} = 37.9$ MHz.

The Walker field of this nanostripe can again be calculated using eq. (4.1) and accounts for $H_w = 0.16$ kA/m. For the driving field of $H_{long} = 1.9$ kA/m the WBD frequency accounts for $f_{1d} = 66.6$ MHz (eq. (4.2)), which overestimates the Walker frequency by roughly a factor of 2. This is, however, not surprising, as the Walker frequency strongly depends on the Walker field which in turn is changed due to an edge roughness like it was explained above. Eq. (4.1) was determined by simulations of the Walker field for perfect nanostripe edges. Moreover, the extrapolation to such large cross sections is at least doubtful, as the largest simulated cross section was 20×50 nm² [117]. A calculation of the Walker fields corresponding to the observed frequencies yields values between (1.57 – 1.84) kA/m. The 1-d model predicts a Walker field of $H_w^{1d} = 3.06$ kA/m which is even higher than the applied field $H_{long} = 1.9$ kA/m. Thus, the Walker field of the rough nanostripe lies in between the values determined by simulation and the 1-d model, as it was reported by Beach et al. [121]. The occurrence of different frequencies can be explained by a certain distribution of the edge roughness along the nanostripe and therefore of the Walker field, too. Table 4.2 collects the data for the calculated Walker fields and frequencies for the different models.

Table 4.2: Calculation of the Walker field and frequency with different models.

Method for calculation of H_w	H_w [kA/m]	f [MHz]
Calculated with f_{exp} and eq. (4.2)	1.84 – 1.57	17.2 – 37.9
Using eqs. (2.14),(2.15),(2.17) of the 1-d model	3.06	-
Using eq. (4.1) of Bryan et al. [117]	0.16	66.6

The inset of Fig. 4.7a shows a blow up of the DW movement. At the initiation of the WBD the DW first moves backwards and then forwards. This is a clear evidence for the appearance of a vortex during the WBD [67]. An antivortex would move vice versa: first a forward and than a backward movement. The occurrence of a vortex is in line with the simulations by Lee et al., who reported the appearance of a vortex for their largest simulated nanostripes with a cross section of 20×240 nm², whereby a antivortex is nucleated during WBD for smaller samples [67]. Thus, it is most likely that a vortex is nucleated in a 20×1000 nm² nanostripe, too.

Influence of a transverse field on the Walker process To investigate the WBD further, the DW dynamics in nanostripes of different width were characterized.

Moreover the influence of an in-plane transverse field on the WBD was studied for the different nanostripes. The impact of H_{tr} is twofold. First, as explained in section 4.1.2, the longitudinal component of the nucleation field is decreased with increasing transverse field, i.e. the driving field of the DW is decreased. Second the transverse field alters the Walker field, as described by Bryan and Wang [37, 39]. This give us a tool to investigate the WBD in narrow nanostripes, too, although the nucleation field for $H_{tr} = 0$ is much larger as compared to H_w . Fig. 4.8 shows the DW dynamics for a $20 \times 250 \text{ nm}^2$ nanostripe in dependence on different transverse fields. The left plots show the movement of the DW with a blow up as an inset and the frequency spectrum is plotted in the right graphs. The denoted peak positions f_{exp} are determined by a Gaussian fit.

In contradiction to the case for $H_{tr} = 0$ in Fig. 4.7 the WBD gets much more periodic by the application of H_{tr} . The frequency spectrum shows only one main peak. This can be understood by the increased width of the DW under the influence of H_{tr} , as it was derived by micromagnetic simulation by several groups [37, 38, 109]. Due to the larger DW width the local variations of the nanostripe geometry are smeared out, and the roughness has less influence on the dynamics.

The main effect of H_{tr} is, however, the suppression of the WBD with increasing transverse field. For $H_{tr} = 12 \text{ kA/m}$ (Fig. 4.8a,b) the main peak in the frequency spectrum accounts for $f_{exp} = 96.7 \text{ MHz}$. Increasing the transverse field to 16 and 18 kA/m the frequency decreases to 54.7 and 42.3 MHz, respectively. For a transverse field of $H_{tr} = 20 \text{ kA/m}$ the WBD is completely suppressed and the DW moves in a steady state regime with a constant velocity (see fig. 4.8g).

In order to compare these results with the 1-d theory, the frequency was calculated using Walker fields which were determined by a 1-d model developed by Lu et al. [39]. This model includes the influence of a transverse field in arbitrary direction on the DW dynamics. The demagnetizing factors were calculated with eq. (2.15) and (2.14). Both, the theoretical Walker field H_w^{1d} and the WBD frequency f_{1d} are given in the right plots in Fig. 4.8. The frequencies determined by the 1-d model are roughly a factor of two too high. Thus, the Walker fields calculated with the 1-d model by Le et al. are too small. This is, however, not surprising, because the authors stated that these formulas can only describe DW dynamics in nanostripes with small cross sections. They wrote explicitly that the $20 \times 160 \text{ nm}^2$ nanostripe, which was also used in this study, is too

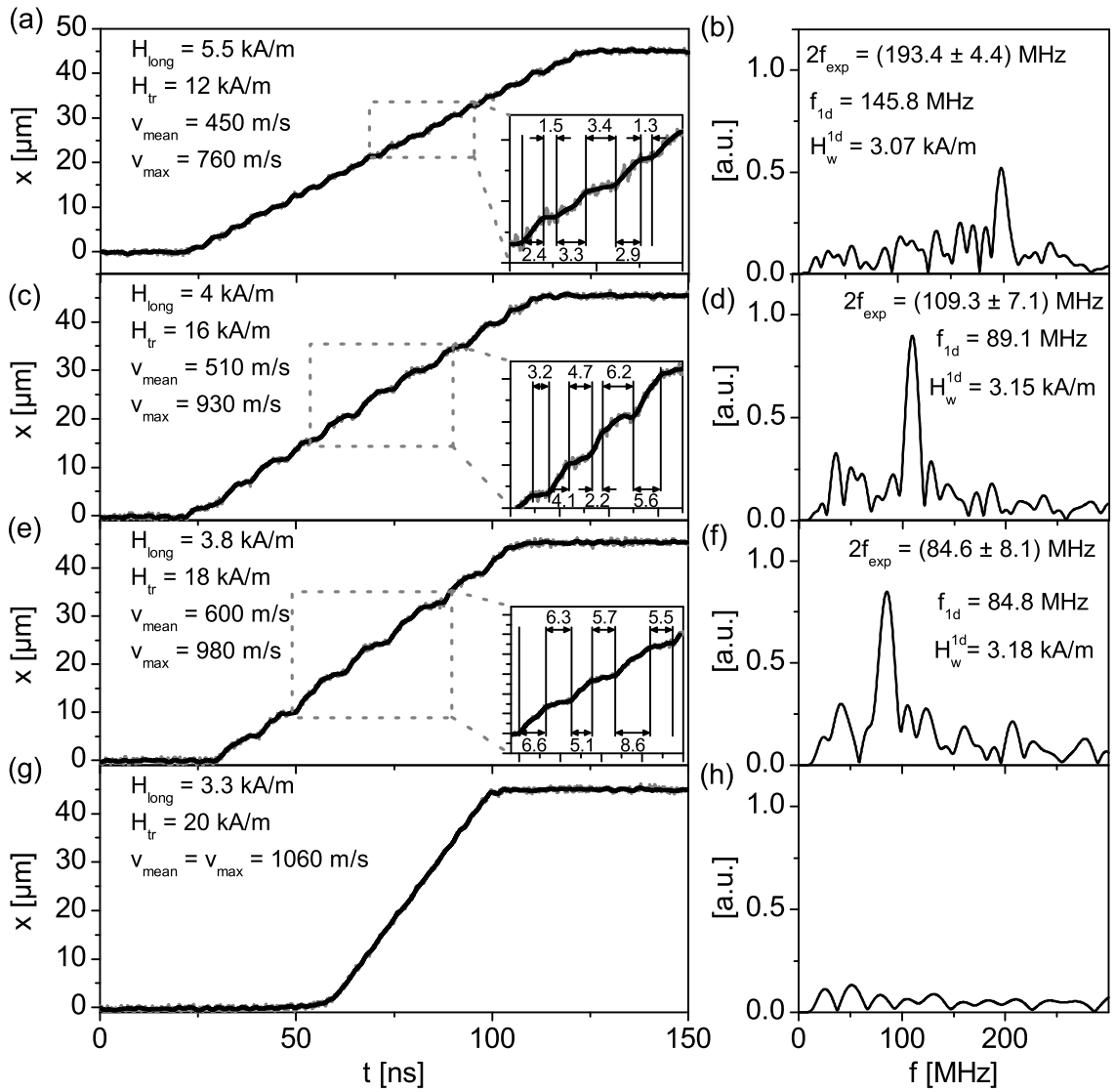


Figure 4.8: Visualization of the WBD with single shot measurements in a $20 \times 250 \text{ nm}^2$ nanostructure under the influence of a transverse field (a,c,e,g) (gray curve - original data; black curve - obtained using a Hamming filter $f_n/f_s = 0.2$, $N = 400$) and its frequency spectrum obtained by a Fourier transform (b,d,f,h). The peak positions $2f_{\text{exp}}$ and width are determined by a Gaussian fit and the theoretical frequency f_{1d} are calculated with eq. (4.2). For the calculation of f_{1d} the H_w values were determined by the model of Lu et al. [39]. The applied fields are denoted at the graphs, whereby the transverse field increases from top to bottom. The insets show a blow up with a horizontal and vertical scale of 10 ns and 5 μm , respectively. The times are given in ns.

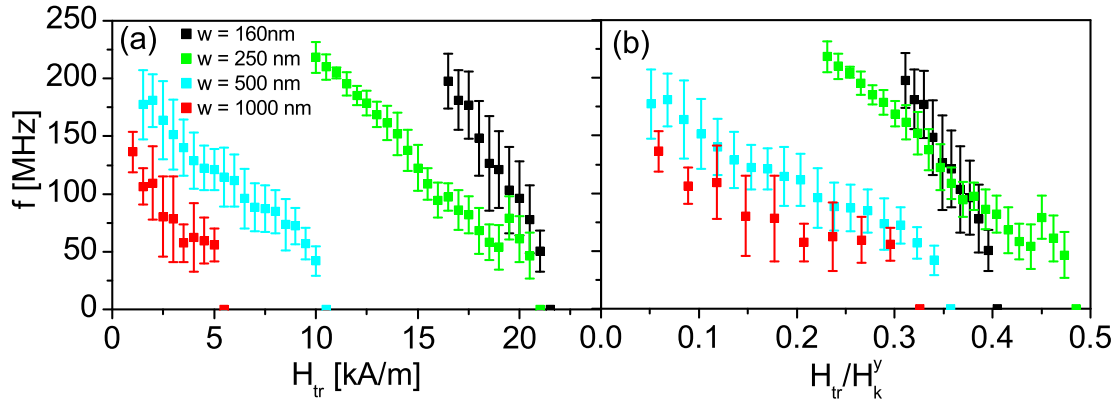


Figure 4.9: Walker frequency as a function of (a) the applied transverse field and (b) the normalized transverse field H_{tr}/H_k^y for several nanostripe width w . The error bars indicate the standard deviation of the observed frequencies for 25 consecutive measurements.

large to be valid for their model.

One might intuitively expect a direct influence of a transverse field on the Walker frequency, too, because H_{tr} breaks the symmetry of the nanostripe in the y -plane preferring one chirality of a TDW. The WBD will become asymmetric as reported by Bryan et al. [37], which in turn can change the frequency of this process. However, up to now there is no theory predicting a change of the Walker frequency with H_{tr} .

Concerning the actual traces of $x(t)$ during the WBD two points are noticeable. First, on average the moving periods in the experiment are larger as compared to the periods of no movement. Second, the behavior during the WBD show neither a significant forward nor a backward movement.

Fig. 4.9 collects the frequencies as a function of (a) the applied transverse field and (b) of the normalized transverse field H_{tr}/H_k^y for several nanostripe width. The values of H_k^y are taken from table 3.1. The error bars denote the standard deviation of 25 consecutive measurements and visualize the statistical variation of the WBD in the GMR nanostripes. One finds a general trend of decreasing frequency with increasing H_{tr} for all nanostripe widths. Interestingly, the WBD is suppressed in a narrow region of the normalized transverse field $H_{tr}/H_k^y = 0.3 - 0.45$. The critical transverse field, where the WBD is suppressed, decreases with increasing nanostripe width. This also holds for H_{tr} normalized to the transverse anisotropy field. Note that the given widths are nominal widths. As stated in section 3.3, the determination of the actual width is

difficult, owing to the complex cross section.

Conclusion Micromagnetic simulations have shown that an edge roughness of the nanostripe increases the Walker field for this stripe. As the Walker field depends on the local distribution of the edge roughness one could have a distribution of H_w leading to a stochastic WBD and a wide frequency band of the WBD which was found to be roughly 80 MHz.

An in-plane transverse field influences the WBD drastically. The main effect is the decrease of the WBD frequency with H_{tr} . This can be understood by two effects: the decrease of the driving field H_{long}^{nuc} and an increase of the Walker field with increasing H_{tr} . However, the available 1-d model [39, 48] does not allow for a good quantitative description of the observed behavior. Beside the influence of H_{tr} on H_w and H_{long}^{nuc} there might be an impact on the frequency of the WBD and thus on the actual behavior during the WBD, too.

4.1.4 Splitting of a dynamic DW

Introduction In the course of investigating the influence of a transverse field on the DW dynamics, a new kind of DW motion was discovered [108]. In the first paragraph of this section the experimental fingerprint of this new mode is introduced and reproduced by means of micromagnetic simulations. The next part explains the physics behind this new motion type and at the end I will give a conclusion.

Experimental verification The experiments were carried out in a $10 \times 300 \times 12000 \text{ nm}^3$ IrMn nanostripe. Fig. 4.10a shows the evolution of the x -magnetization as a function of time which was found for a specific field configuration. The x -magnetization was calculated from the $U(t)$ data with the condition that the whole nanostripe is remagnetized, which is fulfilled most likely. Single shot measurements [108] show that the driving field is below the Walker field $H_{long} < H_w(H_{tr})$. In order to quantify the DW behavior a DW velocity was calculated under the assumption of a rigid DW. The DW velocity changes abruptly during DW motion, between a high and a low velocity regime. The DW starts to move with a high mean velocity of $v_1^{exp} = 800 \text{ m/s}$ and after $9 \mu\text{m}$ the velocity suddenly is changed to $v_2^{exp} = 300 \text{ m/s}$. This was a new dynamic feature which was not reported in experimental and simulative studies. Interestingly this happens below the Walker field, where the DW should move in a steady state regime with a constant DW configuration.

Micromagnetic simulations of a $10 \times 200 \times 6000 \text{ nm}^3$ nanostripe reproduced the experimental findings very well as it is shown in Fig. 4.10b. This behavior was observed in a transverse field of $H_{tr} = 23.9 \text{ kA/m}$ and a driving field of $H_{long} = 4.8 \text{ kA/m}$. To compare these results with the experiments DW velocities were calculated, again under the assumption of a rigid DW. These are comparable to the one found in the experiment. The DW starts with a velocity of $v_1^{sim} = 830 \text{ m/s}$ and changes its velocity abruptly to $v_2^{sim} = 240 \text{ m/s}$. At the beginning of the simulation the DW was positioned $1 \mu\text{m}$ apart from the nanostripe end by means of an artificial notch.

The simulations were performed for perfect nanostripe edges and for a 200 nm wide nanostripe, while in the experiment a 300 nm wide nanostripe with rough edges was used. One would expect a smaller Walker field for the wider nanostripe in the experiment [117], however, the edge roughness increases the Walker field. Thus, the decrease due to the wider nanostripe should be at least partially compensated. However, due to

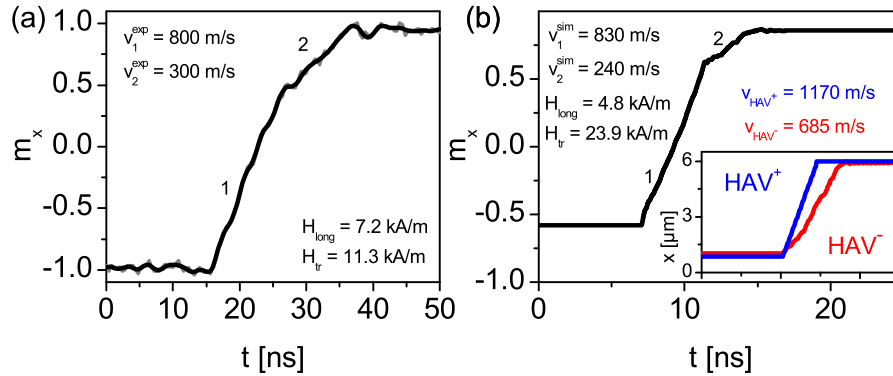


Figure 4.10: Time dependencies of m_x found (a) experimentally in a $10 \times 300 \times 10000 \text{ nm}^3$ nanostripe and (b) simulative in a $10 \times 200 \times 6000 \text{ nm}^3$ nanostripe. The applied fields and the velocities for the two linear $m_x(t)$ parts 1 and 2 are given in the graphs. The velocities were calculated under the assumption of a DW as rigid object for comparison of the experimental and simulative results. The inset in (b) shows the time dependent position of the upper (lower) HAV^+ (HAV^-) with a positive (negative) winding number in blue (red). See Fig. 4.11g for the definition of both HAVs. The mean velocities of both HAVs are determined by a linear fit. The x -scale of the inset is the same as in the main graph.

the strong influence of an edge roughness on the DW dynamics, it is not expected that one finds quantitative agreement of simulation and experiment, even for the same nanostripe width. Therefore, it is not peculiar that the same behavior is found for different field configurations. The simulations were also performed for 300 nm wide nanostripe and this new DW motion type was observed, too. However, the dynamics were much more complicated and therefore the following considerations will be restricted to the 200 nm wide nanostripe.

Explanation by micromagnetic simulation Fig. 4.11a shows snapshots of the simulation which reveal the reason for the abrupt change in the effective DW velocity. Both HAVs, composing the TDW, behave independently as quasiparticles with substantially different mean velocities. Whereby the upper HAV shows a higher velocity as compared to the lower one. When the faster HAV reaches the end of the nanostripe the rest of the nanostripe is remagnetized by the slower HAV, only. This gives rise to this abrupt change in the calculated mean velocity. The inset of Fig. 4.10b shows the time dependencies of the position of both HAVs. A linear fit yields mean velocities of

$v_{H_{AV}^+} = 1170$ m/s and $v_{H_{AV}^-} = 685$ m/s for both HAVs. The reason for the different behavior is connected to the topological charges of the HAVs. Fig. 4.11g shows the relaxed state at $t = 0$ for $H_{tr} = 23.9$ kA/m. The winding number of the upper HAV is positive (see Fig. 2.4a) $n_{H_{AV}^+} = +\frac{1}{2}$, whereby the lower HAV have a negative one $n_{H_{AV}^-} = -\frac{1}{2}$ (see Fig. 2.4b). For large cross sections the symmetry of both edge defects is broken (section 2.1.3), and the positive edge defect is wider as compared to the negative one, which gives rise to a larger stray field energy in the positive edge defect. Below the Walker field the DW velocity depends linearly on the DW width Δ according to eq. (2.19). Therefore, one can intuitively expect different velocities for both HAV, whereby H_{AV}^+ has a higher velocity due to its larger width.

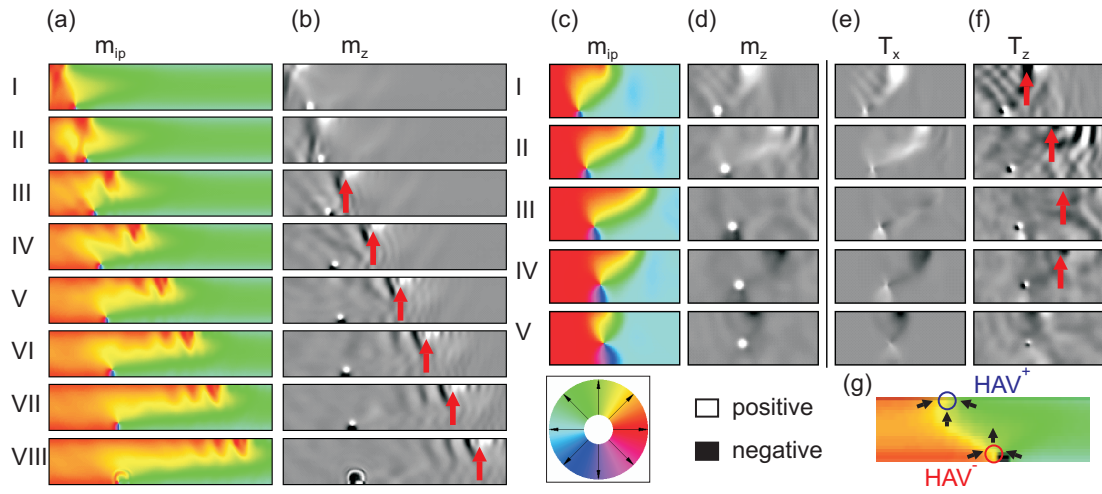


Figure 4.11: Snapshots of the magnetization configuration and torques during DW movement for (a,b) $H_{long} = 4.8$ kA/m, $H_{tr} = 23.9$ kA/m and (c-f) $H_{long} = 4.8$ kA/m, $H_{tr} = 0$ in a $10 \times 200 \times 6000$ nm³ nanostripe. The image show a (a,b) $1 \mu\text{m}$ and (c-f) $0.5 \mu\text{m}$ long part of the nanostripe. The time interval between the images is (a,b) 0.1 ns and (c-f) 0.2 ns. (a,c) shows the in-plane magnetization m_{ip} and (b,d) the out of plane magnetization m_z . In (e) and (f) the x - and the z -projection of the torque is depicted. The red arrows in (b) and (f) show the position of the upper HAV⁺. (g) Magnetic configuration in the relaxed state for $t = 0$ and $H_{tr} = 23.9$ kA/m. The upper HAV⁺ with a positive winding number (see 2.4) and the lower HAV⁻ with a negative winding number are emphasized. Source of (a-f): [108].

A detailed analysis reveals the reason which is more complex. The upper HAV⁺ actually moves with a constant velocity, like it is expected in the regime below the Walker

field and shown in the inset of Fig. 4.10b. At the position of the HAV^- , however, a full antivortex with a winding number of $n = -1$ is nucleated. This is equivalent to the normal WBD (see Fig. 2.6). Contrary to this process the other part of the TDW, the HAV^+ , already moved away from the HAV^- , so that the antivortex cannot traverse the nanostripe. Normally the gyrotropic force moves the antivortex core cross the nanostripe with a parabolic trace [67]. This is not the case in the present DW motion type. The antivortex is pulled back to the nanostripe edge and annihilates under the emission of spin waves leaving the HAV^- behind. As a consequence the HAV^+ shows a linear $m_x(t)$ dependency while for the HAV^- one finds a nonlinear behavior as it can be seen in the inset of Fig. 4.10b. Similar to the WBD, this procedure is repeated continuously. Thus the mean velocity of HAV^- is significantly reduced as compared to v_{HAV^+} .

This situation was not found for $H_{tr} = 0$ in this nanostripe, thus the difference stems from the application of H_{tr} . In order to understand this behavior the WBD process for $H_{tr} = 0$ is recapitulated in detail. Therefore, a second micromagnetic simulation was conducted for the case of zero transverse field and $H_{long} = 4.8 \text{ kA/m} > H_w$ [108]. Snapshots of the magnetic configuration during the WBD are shown in Fig. 4.11c. Both HAVs behave differently, too, because of their different winding number. The HAV^+ is faster and moves away from the HAV^- . The faster HAV, however, is pulled back to the slower one after a certain time. An explanation based on the energies involved in this process is straightforward. The elongation of the DW, due to the different HAV mobilities, increases the exchange energy and decreases the zeeman energy in the system. If the DW is getting too long, the cost in exchange energy overcomes the gain in zeeman energy and the HAV^+ is pulled back to the HAV^- (Fig. 4.11c III-IV). For the case of $H_{tr} = 23.9 \text{ kA/m}$ the DW core magnetization is parallel to the transverse field, which gives an additional source for a gain in zeeman energy as the DW elongates along the x -direction. Above a critical transverse field this gain compensates the cost in exchange energy, stabilizing the elongated DW shown in Fig. 4.11a.

These considerations are only valid for a quasi-static situation if the micromagnetic system can relax to its energy minimum. The small damping parameter for Py of $\alpha = 0.008$ do not allow for a relaxation to the energy minimum and makes DW motion a dynamic problem which is governed by magnetization precession. Therefore, the torques acting on the magnetizations has to be considered.

To understand the new dynamic mode, we will first treat the WBD for zero transverse field in more detail as compared to section 2.1.4. As explained in this section the

driving field for the DW dynamics in nanostripes is the demagnetizing field generated by the oop-magnetization m_z in the DW core region. This assumption is supported by the simulation: the T_x component of the torque is dominated by the demagnetizing field torque (not shown here). The sign of m_z determines the direction of the demagnetizing field and in turn the direction of the torque T_x , which determines the moving direction of the DW. Fig. 4.11d shows m_z in a gray scale plot. At the position of the HAV⁺ we find a positive oop magnetization in row I, giving rise to a positive torque at this position. Therefore, the HAV⁺ moves forward as it is shown in Fig. 4.11c I and II. In the next time step the m_z component is decreased (and therefore the T_x torque, too), which reduces the velocity of the HAV⁺. This reduction in m_z leads in Fig. 4.11d III to a zero oop-magnetization at the HAV⁺ position. As a consequence the HAV⁺ stops.

Fig. 4.11d IV indicates a negative m_z component at the HAV⁺ position in the next time step. This creates a negative T_z torque, pushing the HAV⁺ back to the HAV⁻. The change in the sign of m_z is caused by the torque T_z , which is displayed in Fig. 4.11f. At the position of the HAV⁺ the T_z torque is already negative in the first depicted time step in row I. This pushes the oop-magnetization in the negative direction. A detailed analysis of the T_z torque reveals the reason for its negative sign. The oop-torque T_z stems from the torque of the exchange field T_z^{ex} which overcompensates the demagnetizing field torque T_z^d . In other words: With increasing DW width the torque arising from exchange contributions increases. If this torque overcomes the demagnetizing torque, which pushes the HAV⁺ forward, the HAV⁺ is pulled back to the HAV⁻.

For the case of an applied transverse field the situation changes. H_{tr} influences both, the torques due to the exchange field and the demagnetizing field. The impact of H_{tr} on T_{ex} is thus larger as on T_d . The transverse field tilts the magnetization of the domains in its direction, reducing the DW angle from 180° for $H_{tr} = 0$ (Fig. 4.11c I) to a 120° DW for $H_{tr} = 23.8$ kA/m (Fig. 4.11a I). Because the exchange torque is proportional to the spatial derivative of the magnetization (eq. (2.2)) the amplitude of T_{ex} will be reduced, owing to the smaller DW angle in a transverse field. Above a critical field H_{tr} the negative exchange torque T_z^{ex} cannot overcompensate the positive demagnetizing torque T_z^d any more. Thus, T_z will not become negative at the position of the HAV⁺ which results in a permanent positive m_z (and therefore a positive T_x). The HAV⁺ always moves in the positive x -direction away from the HAV⁻ and the DW is split dynamically.

Note that such a behavior was also found in wider nanostripes without the application of a transverse field. Because the micromagnetic simulation of wider nanostripes is very time consuming, the explanation was done for smaller nanostripes and under the influence of H_{tr} . The fact, that this was also found for wider nanostripes without H_{tr} gives a hint that the transverse field in fact increase the *effective* nanostripe width. The split DW was not found in the $20 \times 160 \text{ nm}^2$ PtMn nanostripes for a wide range of H_{tr} . Thus, the amount of exchange energy would be too large for a stabilized split DW in this small nanostripes even with an applied H_{tr} . It is obvious that the split DW is stable only for a moving DW. If e.g. a pulse field H_{long}^{pulse} , and not a static longitudinal field, is applied additionally to the transverse field, the DW will split, too. However, at the end of the pulse field, the both HAVs will move towards each other, in order to reduce the exchange energy and to attain the global energy minimum of the system.

Conclusion Under conditions below the WBD a new kind of DW motion was found and explained by means of micromagnetic simulations. This dynamically stable split DW could be explained qualitatively via the different torques acting on the magnetizations. The discovery of this mode is important for practical applications like the multiterm counter [21]. It was discussed in the introduction of this thesis, that during DW movement in this application a transverse field is always present during DW movement. Thus, a situation with a split DW can be created in a multiterm. In contrast to the case of a standard TDW, the split TDW has two HAVs which behave differently. This situation could induce problems in terms of DW pinning.

4.1.5 Influence of an in-plane transverse field on the DW dynamics

Introduction In the previous sections the transverse field was used as a tool to alter the nucleation field and the DW behavior. With the help of H_{tr} the frequency of the WBD could be tuned, and a new DW motion type was discovered. In this section the influence of a transverse field on the DW dynamics is analyzed systematically for a larger range of H_{tr} . At the beginning the influence of H_{tr} on a static DW is studied by simulations. In the next part the influence of a transverse field on the nucleation field of a DW in a nanostripe is treated. Based on these fields the velocity spectrum of a DW with an applied H_{tr} is shown. Four different regions in this spectrum will be explained in the adjacent paragraphs.

Influence of H_{tr} on the static DW profile Before dealing with DW dynamics, it is reasonable to clarify the influence of H_{tr} on the static DW profile. Fig. 4.12a shows micromagnetic simulations of a TDW in a $20 \times 160 \text{ nm}^2$ nanostripe under the influence of a transverse field. H_{tr} alters the static DW profile in three ways: An increase of the DW width, a decrease of the DW angle and a deformation of the symmetric TDW. The magnetization components in x - and y -direction, averaged over the y -position, are plotted against x in Fig. 4.12b. The increase of the DW width is illustrated by both curves. As described by Thiaville et al. [48] there is no general definition of the DW width, owing to its complex magnetization structure. A fit of the m_x component with a tanh function, which was proposed in ref. [48], yields significant larger results than expected. Especially for the asymmetric walls the agreement between the simulation and this 1-d model is bad.

In order to get a quantitative measure of Δ two DW widths Δ_{m_x} and Δ_{m_y} were deduced from the m_x or the m_y magnetization components, respectively. They can be determined by the region where $\langle m_i^{DW} \rangle_y$ attains 95% of $\langle m_i^D \rangle_y$ (D - domain). The choice of 95% is somehow arbitrary, however, it gives reasonable results of the DW width. Because of the negative tails in m_y at the border of the DW Δ_{m_y} is larger as compared to Δ_{m_x} (see Fig. 4.12b). Therefore, Δ_{m_x} is used below. The calculated DW widths are normalized to the nanostripe width w and plotted as a function of H_{tr} in Fig. 4.12c. The DW width increases with H_{tr} roughly by a factor of two for an applied transverse field of $H_{tr} = 40 \text{ kA/m}$. According to eq. (2.19) ($v \propto \Delta$) the

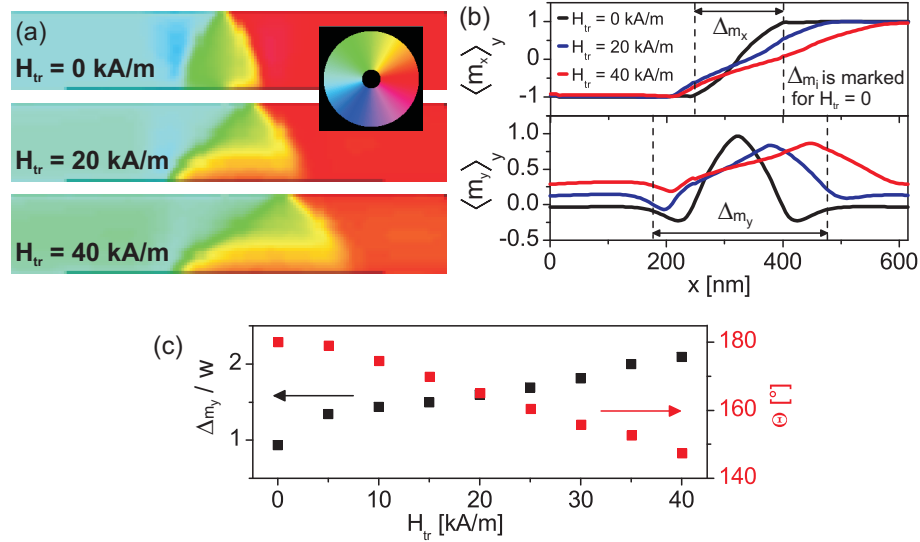


Figure 4.12: Influence of a transverse field on the static DW profile. (a) Micromagnetic simulation of a 20×160 nm² nanostripe under the influence of a transverse field. (b) m_x and m_y averaged over the y -position as a function of x . The DW width Δ is marked for the case of $H_{tr} = 0$. (c) Δ normalized to the nanostripe width w and DW angle as a function of H_{tr} . Δ_{m_x} was determined by the positions, where m_x inside the DW attains 95% of m_x in the domains.

velocity of the DW will be increased by the same amount for $H < H_w$. Note that micromagnetic simulations for 200 nm wide nanostripes yields qualitatively the same results. However, they slightly differs quantitatively from the Δ/w data presented here.

The second change in the magnetization configuration of the DW is the decrease of the DW angle Θ . With increasing H_{tr} the m_y component within the domains increases from 0 to 0.28. Thus, the DW angle changes from 180° to roughly 150° at $H_{tr} = 40$ kA/m and is plotted in Fig. 4.12c.

For $H_{tr} = 0$ the DW is a symmetric TDW, although the vortex wall is the stable configuration for these nanostripe dimensions (see Fig. 2.3). However, as described earlier the TDW can exist in these dimensions as a metastable configuration. The transverse field changes the energetics of this system, so that a asymmetric TDW become the metastable DW. This can be seen in the m_x and m_y plots in Fig. 4.12b. Normally this DW structure occur in nanostripes with larger cross sections as compared to nanostripes with a symmetric TDW (see the phase diagramm in Fig. 2.3). Thus, one could conclude again that H_{tr} increases the effective nanostripe width.

Nucleation field and velocity spectrum After treating the DW statics we will now investigate the influence of H_{tr} on the nucleation process in more detail. The principle impact of H_{tr} on the nucleation field of a DW was treated in section 4.1.2. Two consequences were described: the nucleation field H_{long}^{nuc} and its statistical variation decreased with increasing H_{tr} . Both effects are shown in the red curve of Fig. 4.13a, where the longitudinal component of the nucleation field is plotted against the applied transverse field for a $20 \times 160 \times 45000 \text{ nm}^3$ PtMn nanostripe without a nucleation pad.

The blue curve in the same figure represents the data for a nanostripe with the same dimensions, but a nucleation pad at one end of the nanostripe. Note that the plotted field is called injection field because the DW is nucleated in the nucleation pad for smaller fields and depinned from the nucleation pad - nanostripe intersection at the injection field. The curve significantly differs from the red one. For $H_{tr} = 0$ H_{long}^{nuc} is much smaller as compared to the nanostripe with no nucleation pad, as it is expected. With increasing transverse field the injection field first increases to a maximum at $H_{tr} \approx 8 \text{ kA/m}$ and decreases above this value.

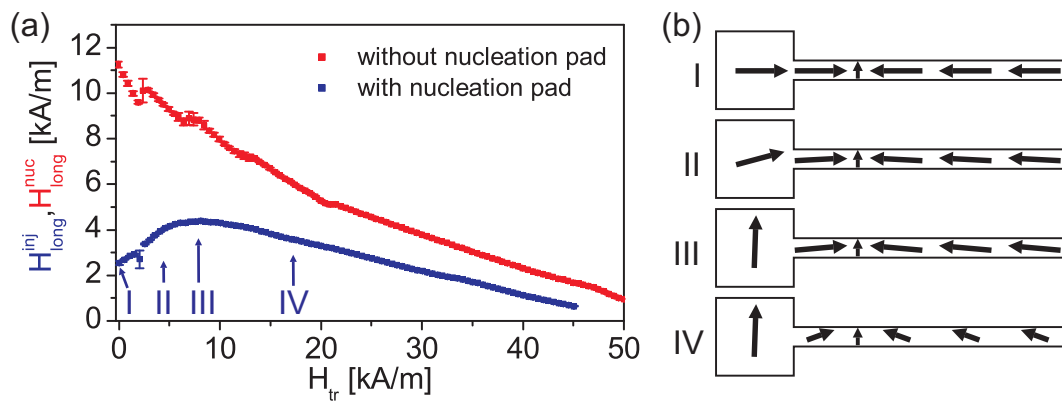


Figure 4.13: (a) Longitudinal component of the nucleation field H_{long}^{nuc} (red) and the injection field H_{inj} (blue) in dependence on the applied transverse field. The plotted values are the arithmetic average of 25 consecutive measurements with its standard deviation. The error of the H_{long}^{nuc} and H_{inj} measurements is mostly smaller than the symbol size. The blue and red curve represents the measurements of a nanostripe with and without a nucleation pad, respectively. (b) shows a schematic of the magnetization directions in the nucleation pad and the nanostripe for four situations marked in (a).

This behavior can be understood by the smaller shape anisotropy in the nucleation pad due to its dimensions of $20 \times 8000 \times 16000 \text{ nm}^3$. The deviation of the magnetization

in the direction of H_{tr} is larger in the nucleation pad as compared to the magnetization in the nanostripe as depicted schematically Fig. 4.13b II. This difference will first increase (Fig. 4.13b II to III), and if the magnetization in the nucleation pad is parallel to H_{tr} this difference decreases (Fig. 4.13b III to IV). The difference of both magnetizations gives rise to additional exchange energy which is necessary to inject a DW in the nanostripe. Therefore, the dependence of the angle between the magnetization in the nucleation pad and the nanostripe is the reason for the dependence of H_{inj} on the applied transverse field.

The two curves in Fig. 4.13a represent the driving fields, at which the DW dynamics could be investigated. The complete $v(H)$ data are shown in Fig. 4.14a. The blue (red) curve is again the nanostripe with (without) a nucleation pad. The direction of increasing transverse field is indicated by an arrow in the inset, showing a blow up of the data. The red curve is subdivided in 4 regions with different DW dynamics. For the blue curve one finds corresponding regions with the same behavior of the DW. These regions will be discussed below:

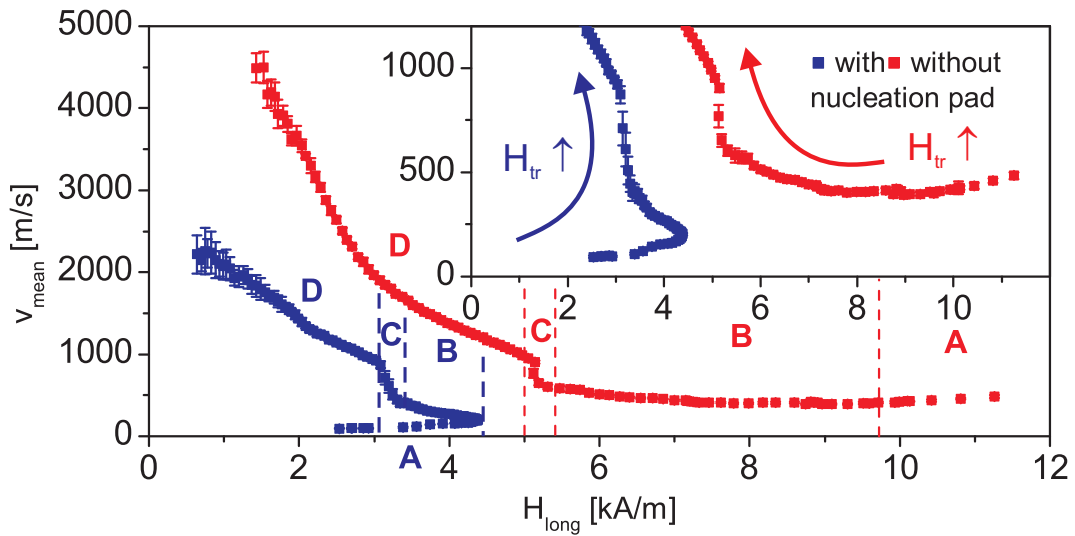


Figure 4.14: Dependence of the v_{DW} on H_{long} for a nanostripe with (blue) and without (red) a nucleation pad. The graph shows the arithmetic average and its standard deviation of 25 consecutive measurements. The error of the DW velocity determination is smaller than the symbol size. 4 regions of different DW behavior are marked with A-D. In the inset, showing a blow up of the data, the direction of increasing H_{tr} is indicated.

Region A The sufficient large variations of H_{long}^{nuc} for small H_{tr} allow to calculate a mobility $\mu = dv/dH_{long}$ of the DW for zero or at least small H_{tr} . Fig. 4.15 a and b show the DW velocities for a nanostripe with and without a nucleation pad, respectively for small transverse fields. The plot depicts 25 measurements for a constant H_{tr} color coded for the different transverse fields. The black data in Fig. 4.15b (nanostripe without a nucleation pad) represents the velocities for the smallest transverse fields, i.e. $H_{tr} \leq 2.5$ kA/m. The velocity data show a linear dependence on the applied H_{long} independently on H_{tr} . The red data points for $3 \text{ kA/m} \leq H_{tr} \leq 3.5 \text{ kA/m}$ are plotted for clarification: these velocity values barely differ from the linear dependence. However, for $H_{tr} \geq 4 \text{ kA/m}$ a significant deviation of the data is found.

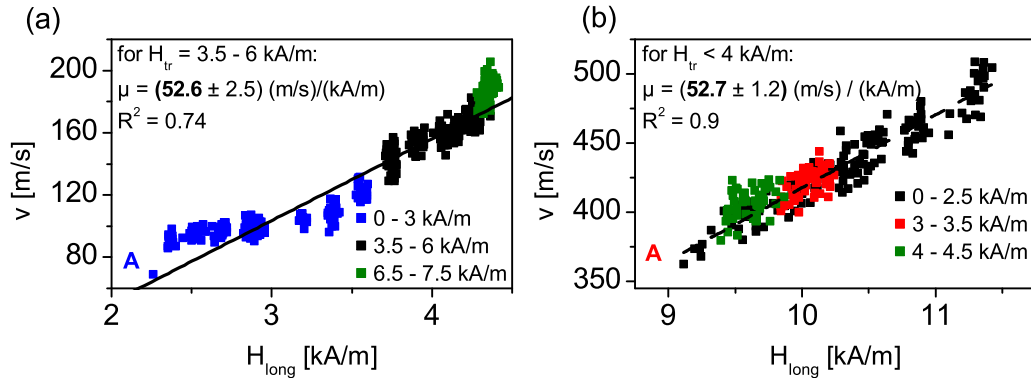


Figure 4.15: (a) and (b) show each of the 25 measurements at constant H_{tr} for the nanostripes with and without a nucleation pad, respectively. Here the measurements for small transverse field are plotted, whereby the different H_{tr} ranges are color coded.

The nanostripe with a nucleation pad shows a different behavior due to the much smaller driving field H_{long} . The blue data in Fig. 4.15a, representing the velocity for small transverse fields, show a weak dependence on H_{long} . This is expected for driving fields slightly above the Walker field (see Fig. 2.7). Above $H_{tr} > 3.5$ kA/m (marked by black symbols) we find a region of constant mobility which matches the one found for the nanostripe without a nucleation pad almost perfectly. For $H_{tr} > 6$ kA/m the velocity data are significantly increased as compared to smaller transverse fields, indicating an influence of the transverse field on the DW dynamics.

The velocity data for a transverse field marked in black and red, define region A: a negligible influence of H_{tr} and a linear dependency of the velocity on the applied

driving field H_{long} . The mobility for both nanostripes in this region is almost equal and accounts for $\mu = (52.6 \pm 2.5) \frac{\text{m/s}}{\text{kA/m}}$ and $\mu = (52.7 \pm 1.2) \frac{\text{m/s}}{\text{kA/m}}$, respectively. Compared to the values found by Beach et al. [23] $\mu_{(H < H_W)} \approx 300 \frac{\text{m/s}}{\text{kA/m}}$ and $\mu_{(H \gg H_W)} \approx 30 \frac{\text{m/s}}{\text{kA/m}}$ the DW movement in our nanostripes is clearly above the Walker field in this region.

Region B According to the red data in Fig. 4.14 this region is attached to region A at smaller longitudinal fields. The positive mobility increases with decreasing driving field H_{long} . There are several reasons for this behavior. First of all the standard DW dynamics shows a transition region, too, where the mobility is first negative and for large longitudinal field starts to increase until it reaches its high field mobility (μ found in region A) Fig. 2.7. This behavior is, however, changed by the applied transverse field which enhances the DW mobility even more.

The blue curve in Fig. 4.14 reveals this enhancement. Because of the dependence of H_{long} on H_{tr} , with the maximum at $H_{long} = 4.7 \text{ kA/m}$, we have velocity data for the same longitudinal field but different transverse fields. The region $3.7 \text{ kA/m} \leq H_{long} \leq 4.7 \text{ kA/m}$ represents region B for this curve and we can study the influence of H_{tr} on the mobility with these data. Fig. 4.16a shows the change of the mobility ratio $\frac{\mu(H_{tr}^{high}) - \mu(H_{tr}^{low})}{\mu(H_{tr}^{low})}$ as a function of the change in the applied transverse field. For the analysis I used velocity values with the same driving field, but different transverse fields, namely H_{tr}^{high} and H_{tr}^{low} . With this velocities I calculated the differential mobility $\mu = dv/dH_{long}$. Because of different velocities for the same H_{long} one gets different mobilities depending on the applied transverse field. The change of the mobility ratio shows two regimes. For small differences in the transverse fields it increases linearly with a slope of 0.079 kA/m^{-1} , and for larger ΔH_{tr} the mobility ratio increases much faster.

In order to understand this behavior one can calculate the mobility using the 1-d model. The mobility above the Walker field can be expressed by $\mu = \Delta\gamma_0/(\alpha + \alpha^{-1})$ (see eq. (2.22)). It was discussed in Fig. 4.12 that H_{tr} increases the DW width by roughly a factor of two for $H_{tr} = 40 \text{ kA/m}$. The second impact of H_{tr} on the static DW profile was the decrease of the DW angle. There is no analytical theory which calculates the DW velocity above the Walker field under the influence of a transverse field including the decrease of the DW angle. Bryan et al. gave the formula (4.3) for the DW velocity *below* the Walker field. It includes the change of the DW angle Θ via the angle, the domain magnetization makes with the nanostripe axis ϑ ($\Theta = 180^\circ -$

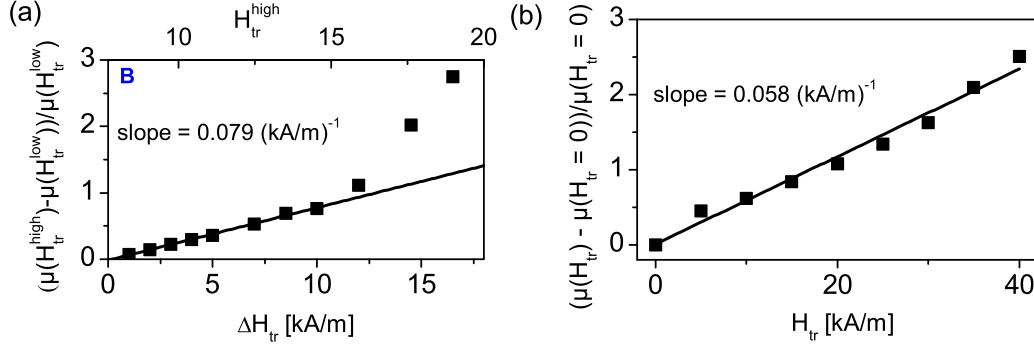


Figure 4.16: (a) Dependence of the mobility ratio $\frac{\mu(H_{tr}^{high}) - \mu(H_{tr}^{low})}{\mu(H_{tr}^{low})}$ on ΔH_{tr} calculated with the data of the blue curve in Fig. 4.14 for $3.7 \text{ kA/m} \leq H_{long} \leq 4.7 \text{ kA/m}$. $\mu(H_{tr}^{low})$ and $\mu(H_{tr}^{high})$ denotes the mobility at the lower and higher transverse field for the same longitudinal field. The transverse field H_{tr}^{high} is depicted in the upper x -axis. (b) Dependency of the mobility ratio $\frac{\mu(H_{tr}) - \mu(H_{tr=0})}{\mu(H_{tr=0})}$ on the applied transverse field as calculated by the model by Bryan et al. [37] using the DW width and DW angle deduced from Fig. 4.12.

2ϑ) [37]. The mobility of the DW was calculated with eq. (4.3) using the data of the quasi-static simulations given in Fig. 4.12c. Fig. 4.16b shows the ratio of the mobility $\frac{\mu(H_{tr}) - \mu(H_{tr=0})}{\mu(H_{tr=0})}$ as a function of the applied transverse field. The dependency shows a linear behavior, too, and the slope is estimated to be 0.058 kA/m^{-1} . As this slope is comparable to the experimentally found one (0.079 kA/m^{-1}), the increase of the mobility with H_{tr} can be explained with the change of Δ and Θ .

$$v = \left[\frac{2\cos\vartheta}{2 - (\Pi - 2\vartheta)\tan\vartheta} \right] \frac{\gamma_0}{\alpha} \Delta H_{long} \quad (4.3)$$

Eq. (4.3) is valid for $H_{long} < H_w$. However, if one compares the eqs. (2.19) and (2.22) describing the $v - H$ dependencies below and above H_w , respectively, the difference stems from the damping parameter α only. Therefore, one could suggest, that the principle structure of an equation, describing the $v - H$ dependency above the Walker field under the influence of H_{tr} , should be the same as eq. (4.3).

The increase of the linear slope for larger transverse fields in Fig. 4.16a cannot be explained by the increase of Δ and the decrease of Θ . Additionally one can suggest an increase of the Walker field with H_{tr} , which would lead to a higher velocity, too. Bryan et al. [37] reported an increase (decrease) of H_w with H_{tr} for an antiparallel (parallel)

alignment of M_{core} with H_{tr} . Thus, one has to assume an antiparallel alignment of M_{core} and H_{tr} in order to get an increased Walker field. This is somehow counterintuitive, however, an increase of the Walker field in the measurements presented here is doubtless as I will show in the description in the next section.

Region C In region C the mean velocity of the DW increases sharply with decreasing driving field by roughly a factor of two as it can be seen by the red data in Fig. 4.14. Single shot measurements of the DW movement in the nanostripe without a nucleation pad reveal the reason for this sudden increase. Fig. 4.17 shows three measurements for different applied field configurations. The brown curve is the measurement with the largest $H_{long} = 5.3$ kA/m and smallest $H_{tr} = 20.5$ kA/m. Clearly this measurement is above the Walker field because several Walker events are observed. The maximum velocity between the Walker events accounts for $v_{max} = 900$ m/s, while the mean velocity of the DW is significantly reduced $v_{mean} = 680$ m/s, due to the WBD. If one increases the transverse field by 0.5 kA/m, the longitudinal field decreases to $H_{long} = 5.0$ kA/m. The dynamics change substantially by a decreased number of Walker events. As a consequence the mean velocity increases to $v_{mean} = 740$ m/s, while the maximum velocity interestingly remains constant at $v_{max} = 900$ m/s. Increasing the transverse field by another 0.5 kA/m the longitudinal field is changed only marginal to $H_{long} = 4.9$ kA/m and the WBD is suppressed completely. The maximum velocity, which hardly changed to $v_{max} = 920$ m/s, is now identical to the mean velocity. Thus, the sharp increase of the DW mean velocity in region C is only caused by the suppression of the WBD.

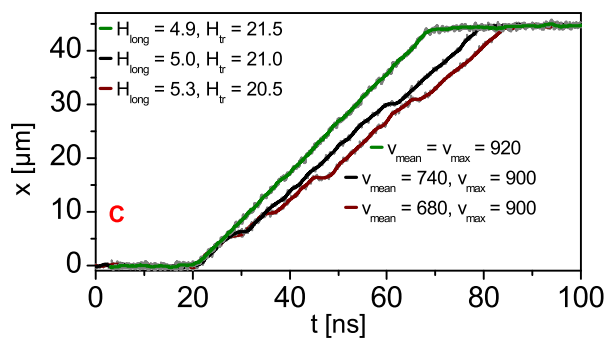


Figure 4.17: $x(t)$ dependencies in region C. The field and velocity values are given in kA/m and m/s.

The Walker field determined by the single shot measurements in nanostripes with a nominal identical cross section is $H_w = 3.09$ kA/m and $H_w = 5.14$ kA/m for the nanostripe with and without the nucleation pad, respectively. This fact suggests a larger impact of H_{tr} on the suppression of the WBD than H_{long} . This is supported by the fact that the WBD is suppressed at the same H_{tr} for both nanostripes (but different H_{long}).

The data of the nanostripe with a nucleation pad give a direct evidence of an increased Walker field with the applied transverse field. For a longitudinal field smaller than the Walker field of this nanostripe, estimated to be $H_{long} < H_w = 3.09$ kA/m at $H_{tr} = 22$ kA/m, there are velocity data below and above the WBD (see the blue curve in Fig. 4.14). For small transverse fields it was shown that the data indicate $H_{long} < H_w$, i.e. $H_w < 2.5$ kA/m at $H_{tr} = 1.5$ kA/m. On the other hand it was shown that for $H_{tr} = 22$ kA/m the Walker field is $H_w = 3.09$ kA/m. Thus, the Walker field is increased at least by 0.6 kA/m for a change of the transverse field of roughly $\Delta H_{tr} \approx 20$ kA/m.

Region D This region includes the DW dynamics below the Walker field. For the case of $H_{tr} = 0$ one gets a linear dependency of the DW velocity on the driving field with a positive mobility (see Fig. 2.7). Under the influence of an increasing transverse field one observes a nonlinear increase with decreasing H_{long} as it can be seen for the red plot in Fig. 4.14. The highest velocity in this region is $v_{max} = 4500$ m/s, which is the fastest DW movement in nanostripes reported up to now [109]. The velocity data in this region for the nanostripe with a nucleation pad show this nonlinear increase, too. The highest velocities are smaller than the one found in the nanostripe without a nucleation pad. This can be explained by the smaller longitudinal field at the same transverse field for the blue curve.

The differential mobility, normalized to the mobility at the Walker field H_w , is plotted against the applied transverse field in Fig. 4.18a. The reasons for the increase are again the increased DW width and the decrease of the DW angle, as it was discussed in region B. The DW width and angle in dependence on the applied transverse field found in the micromagnetic simulations in Fig. 4.12 cannot explain this nonlinear increase as it is shown in the dependence of the mobility ratio on H_{tr} in Fig. 4.16. However, the bracketed factor of the underlying formula (4.3) shows a nonlinear increase for *smaller* DW angle Θ , too. This is shown in Fig. 4.18b.

This strongly decreased DW angle can be explained by the slanted edges of the PtMn

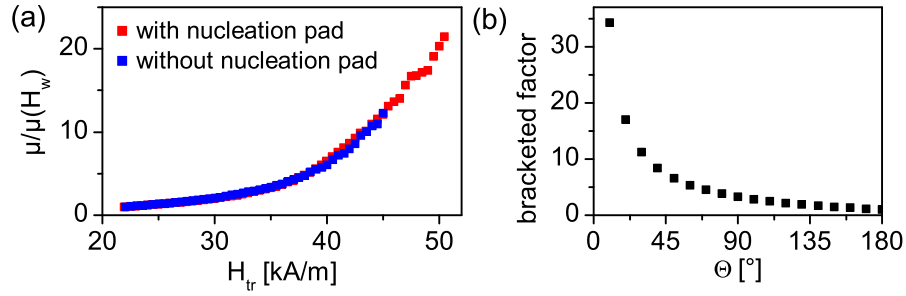


Figure 4.18: (a) Differential mobility $\mu = dv/dH$ normalized to the mobility at H_w as a function of the applied transverse field. (b) Bracketed factor of eq. (4.3) as a function of the DW angle Θ .

stack (see Fig. 3.3). As it will be explained in the next section the transverse anisotropy is decreased for slanted edges as compared to rectangular edges. The reason for this is the decrease of the surface charge density $\sigma_s = \mathbf{m} \cdot \mathbf{n}$, with \mathbf{n} as surface normal. For slanted edges a magnetization \mathbf{m} in the y -direction will not be parallel to the surface normal which decreases the surface charges and in turn the demagnetizing energy. Thus, the y -magnetization will be larger for the nanostripe with slanted edges as compared to the rectangular cross section for the same applied transverse field. In addition the DW width will also increase. Therefore, one can assume smaller DW angles and wider DWs for the nanostripe used in the experiments as compared to the micromagnetic simulation of the nanostripe with the same dimensions but with a rectangular cross section.

In summary the application of a transverse field below the WBD increases the DW mobility drastically. The highest velocities found in these samples were 4500 m/s, which are the highest reported up to now [109].

Conclusion This section treated the influence of an in-plane transverse field on the DW statics as well as on the DW dynamics. Two main changes of the DW profile are reported, first an increase of the DW width and second a decrease of the DW angle. For the investigations of the DW dynamics I investigated a nanostripe with and without a nucleation pad. The dependence of H_{long}^{nuc} on H_{tr} was used to explore the dynamics in a wide field range, because H_{long}^{nuc} is the driving field of the DW, too. As a consequence one has to calculate with the mobility $\mu = dv/dH_{long}$ in order to separate the influence of H_{tr} and H_{long} in the DW dynamics.

Four different regions were separated and discussed in detail. For small transverse fields one finds a region of negligible influence of H_{tr} on the DW mobility, which accounts for $\mu \approx 53 \frac{\text{m/s}}{\text{kA/m}}$ for both nanostripes. This value stems from a driving field which is clearly above the critical Walker field. For increasing H_{tr} the mobility increases, too. Both region B and D for $H_{long} > H_w$ and $H_{long} < H_w$, respectively showed a nonlinear increase, which could be explained by the change of the two DW parameters, the DW width and the DW angle. The highest DW velocities found here account for 4500 m/s, which is three times the highest DW velocity reported before [22]. In between these two regions the WBD is suppressed leading to an increase of the DW velocity (and the mobility) by a factor of roughly two.

In summary the velocities under the influence of H_{tr} are generally larger as compared to the case of $H_{tr} = 0$. This leads to a higher possible operation frequency of any device where DWs are controlled by a rotating magnetic field, which causes the existence of a transverse field during DW movement.

4.1.6 Influence of the real shape on the DW dynamics

Introduction It was already pointed out, that the real shape of the nanostripe substantially changes the DW dynamics from the ideal rectangular nanostripe. Thiaville et al. [105] reported a suppression of the Walker field by means of an edge roughness. In section 4.1.3 it was shown that the frequency band of the WBD is wider and the Walker field is increased in nanostripes with rough edges. Besides a certain edge roughness the nanostripes will not have a perfectly rectangular cross section. As shown in Fig. 3.3 the PtMn samples in this study exhibit slanted edges, due to an etch process under a certain angle during their patterning process. There are few papers dealing with the influence of slanted edges on the shape anisotropy [122] and on ferromagnetic resonance [123–125]. The influence on the DW dynamics, especially the WBD, is the topic of the next section.

In the first paragraph the experimental configuration used to investigate the influence of the real cross section on the DW dynamics are introduced. Especially the consequence of the different configurations for the behavior during the WBD will be explained. In the second paragraph the experimental results will be presented. I will give the reasons for the observed behavior in the last part.

Experimental configuration The investigations were carried out on $20 \times 160 \text{ nm}^2$ PtMn nanostripes with a nucleation pad. Basically similar measurements as described in the previous section were performed. However, I conducted in total four different measurements using the polarity of both, the longitudinal and transverse field. H_{tr} was used to determine the direction of the DW core magnetization. At sufficient large transverse fields, a DW with a core magnetization parallel to H_{tr} will be nucleated as it was discussed in the previous section 4.1.2. The longitudinal field determines whether a head-to-head (HH) DW or a tail-to-tail (TT) DW will be nucleated because the DW will always be nucleated at the nucleation pad.

Fig. 4.19 a, b shows two of the four possible configurations. A HH DW with a positive core magnetization (a), a TT wall with a negative core magnetization (b), hereafter called configuration 1 and 2. Note that the HAVs are located at the same position for these two configurations, namely the HAV^+ at the upper and the HAV^- at the lower edge. Thus, the triangle of the TDW has the same orientation for both configurations. It was explained in section 2.1.4 that the location of the HAVs determines the behavior

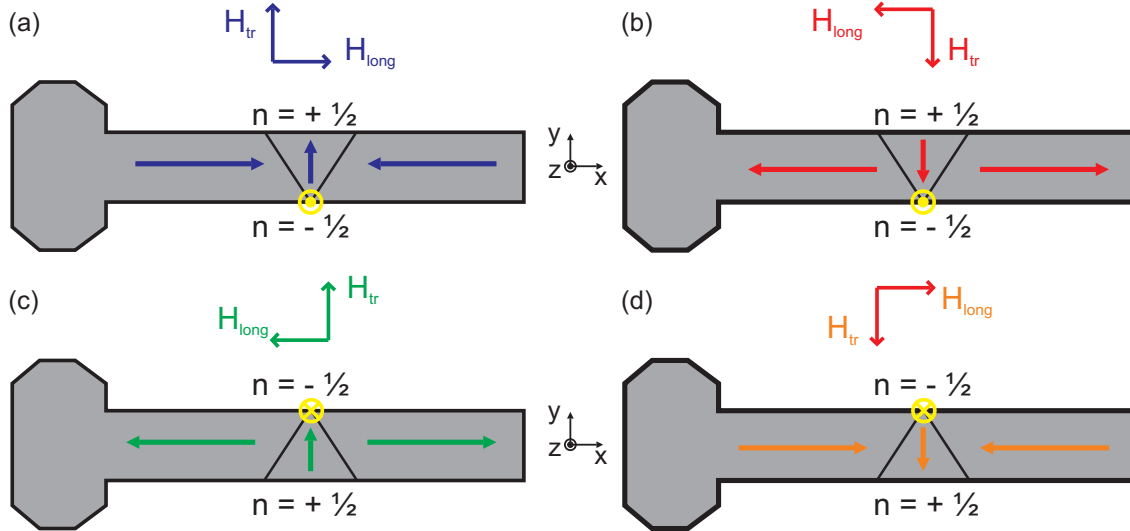


Figure 4.19: Four different configurations for the measurements of the DW dynamics in dependence on the directions of the longitudinal and transverse field. The positions and the value of the topological charges are depicted according to their definition in Fig. 2.4. The yellow marks indicate the position of the antivortex nucleation and its core polarity.

during the WBD. In dependence on the nanostructure dimensions an antivortex or vortex is nucleated at the position of the HAV^+ and HAV^- , respectively [67]. In the nanostructure used in this experiment ($20 \times 160 \text{ nm}^2$) an antivortex will be nucleated at the HAV^- at the lower edge for both configurations.

The polarity of the antivortex core is determined by the torque $\mathbf{T} = -\mathbf{m} \times \mathbf{H}_{eff}$ acting on the DW core magnetization m_{core} by the effective field. The z -component of \mathbf{T} , which is responsible for the polarity of the oop-magnetization, is mainly caused by the applied longitudinal field. Because both, the direction of m_{core} and H_{long} , change in comparison of configuration 1 and 2, the direction of T_z will be positive for both configurations. As a consequence the antivortex core will have a positive core magnetization in both situations (see yellow marks in Fig. 4.19 a, b).

The two remaining configurations are depicted in 4.19 c, d. Both show the same orientation of the TDW, too. Here the positive HAV is located at the lower edge and the negative one at the upper edge. Therefore, the antivortex is nucleated at the upper edge and its core magnetization will be negative. These two match the configurations sketched in Fig. 4.19 a, b in terms of the following considerations and are omitted below.

Experimental results Fig. 4.20a shows the measurement of H_{tr} and v as a function of the applied H_{long} . The measurement scheme was the same described in the previous section 4.1.5. Thus, the measurement would suggest to plot H_{long} as a function of H_{tr} because the longitudinal field is changed by H_{tr} . However, the transverse field is only a tool to set the TDW core magnetization and its impact on the DW dynamics is not the topic of this section. Because commonly the velocity is plotted against H_{long} , H_{tr} was plotted as a function of H_{long} for convenience. The blue and red line in Fig. 4.20a represents configuration 1 and 2 and shows the applied transverse field for a range of H_{long} between $2.6 \text{ kA/m} < H_{long} < 4.3 \text{ kA/m}$. The value of the applied field $H_{ext} = \sqrt{H_{long}^2 + H_{tr}^2}$ is almost the same for both configuration between $2.6 \text{ kA/m} < H_{long} < 3.7 \text{ kA/m}$. Thus, the influence of H_{tr} on the DW dynamics will be the same for both configurations.

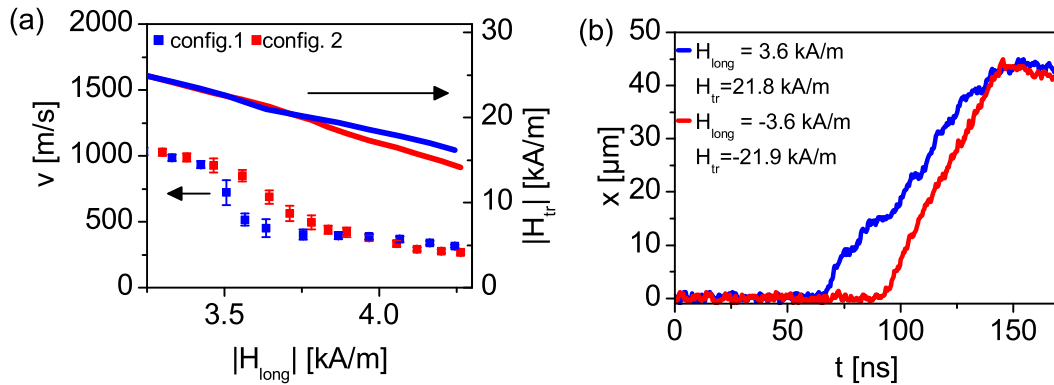


Figure 4.20: (a) Transverse field and DW velocity as a function of the longitudinal field for configuration 1 and 2 (see Fig. 4.19a,b). The data points show the arithmetic average and the standard deviation of 25 consecutive measurements. The error bars for the H_{tr} values are smaller than the symbol size. (b) Single shot measurements with the DPO 4032 oscilloscope (see table 4.1) for both configurations for the applied field values as indicated.

The rectangles in Fig. 4.20a show the DW velocity in dependence on H_{long} for configuration 1 and 2 in blue and red, respectively. The data show the typical behavior explained in the last section. For small H_{long} (and thus large H_{tr}) the DW is in the regime below the WBD with a high velocity. With increasing H_{long} v_{mean} drops by a factor of two which corresponds to the suppression of the WBD in region C of the previous section. For higher fields H_{long} the DW is in the low velocity regime and thus $H_{long} > H_w$.

The velocity is almost equal for both configurations for $H_{long} < H_w \approx 3.4$ kA/m, but there is a significant difference for $H_{long} > 3.4$ kA/m. For $H_{long} > 4$ kA/m the higher velocity of the blue configuration 1 stems from the higher transverse field for this configuration. A transverse field increases the mean velocity of a DW below and above the Walker field, as explained in the previous section. If H_{tr} is higher for configuration 1 the mean velocity will be higher, too.

The difference in the velocity for the field range 3.5 kA/m $< H_{long} < 3.8$ kA/m cannot be explained by a difference in H_{tr} . The reason for the different velocities can only be explained by different Walker fields for both configurations. The velocity breakdown for the blue curve (configuration 1) occurs for smaller fields as compared to the red curve (configuration 2). Thus, we find a higher Walker field for configuration 2. Single shot measurements in this region confirm this suggestions. Fig. 4.20b shows single shot measurements of the DW movement for both configurations for $|H_{long}| = 3.6$ kA/m. The red configuration 2 is still in the steady state regime, i.e. showing a linear position-time dependence. The blue configuration 1, on the other hand, shows the stop-and-go movement typical for the WBD. By analyzing the single shot measurements, the Walker field could be estimated for both configurations to be $H_w^{\textcircled{1}} = 3.4$ kA/m and $H_w^{\textcircled{2}} = 3.7$ kA/m, respectively.

Concluding there are different Walker fields in the same nanostripe (and thus the same edge roughness) depending on the magnetization configuration of the TDW at the beginning of the DW motion. This can not be understood by the 1-d model, where the Walker field simply depends on the transverse anisotropy field $H_k^z = (N_z - N_y)M_s$ (see eq. (2.17)), which is the same for both configurations.

Analytical Theory The reason for the different H_w in the same sample lies in the cross section of the nanostripe. If one considers the dynamic process of the Walker breakdown the symmetry is broken due to the trapezoid cross section. As shown in Fig. 3.3 the PtMn nanostripe has a complex cross section with a base angle varying with the z -coordinate between $\alpha = 30^\circ \dots 80^\circ$ due to the etching process under tilt. It was already pointed out that for both configurations an antivortex with the same polarity is nucleated at the initiation of the WBD. The difference of this two configurations concerning the Walker field stems from the different stray field contributions in dependence on the rotation senses of the TDW core magnetization when an antivortex is nucleated. Namely for configuration 1 and 2 the magnetization rotates ccw and cw,

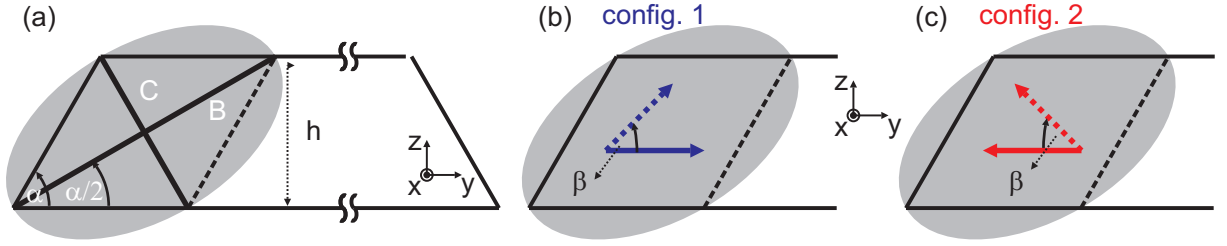


Figure 4.21: Schematic of the nanostripe cross section with a trapezoid shape. The edge region can be approximated by an elliptical cylinder having its long axis along the x -direction. The major and minor axis of the ellipse are defined in (a). (b) and (c) shows the rotation sense of rotation for the TDW core magnetization for the two configurations.

respectively as it is shown in Fig. 4.21b and c.

The stray field energy per volume in the edge region, which is generated by the oop rotation of the TDW core magnetization, can be estimated analytically if one approximates the trapezoid in the edge region of the slanted nanostripe with an elliptic cylinder. Like it is shown in Fig. 4.21a the long axis of the ellipse in the cross section (labeled as B in figure 4.21a) lies along $\alpha/2$. The hard axis C is perpendicular to B as depicted in Fig. 4.21a and the long axis of the cylinder A is parallel to the x -direction. For an elliptic cylinder the demagnetizing factors N_i can be calculated straight forward by eq. (4.6) [126].

$$N_A = 0 \quad (4.4)$$

$$N_B = \frac{c}{b+c} \quad (4.5)$$

$$N_C = \frac{b}{b+c} \quad (4.6)$$

The length of the major and minor axis of the ellipse depend on the base angle α and the height of the Py layer h . They can be expressed by:

$$b = \frac{h}{\sin(\alpha/2)} \quad (4.7)$$

$$c = \frac{h}{\cos(\alpha/2)} \quad (4.8)$$

Therefore, the demagnetizing tensor has the following form.

$$\mathbf{N} = \begin{pmatrix} 0 & 0 & 0 \\ 0 & \frac{\sin(\alpha/2)}{\sin(\alpha/2)+\cos(\alpha/2)} & 0 \\ 0 & 0 & \frac{\cos(\alpha/2)}{\cos(\alpha/2)+\cos(\alpha/2)} \end{pmatrix} \quad (4.9)$$

According to Ref. [45] the demagnetizing energy for an ellipsoid is given by:

$$E_d = \frac{\mu_0}{2} M_s^2 V \mathbf{m}^T \cdot \mathbf{N} \cdot \mathbf{m} \quad (4.10)$$

The magnetization of the TDW core \mathbf{m} with respect to the long major of the ellipse is:

$$\mathbf{m} = \begin{pmatrix} 0 \\ \cos(\beta - \frac{\alpha}{2}) \\ \sin(\beta - \frac{\alpha}{2}) \end{pmatrix} \quad (4.11)$$

Summarizing eqs. (4.9)-(4.11) one gets the normalized stray field energy as a function of the base angle α and the magnetization angle β .

$$\frac{E_d}{\frac{\mu_0}{2} M_s^2 V} = \frac{\cos^2(\beta - \frac{\alpha}{2}) \sin(\frac{\alpha}{2}) + \sin^2(\beta - \frac{\alpha}{2}) \cos(\frac{\alpha}{2})}{\sin(\frac{\alpha}{2}) + \cos(\frac{\alpha}{2})} \quad (4.12)$$

Fig. 4.22 shows the dependence of the normalized stray field on the oop magnetization angle β for a base angle of $\alpha = 30^\circ$ and 60° , respectively. In order to nucleate an antivortex, giving rise to the inset of the WBD, the magnetization has to be rotated by 90° out-of-plane. For the red configuration the stray field energy has a maximum below 90° , while the blue configuration shows its stray field maximum at 90° . Thus, it should be energetically easier to rotate the magnetization oop in the blue configuration. From this point of view it appears straightforward that the blue configuration 1 will lead to a smaller Walker field as compared to the red configuration. A change in the base angle α from 30° to 60° reduces the maximum for the red configuration and changes its position. However, the qualitative behavior is not changed.

Owing to the complex cross section, depicted in Fig. 3.3, the different Walker fields can be explained by the difference in the stray field contribution in the nanostripe edge region.

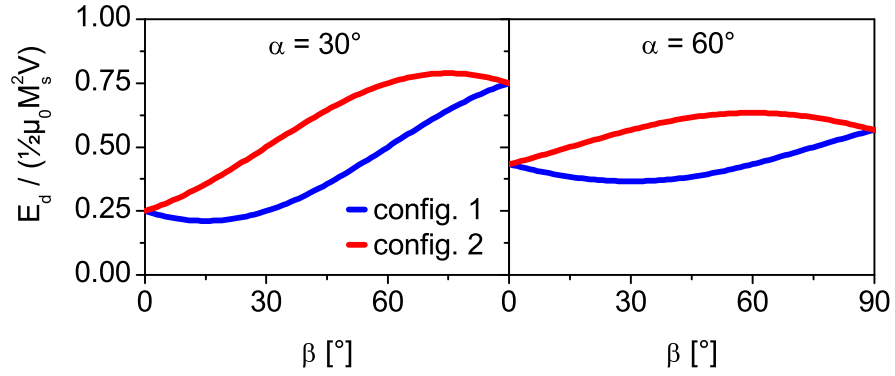


Figure 4.22: The normalized stray field contribution according to eq. (4.12) is plotted against the oop angle β .

Conclusion It was shown that the real shape of the nanostripe significantly influence the DW dynamics. In dependence on the actual DW configuration two Walker fields were experimentally verified in the same sample. These account for $H_w^\ominus = 3.4$ kA/m and $H_w^\oplus = 3.7$ kA/m, respectively. This behavior could be qualitatively explained by an 1-d model which calculates the stray field energy generated by the DW core magnetization during the DW dynamics.

4.2 Pinning of DWs

In this section the quasi-static phenomenon of pinning and depinning is treated. This topic is of crucial importance for any application because a DW pinned by an imperfection of the nanostripe can lead to a malfunction of a device. As a consequence there are lots of publications dealing with this topic (e.g. [127–132]). However, the influence of a transverse field on the DW pinning has barely been treated [133, 134], and moreover the applied transverse fields are rather small in the range of some kA/m. For applications like the multiturn counter the applied transverse fields during DW propagation will be in the range of $H_{tr} = 10 - 35$ kA/m [21]. The influence of transverse fields up to 50 kA/m on the DW pinning and depinning will be treated in this section.

First the experimental instrumentation used for this investigation is introduced. The next part shows the experimental results. They can be understood by means of micro-magnetic simulations and the results of the previous sections. At the end I will give a summary of this section.

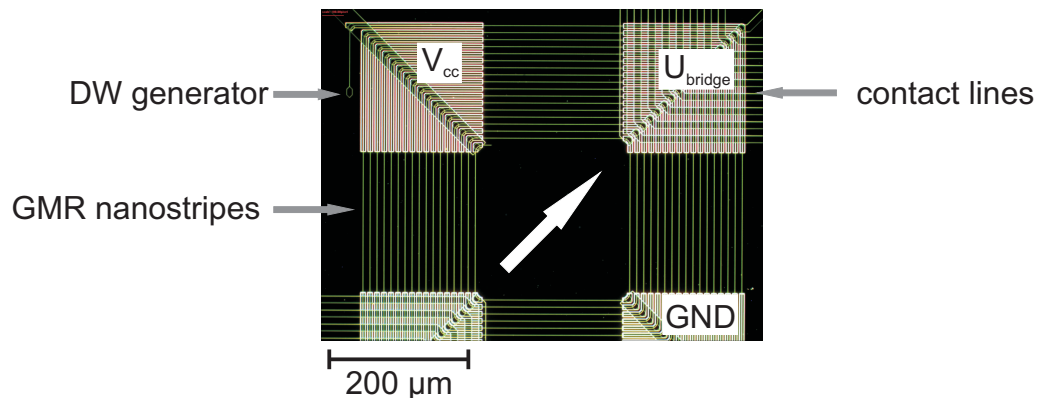


Figure 4.23: Dark field image of a multiturn chip. The white arrow displays the reference direction, which is in 45° with respect to the straight parts of the nanostripes. The spiral is electrical connected in a half bridge geometry.

4.2.1 Experimental instrumentation

For the investigations a multiturn counter [21] was used, like it is shown in Fig. 4.23. The GMR nanostripes are patterned in a rectangular spiral. The reference direction points along the diagonal of the rectangles. In order to determine the existence and

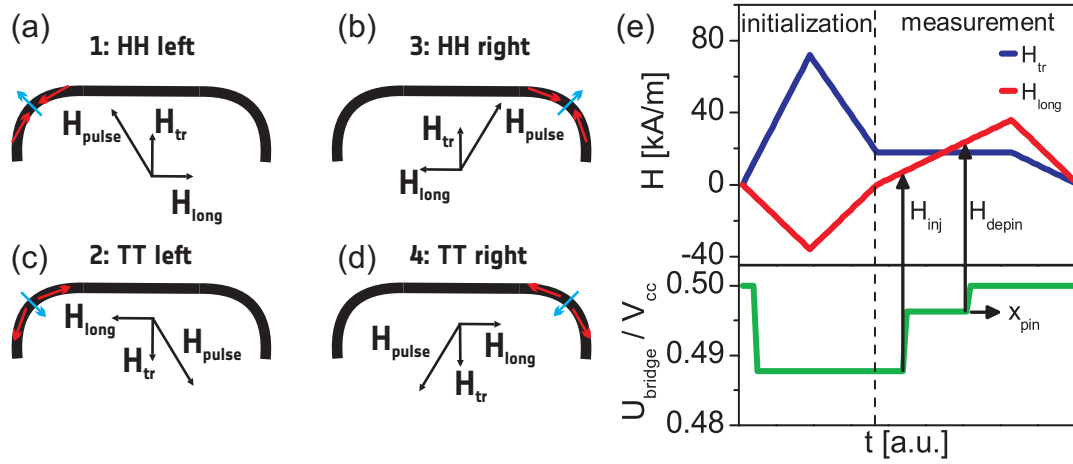


Figure 4.24: (a-d) Schematic of the measurement scheme with the four possible combinations of H_{long} and H_{tr} . The blue (red) arrows indicate the DW core (domain) magnetization after the initialization. (e) shows the signal traces for one measurement. In the initialization phase a field pulse is applied positioning a DW in a corner. During the measurement a constant transverse field is applied and the longitudinal field is increased linearly. Using the voltage bridge signal one can determine the pinning positions x_{pin} and the depinning field H_{depin} .

position of a DW in the spiral a Wheatstone half bridge was used. The distance between two contacts, i.e. the measurement region, was $200 \mu\text{m}$.

The measurement scheme is depicted in Fig. 4.24e. First a field pulse was applied in order to nucleate a DW in the corner of the spiral. Second the desired constant transverse field is applied and the longitudinal field is increased. During the increase of H_{long} the DW is first depinned from the nucleation position in the corner at the injection field H_{inj} , eventually pinned in the nanostripe at the position x_{pin} and depinned from the pinning site at the depinning field H_{depin} .

In changing the polarity of H_{long} and H_{tr} four different measurements could be performed. These four possibilities are schematically shown in Fig. 4.24a-d. If both fields are positive, as depicted in Fig. 4.24a, a HH DW will move from the left side. This measurement is named HH-left for convenience. The three remaining measurements are named accordingly, as it is shown in Fig. 4.24c-d.

4.2.2 Influence of a transverse field on DW pinning.

In a first step the pinning probability was plotted against the pinning positions for zero transverse field. This characterizes the potential for the moving DW, which is induced by the edge roughness of the nanostripe. Fig. 4.25a shows a typical measurement for several samples. The pinning sites are rather weak and distributed randomly over the 200 μm measuring length. Moreover, each of the 4 measurement setups show different pinning sites, reflecting the dependence of the pinning potential on the DW structure [135].

In Fig. 4.25b a sample with two strong pinning sites, which are active for all four measurements, is shown. The pinning sites are located at $x_{pin} \approx 8 \mu\text{m}$ and $x_{pin} \approx 74 \mu\text{m}$. These are used to investigate the influence of an applied transverse field on the pinning process.

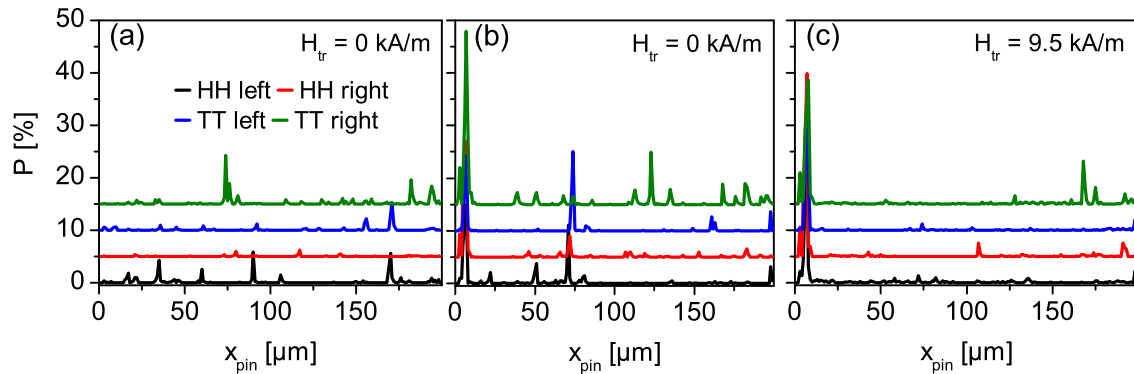


Figure 4.25: (a) Typical plot of the pinning probability as a function of the pinning position x_{pin} for the four different measurement setups explained in Fig. 4.24. (b) Sample with strong pinning sites at $x_{pin} \approx 8 \mu\text{m}$ and $x_{pin} \approx 74 \mu\text{m}$. The transverse field for (a) and (b) is zero for both graphs. (c) shows the data for the same sample used in (b) and for $H_{tr} = 9.5 \text{ kA/m}$. The total number of measurements for each configuration was 1000. The different plots are offset by 5% for clarity.

Fig. 4.25c shows the pinning probability for the same sample used in Fig. 4.25b under the influence of $H_{tr} = 9.5 \text{ kA/m}$. Due to the applied transverse field the pinning site at $x_{pin} \approx 74 \mu\text{m}$ has vanished completely. This is a typical feature for the most pinning site in GMR nanostripes investigated in the course of this thesis. The reason could be the increased DW width as described in section 4.1.5. A wider DW is less influenced by a certain edge roughness of a nanostripe. One finds some weak pinning

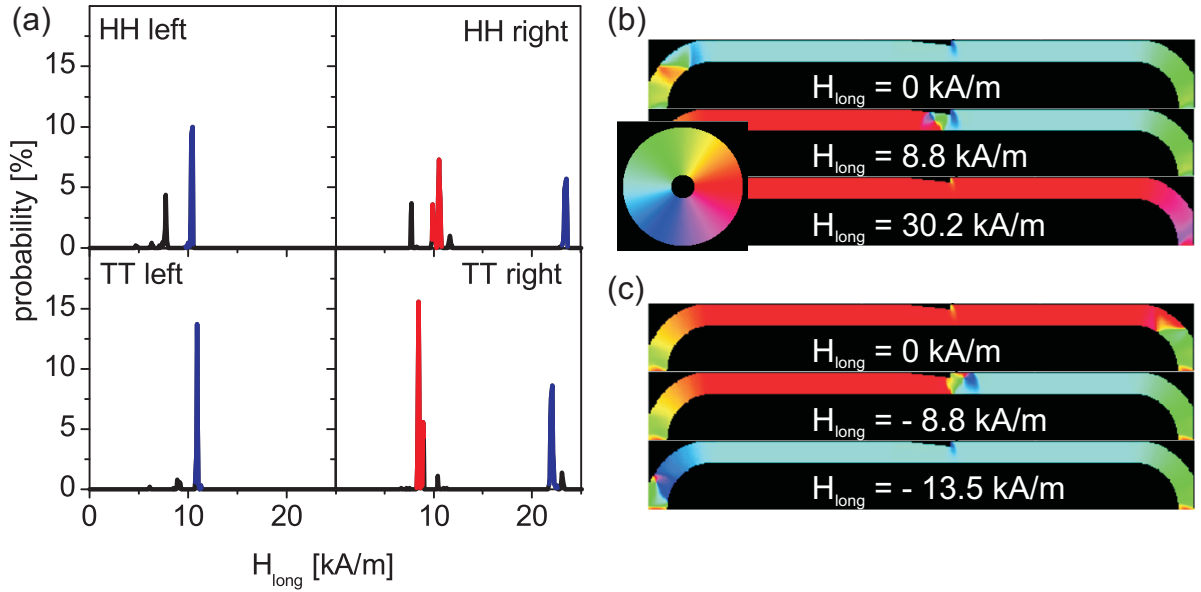


Figure 4.26: (a) Probability plot for the depinning fields from the strong pinning site at $x_{pin} \approx 8 \mu\text{m}$ for the four configurations. (b) and (c) shows micromagnetic simulation of the pinning behavior in a $20 \times 160 \text{ nm}^2$ nanostripe for a DW moving from the left and right, respectively. An artificial notch was introduced as pinning site with a depth of 50 nm.

sites, which are still present for $H_{tr} = 9.5 \text{ kA/m}$. The reason is the decreased injection field (the depinning field from the corner) with increasing transverse field. If the DW is driven by a smaller field and thus moves with a smaller velocity new weak pinning sites could become active. However, for larger transverse fields all weak pinning sites are inactive.

The pinning site at $x_{pin} \approx 8 \mu\text{m}$ is still active for $H_{tr} = 9.5 \text{ kA/m}$ and is used to investigate the influence of a transverse field on the pinning process in more detail. First of all one can examine the depinning fields (the field needed to move the pinned DW away from the defect) for this pinning site. The probability plot of the depinning fields is plotted in Fig. 4.26. For the DW moving from the left towards the pinning sites one finds in principle one main peak at $H_{depin} \approx 10 \text{ kA/m}$. This peak is also found for the measurements with a DW moving from the right side to the defect. Additionally there is a peak at a rather high depinning field of $H_{depin} \approx 23 \text{ kA/m}$.

An asymmetric notch can explain this strong difference of the depinning fields, which depend on the direction the DW is approaching the pinning site. A micromag-

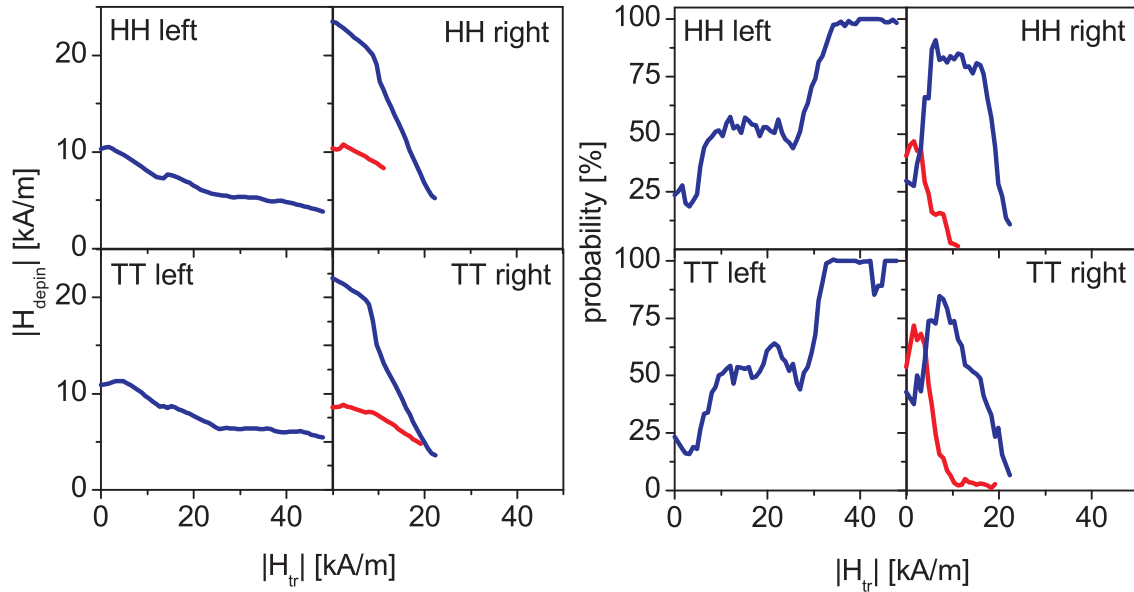


Figure 4.27: Dependence of (a) the depinning field and (b) the pinning probability on the applied transverse field. The blue and the red peaks found in Fig. 4.26a are analyzed.

netic simulation support this assumption. An asymmetric notch with a depth of 50 nm was added to a nanostripe comparable to the one used in the experiment with a cross section of $20 \times 160 \text{ nm}^2$. Two simulations were conducted with a DW moving from the left 4.26b and the right corner 4.26c towards the notch. For the DW approaching from the right corner one finds a depinning field of $H_{depin} = 13.5 \text{ kA/m}$, while a DW from the left corner needs a field of $H_{depin} = 30.2 \text{ kA/m}$ to be depinned from the notch. These values reproduce the one found experimentally quite well.

In a next step the dependence of this depinning fields as well as the pinning probability on the applied transverse field was investigated. The pinning probability was thereby analyzed with respect to the two main depinning fields found in Fig. 4.26a. The results are plotted in Fig. 4.27. The general trend is the decrease of the depinning field with the applied transverse field. Interestingly the higher depinning field decrease very rapidly with H_{tr} , so that for large transverse fields all depinning fields are in the range of 10 kA/m.

The pinning probability shows a behavior which is not expected intuitively. For a DW approaching from the left corner the probability increases in two steps to 100 %, whereby for both steps the probability increase by a factor of two: first from $\approx 25 \%$ to

$\approx 50\%$ at roughly $H_{tr} \approx 7 - 10$ kA/m and than to 100% for a transverse field in the region of $H_{tr} = 20 - 30$ kA/m. These steps can be explained by the preferred pinning of one DW type. In order to reduce the Zeeman energy and because of the suppression of the WBD (see section 4.1.3) the DW will be a TDW with a core magnetization parallel H_{tr} for both measurements, TT and HH left, if a large transverser fields is applied. However, for both measurements from one direction the TDW has the same chirality, because both the TDW core magnetization and the domain magnetizations change. Therefore, one can explain the first step in the probability by a selection of one TDW chirality by means of the transverse field. In other words for $H_{tr} = 0$ a TDW and a VW will arrive with 50% probability due to the stochasticity of the WBD. 50% of these TDWs, arriving at the pinning site, will have the chirality which is pinned at the defect. And the other 50% will have a chirality which moves over the defect without beeing pinned. This would result in a overall pinning probability of the measured 25% . If one applies a transverse field one chirality will be preferred over the other resulting in an increase of the pinning probability. Consequently the second step is due to the suppression of the WBD. As explained in section 4.1.3 a transverse field of sufficient strength will suppress the WBD. Because the periodic change of the DW type stops, the VW will not be present above the suppression of the WBD. The pinning probability will increase to 100% as it is observed in the experiment for $H_{tr} > 20$ kA/m.

For the case of a DW moving from the right corner to the defect we find a slightly different picture. The pinning probability is zero for transverse fields larger than 22 kA/m. This again reflects the asymmetry of the pinning potential created by this defect. The two depinning fields found for this case can be assigned to different DW types, too. The higher depinning field plotted as the blue graph is again the TDW of either chirality, while the red curve represents the depinning field for a vortex wall. With increasing transverse field the probability of a pinned VW decreases. Note that the probability of a pinned VW decreases to zero for smaller transverse fields as compared to the left case. This probability does not imperatively reflect the probability of the VW occurrence. Accurately it is the product of the pinning probability of a VW and the probability of the occurrence of this DW type. Therefore, the pinning probability of the VW is zero, albeit there are still VWs in the nanostripe during DW propagation because $H < H_w$. The same holds for the TDW whose pinning probability decreases to zero for $H_{tr} > 22$ kA/m.

Another evidence of different DW types during the pinning process can be the volt-

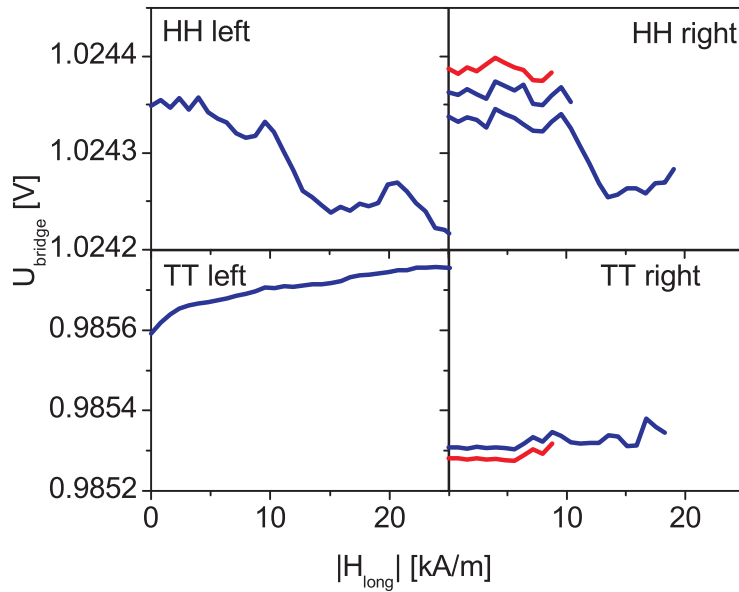


Figure 4.28: Voltage levels of the DWs pinned at the pinning site at $x_{pin} \approx 8 \mu\text{m}$ for the four different measurements depicted in Fig. 4.24a-d.

age level of the half bridge, when a DW is pinned at the defect. The interpretation of these voltage levels is, however, difficult. The GMR depends on the magnetization parallel to the reference direction. In the present measurement the reference direction makes an angle of 45° with the nanostripe long axis. Thus, the MR is sensitive to the x - and the y -magnetization. A change of both, the DW type and the DW position, alters the X_{GMR} .

Fig. 4.28 shows the measured voltage for the pinned DW for zero applied fields. One can find well separated voltage levels for the different DW types. As expected there is only one voltage level for the left case, as there is only the TDW pinned at the defect. The voltage decreases with increasing H_{tr} , which can have two reasons. First a change of the TDW width and second a shift of the DW position in the pinned state. For the HH right case there are three voltage levels which can be attributed to a VW (red) and a TDW with its two chirality (blue). The VW and one chirality of the TDW are not pinned any more for larger transverse fields. The TT right case only shows the VW and one chirality of the TDW. It is possible that both chirality can not be resolved for this case.

4.2.3 Conclusion

In conclusion large transverse fields, which will occur in applications like the multi-turn counter, can have a strong influence on the pinning process of DWs at geometric imperfections. For small pinning sites it was found that a transverse field decrease the pinning probability significantly. If the pinning site is stronger, H_{tr} can influence both, the depinning field and the pinning probability. The first decreases for all cases reported here, while the latter can have difficult dependencies on the transverse field. Due to the selection of one DW type the pinning probability can increase up to 100 %.

Furthermore the presented measurements of the pinning probability allowed for an indirect determination of the DW type, which could be confirmed by analysis of the voltage levels for the pinned DW state.

5 Summary and Outlook

Summary In this thesis the Walker breakdown process, which was predicted by an 1-d model in the 1970s, could be experimentally verified by single shot measurements for the first time [107]. This single shot technique was used to characterize this process in more detail. The prediction by Lee et al. [67], who reported the traces of the vortex and antivortex during this process could be proven. In a 1 μm wide nanostripe the single shot measurements clearly showed first a back- and then a forward movement which is a clear evidence for the occurrence of a vortex during the WBD. The influence of a transverse field on this process was investigated, too. It could be shown that with increasing H_{tr} the Walker frequency decreases for all nanostripe width. Above a critical transverse field in the range of $H_{tr}/H_k^y = 0.3 - 0.45$ the WBD was suppressed. The present 1-d theory of Wang et al. [39], which includes a H_{tr} of arbitrary angle, cannot explain the observed data. This is, however, not surprising because the theory is valid for smaller nanostripes as compared to those used in these experiments.

With the help of the single shot technique a new mode of DW dynamics was discovered: a dynamically stable, split DW [108]. The DW is stretched over several μm along the nanostripe because the two HAVs constituting the TDW, behave as independent quasiparticles. The reasons for this mode could be explained by analyzing the different torques acting on the magnetization during DW movement.

The largest part of this work dealt with the impact of an in-plane transverse field on both the DW dynamics as well as the DW statics. Concerning the DW dynamics, one can generally conclude that a transverse field increases the DW mobility [109], due to the wider DW and decreased DW angle (given the most likely parallel alignment of H_{tr} and M_{core}). This was shown for both, $H < H_w$ and $H > H_w$. These findings could be, at least partially, explained using a 1-d model developed by Bryan et al. [37]. It was found that for small H_{tr} the DW mobility rises in a first approximation linearly. For larger H_{tr} (in this paper below the WBD) the mobility increased much stronger. As this nonlinear rise for large H_{tr} was found to be the same in two different nanostripes,

it seems to be a fundamental impact of H_{tr} on the mobility.

Beside the DW dynamics, the influence of H_{tr} on DW pinning was investigated, too. It could be shown that the pinning probability for weak pinning sites falls to zero with increasing H_{tr} . For a strong pinning site the dependence of both, the pinning probability and the depinning field, was investigated in dependence on H_{tr} . The pinning probability increased up to 100% for large H_{tr} . A selection of one DW type via the transverse field was suggested as the reason for this drastic increase. For all types of DW observed in this experiment, the depinning field was found to decrease.

Another outcome of this thesis is the surprising occurrence of different Walker fields in the same sample. Depending on the magnetization configuration inside the TDW [110] a change in the Walker field by roughly 10% was found. It was shown that a trapezoid cross section influences the dynamics significantly, leading to these different Walker fields. The reason for this influence stems from the demagnetizing energy in the edge region, which is generated by the DW core region.

With regard to potential applications using a rotating magnetic field for DW control, the outcome of this thesis is of great importance. First of all large H_{tr} increase the DW mobility by a factor of >20 . This allows for a larger operation frequency of the devices. Equally positive is the suppression of the WBD above a critical transverse field. As a consequence only one DW type is present during the movement, the transverse DW with a defined chirality. This reduces the variety of DW behavior at pinning sites. However, this selection could, in principle, increase the pinning probability of a DW at a strong pinning site. Nevertheless, such an unwanted pinning site was only found once in roughly 0.4 μm of investigated GMR nanostripe length. This is 2.5 billion times the nanostripe width.

Outlook Beside the above explained outcome of this thesis there are still lots of open questions concerning field driven DW dynamics. One interesting and important experiment is the DW motion under the influence of arbitrary longitudinal and transverse field, i.e. by using pulse magnetic fields to nucleate or move DW in nanostripe. This has been used in several experiments, however, to the author's knowledge pulse fields and the GMR single shot technique have not yet been combined. This combination would allow a more detailed analysis of the DW dynamics under the influence of both H_{long} and H_{tr} .

Additionally, a systematic study of the DW dynamics in nanostripes of arbitrary

width and thickness would be of great interest. Moriya et al. investigated the influence of the nanostripe dimensions on the Walker field, the Walker frequency and the low field mobility [33]. However, the characterization of the WBD in nanostripes of different dimensions by means of single shot measurements would help to understand this process even more. An experimental phase diagram, comparable to the one predicted by micromagnetic simulations [67], could be one of the next issues, addressed by the single shot technique.

In this thesis the underlying layers as well as the edge roughness were said to influence the DW dynamics in the Py layer. But the mechanism and the amount of the interaction are not yet understood. For this purpose one could change the composition of the AAF (e.g. layer thicknesses) in order to change the total moment of the AAF. By comparing nanostripes with nominal equal dimensions, but different under layers, one may derive the impact of the layers beneath the Py on the DW behavior. Furthermore nanostripes of defined edge roughness, like it was done by Chiang et al. [36] in a first experiment, would be an useful tool to investigate the DW dynamics under the influence of an edge roughness.

Accompanying to these experiments a systematic study by micromagnetic simulations is essential in order to understand the experimental findings. The GMR technique is a powerful tool to discover new types of DW dynamics, however, one needs micromagnetic simulations to interpret and explains these new modes.

Bibliography

- [1] Sixtus K. and Tonks L., Propagation of large Barkhausen discontinuities, *Physical Review*, **37**, 930 (1931)
- [2] Sixtus K. and Tonks L., Propagation of large Barkhausen discontinuities. ii, *Physical Review*, **42**, 419 (1932)
- [3] Spain R., Domain tip propagation logic, *IEEE Transactions on Magnetics*, **2**, 347 (1966)
- [4] Spain R. and Marino M., Magnetic film domain-wall motion devices, *IEEE Transactions on Magnetics*, **6**, 451 (1970)
- [5] Ono T., Miyajima H., Shigeto K., and Shinjo T., Magnetization reversal in sub-micron magnetic wire studied by using giant magnetoresistance effect, *Appl. Phys. Lett.*, **72**, 1116 (1998)
- [6] Ono T., Miyajima H., Shigeto K., Mibu K., Hosoi N., and Shinjo T., Propagation of a magnetic domain wall in a submicrometer magnetic wire, *Science*, **284**, 468 (1999)
- [7] Allwood D.A., Xiong G., Cooke M.D., Faulkner C.C., Atkinson D., Vernier N., and Cowburn R.P., Submicrometer ferromagnetic not gate and shift register, *Science*, **296**, 2003 (2002)
- [8] Allwood D.A., Xiong G., Faulkner C.C., Atkinson D., Petit D., and Cowburn R.P., Magnetic domain-wall logic, *Science*, **309**, 1688 (2005)
- [9] Parkin S.S.P., Hayashi M., and Thomas L., Magnetic domain-wall racetrack memory, *Science*, **320**, 190 (2008)

- [10] Grollier J., Lacour L., Gros V., Hamzic A., Vaures A., Fert A., Adam D., and Faini G., Switching the magnetic configuration of a spin valve by current-induced domain wall motion, *J. Appl. Phys.*, **92**, 4825 (2002)
- [11] Tsoi M., Fontana R.E., and Parkin S.S.P., Magnetic domain wall motion triggered by an electric current, *Appl. Phys. Lett.*, **83**, 2617 (2003)
- [12] Yamaguchi A., Ono T., Nasu S., Miyake K., Mibu K., and Shinjo T., Real-space observation of current-driven domain wall motion in submicron magnetic wires, *Phys. Rev. Lett.*, **92**, 077205 (2004)
- [13] Yamanouchi M., Chiba D., Matsukura F., and Ohno H., Current-induced domain-wall switching in a ferromagnetic semiconductor structure, *Nature*, **428**, 539 (2004)
- [14] Kläui M., Vaz C.A.F., Bland J.A.C., Wernsdorfer W., Faini G., Cambril E., Heyderman L.J., Nolting F., and Rüdiger U., Controlled and reproducible domain wall displacement by current pulses injected into ferromagnetic ring structures, *Phys. Rev. Lett.*, **94**, 106601 (2005)
- [15] Hayashi M., Thomas L., Rettner C., Moriya R., Bazaliy Y.B., and Parkin S.S.P., Current driven domain wall velocities exceeding the spin angular momentum transfer rate in permalloy nanowires, *Phys. Rev. Lett.*, **98**, 037204 (2007)
- [16] Donolato M., Vavassori P., Gobbi M., Deryabina M., Hansen M.F., Metlushko V., Ilic B., Cantoni M., Petti D., Brivio S., and Bertacco R., On-chip manipulation of protein-coated magnetic beads via domain-wall conduits, *Adv. Mater.*, **22**, 2706 (2010)
- [17] Bryan M.T., Dean J., Schrefl T., Thompson F.E., Haycock J., and Allwood D.A., The effect of trapping superparamagnetic beads on domain wall motion, *Applied Physics Letters*, **96**, 192503 (2010)
- [18] Glathe S., Beinersdorf J., Henkel T., Müller R., Julich S., Hübner U., and Mattheis R., Nanobead manipulation using domain walls in ferromagnetic conduits, in *Intermag Conference Taipeh 04/2011*, AG-04
- [19] Novotechnik, RSM2800 (2011), URL <http://www.novotechnik.de/>

- [20] Diegel M., Mattheis R., and Halder E., Multiturn counter using movement and storage of 180° magnetic domain walls, *Sens. Lett.*, **5**, 118 (2007)
- [21] Diegel M., Glathe S., Mattheis R., Scherzinger M., and Halder E., A new for bit magnetic domain wall based multiturn counter, *IEEE T. Magn.*, **45**, 3792 (2009)
- [22] Atkinson D., Allwood D.A., Xiong G., Cooke M.D., Faulkner C.C., and Cowburn R.P., Magnetic domain-wall dynamics in a submicrometre ferromagnetic structure, *Nat. Mater.*, **2**, 85 (2003)
- [23] Beach G.S.D., Nistor C., Knutson C., Tsoi M., and Erskine J.L., Dynamics of field-driven domain-wall propagation in ferromagnetic nanowires, *Nat. Mater.*, **4**, 741 (2005)
- [24] Hayashi M., Thomas L., Rettner C., Moriya R., and Parkin S., Direct observation of coherent precession of magnetic domain walls propagating along permalloy nanowires, *Nature Physics*, **3**, 21 (2007)
- [25] Hayashi M., Thomas L., Rettner C., Moriya R., and Parkin S.S.P., Real time observation of the field driven periodic transformation of domain walls in permalloy nanowires at the larmor frequency and its first harmonic, *Appl. Phys. Lett.*, **92**, 112510 (2008)
- [26] Kondou K., Ohshima N., Kasai S., Nakatani Y., and Ono T., Single shot detection of the magnetic domain wall motion by using tunnel magnetoresistance effect, *Appl. Phys. Express*, **1**, 061302 (2008)
- [27] Möhrke P., Moore T.A., Kläui M., Boneberg J., Backes D., Krzyk S., Heyderman L.J., Leiderer P., and Rüdiger U., Single shot kerr magnetometer for observing real-time domain wall motion in permalloy nanowires, *J. Phys. D: Appl. Phys.*, **41**, 164009 (2008)
- [28] Weerts K., Neutens P., Lagae L., and Borghs G., Influence of pulse amplitude and rise time on field-induced domain wall propagation in Ni₈₀Fe₂₀ nanowires, *J. Appl. Phys.*, **103**, 094307 (2008)
- [29] Yang J., Nistor C., Beach G.S.D., and Erskine J.L., Magnetic domain-wall velocity oscillations in permalloy nanowires, *Phys. Rev. B*, **77**, 014413 (2008)

- [30] Bergman B., Moriya R., Hayashi M., Thomas L., Tyberg C., Lu Y., Joseph E., Rothwell M.B., Hummel J., Gallagher W.J., Koopmans B., and Parkin S.S.P., Generation of local magnetic fields at megahertz rates for the study of domain wall propagation in magnetic nanowires, *Appl. Phys. Lett.*, **95**, 262503 (2009)
- [31] Rhensius J., Heyne L., Backes D., Krzyk S., Heyderman L.J., Joly L., Nolting F., and Kläui M., Imaging of domain wall inertia in permalloy half-ring nanowires by time-resolved photoemission electron microscopy, *Phys. Rev. Lett.*, **104**, 067201 (2010)
- [32] Jiang X., Thomas L., Moriya R., Hayashi M., Bergman B., Rettner C., and Parkin S.S., Enhanced stochasticity of domain wall motion in magnetic race-tracks due to dynamic pinning, *Nat Commun*, **1**, 25 (2010)
- [33] Moriya R., Hayashi M., Thomas L., Rettner C., and Parkin S.S.P., Dependence of field driven domain wall velocity on cross-sectional area in NiFeCo nanowires, *Appl. Phys. Lett.*, **97**, 142506 (2010)
- [34] Weerts K., Roy W.V., Borghs G., and Lagae L., Suppression of complex domain wall behavior in Ni₈₀Fe₂₀ nanowires by oscillating magnetic fields, *Applied Physics Letters*, **96**, 062502 (2010)
- [35] Lewis E.R., Petit D., O'Brien L., Fernandez-Pacheco A., Sampaio J., Jausovec A.V., Zeng H.T., Read D.E., and Cowburn R.P., Fast domain wall motion in magnetic comb structures, *Nat Mater*, **9**, 980 (2010)
- [36] Chiang T.W., Chang L.J., Yu C., Huang S.Y., Chen D.C., Yao Y.D., and Lee S.F., Demonstration of edge roughness effect on the magnetization reversal of spin valve submicron wires, *Appl. Phys. Lett.*, **97**, 022109 (2010)
- [37] Bryan M.T., Schreffl T., Atkinson D., and Allwood D.A., Magnetic domain wall propagation in nanowires under transverse magnetic fields, *J. Appl. Phys.*, **103**, 073906 (2008)
- [38] Kunz A. and Reiff S.C., Enhancing domain wall speed in nanowires with transverse magnetic fields, *J. Appl. Phys.*, **103**, 07D903 (2008)
- [39] Lu J. and Wang X., Motion of transverse domain walls in thin magnetic nanostripes under transverse magnetic fields, *J. Appl. Phys.*, **107**, 083915 (2010)

-
- [40] Weiss P., Molekulares Feld und Ferromagnetismus, *Phys. Zs.*, **9**, 358 (1908)
- [41] Ising E., Beitrag zur Theorie des Ferromagnetismus, *Z. f. Physik*, **31**, 253 (1925)
- [42] Heisenberg W., Zur theorie des ferromagnetismus, *Z. f. Physik*, **49**, 619 (1928)
- [43] Bloch F., Zur Theorie des Austauschproblems und der Remanenzerscheinung der Ferromagnetika, *Zeits. f. Physik*, **74**, 295 (1932)
- [44] Landau L. and Lifshits E., On the theory of the dispersion of magnetic permeability in ferromagnetic bodies, *Physikalische Zeitschrift der Sowjetunion*, **8**, 153 (1935)
- [45] Hubert A. and Schäfer R., *Magnetic Domains*, Springer, Berlin (1998)
- [46] Hellwege K.H. and Hellwege A.M., *Landolt and Börnstein: II. Band, 9. Teil Magnetische Eigenschaften I*, Springer (1962)
- [47] Stöhr J. and Siegmann H., *Magnetism: From fundamentals to nanoscale dynamics*, Springer, Berlin (2006)
- [48] Thiaville A. and Nakatani Y., *Spin Dynamics in Confined Magnetic Structures III*, chapter Domain wall dynamics in nanowires and nanostrips, p. 161, Springer, New York (2006)
- [49] Nibarger J.P., Lopusnik R., Celinski Z., and Silva T.J., Variation of magnetization and the landé g factor with thickness in Ni-Fe films, *Appl. Phys. Lett.*, **83**, 93 (2003)
- [50] Gilbert T.L., A lagrangian formulation of the gyromagnetic equation of the magnetic field, *Phys. Rev.*, **100**, 1243 (1955)
- [51] Gilbert T.L., A phenomenological theory of damping in ferromagnetic materials, *IEEE T. Magn.*, **40**, 3443 (2004)
- [52] Berkov D.V. and Gorn N.L., Micromagus: package for micromagnetic simulations, <http://www.micromagus.de>
- [53] Kittel C., Physical theory of ferromagnetic domains, *Rev. Mod. Phys.*, **21**, 541 (1949)

- [54] Porter D.G. and Donahue M.J., Velocity of transverse domain wall motion along thin, narrow strips, *J. Appl. Phys.*, **95**, 6729 (2004)
- [55] McMichael R.D. and Donahue M., Head to head domain wall structures in thin magnetic strips, *IEEE T. Magn.*, **33**, 4167 (1997)
- [56] Nakatani Y., Thiaville A., and Miltat J., Head-to-head domain walls in soft nano-strips: a refined phase diagram, *J. Magn. Magn. Mater.*, **290**, 750 (2005)
- [57] Laufenberg M., Kläui M., Backes D., Bühner W., Ehrke H., Bedau D., Rüdiger U., Nolting F., Heyderman L.J., Cherifi S., Locatelli A., Belkhou R., Heun S., Vaz C.A.F., Bland J.A.C., Kasama T., Dunin-Borkowski R.E., Pavlovska A., and Bauer E., Domain wall spin structures in 3d metal ferromagnetic nanostructures, *Adv. in Solid State Phys.*, **46**, 281 (2008)
- [58] Rothman J., Kläui M., Lopez-Diaz L., Vaz C.A.F., Bleloch A., Bland J.A.C., Cui Z., and Speaks R., Observation of a bi-domain state and nucleation free switching in mesoscopic ring magnets, *Phys. Rev. Lett.*, **86**, 1098 (2001)
- [59] Kläui M., Head-to-head domain walls in magnetic nanostructures, *J. Phys.: Condens. Matter*, **20**, 313001 (2008)
- [60] Tonomura A., Electron-holographic interference microscopy, *Advances in Physics*, **41**, 59 (1992)
- [61] Stöhr J., Wu Y., Hermsmeider B.D., Samant M.G., Harp G.R., Koranda S., Dunham D., and Tonner B.P., Element-specific magnetic microscopy with circularly polarized x-rays, *Science*, **259**, 658 (1993)
- [62] Tchernyshyov O. and Chern G.W., Fractional vortices and composite domain walls in flat nanomagnets, *Phys. Rev. Lett.*, **95**, 197204 (2005)
- [63] Chern G.W., Youk H., and Tchernyshyov O., Topological defects in flat nanomagnets: The magnetostatic limit, *J. Appl. Phys.*, **99**, 08Q505 (2006)
- [64] Youk H., Chern G.W., Merit K., Oppenheimer B., and Tchernyshyov O., Composite domain walls in flat nanomagnets: The magnetostatic limit, *J. Appl. Phys.*, **99**, 08B101 (2006)

- [65] Schryer N.L. and Walker L.R., The motion of 180° domain walls in uniform dc magnetic fields, *J. Appl. Phys.*, **45**, 5406 (1974)
- [66] Choi Y.S., Lee J.Y., Yoo M.W., Lee K.S., Guslienko K.Y., and Kim S.K., Critical nucleation size of vortex core for domain wall transformation in soft magnetic thin film nanostrips, *Phys. Rev. B*, **80**, 012402 (2009)
- [67] Lee J.Y., Lee K.S., Choi S., Guslienko K.Y., and Kim S.K., Dynamic transformations of the internal structure of a moving domain wall in magnetic nanostripes, *Phys. Rev. B*, **76**, 184408 (2007)
- [68] Malozemoff A.P. and Slonczewski J., *Magnetic Domain Walls in Bubble Materials*, Academic Press (new York) (1979)
- [69] Binasch G., Grünberg P., Saurenbach F., and Zinn W., Enhanced magnetoresistance in layered magnetic structures with antiferromagnetic interlayer exchange, *Phys. Rev. B*, **39**, 4828 (1989)
- [70] Baibich M.N., Broto J.M., Fert A., Van Dau F.N., Petroff F., Etienne P., Creuzet G., Friederich A., and Chazelas J., Giant magnetoresistance of (001)Fe/(001)Cr magnetic superlattices, *Phys. Rev. Lett.*, **61**, 2472 (1988)
- [71] Levy P.M., Zhang S., and Fert A., Electrical conductivity of magnetic multilayered structures, *Phys. Rev. Lett.*, **65**, 1643 (1990)
- [72] Valet T. and Fert A., Theory of the perpendicular magnetoresistance in magnetic multilayers, *Phys. Rev. B*, **48**, 7099 (1993)
- [73] Camley R.E. and Barnasacute J., Theory of giant magnetoresistance effects in magnetic layered structures with antiferromagnetic coupling, *Phys. Rev. Lett.*, **63**, 664 (1989)
- [74] Hirota E., Sakakima H., and Inomata K., *Giant Magnetoresistance devices*, Springer (2002)
- [75] Erekhinsky M., Sharoni A., Casanova F., and Schuller I.K., Surface enhanced spin-flip scattering in lateral spin valves, *Appl. Phys. Lett.*, **96**, 022513 (2010)
- [76] Mott N.F., The electrical conductivity of transition metals, *Proc. Roy. Soc.*, **153**, 699 (1936)

- [77] Thomson W., On the electrodynamic qualities of metals: effect of magnetization on the electric conductivity of nickel and iron, *Proc. Roy. Soc.*, **8**, 546 (1857)
- [78] Tumanski S., *Thin film magnetoresistive sensors*, Institute of Physics Publishing (2001)
- [79] Meiklejohn W.H. and Bean C.P., New magnetic anisotropy, *Phys. Rev.*, **102**, 1413 (1956)
- [80] Meiklejohn W.H. and Bean C.P., New magnetic anisotropy, *Phys. Rev.*, **105**, 904 (1957)
- [81] Meiklejohn W.H., Exchange anisotropy—a review, *J. Appl. Phys.*, **33**, 1328 (1962)
- [82] Fulcomer E. and Charap S.H., Thermal fluctuation aftereffect model for some systems with ferromagnetic-antiferromagnetic coupling, *J. Appl. Phys.*, **43**, 4190 (1972)
- [83] Stiles M.D. and McMichael R.D., Model for exchange bias in polycrystalline ferromagnet-antiferromagnet bilayers, *Phys. Rev. B*, **59**, 3722 (1999)
- [84] Fujiwara H., Hou C., Sun M., Cho H., and Nishioka K., Effect of exchange coupling of polycrystalline antiferromagnetic layers on the magnetization behavior of soft magnetic layers, *IEEE Transactions on Magnetics*, **35**, 3082 (1999)
- [85] Malozemoff A.P., Heisenberg-to-ising crossover in a random-field model with uniaxial anisotropy, *Phys. Rev. B*, **37**, 7673 (1988)
- [86] Malozemoff A.P., Mechanisms of exchange anisotropy (invited), *J. Appl. Phys.*, **63**, 3874 (1988)
- [87] Malozemoff A.P., Random-field model of exchange anisotropy at rough ferromagnetic-antiferromagnetic interfaces, *Phys. Rev. B*, **35**, 3679 (1987)
- [88] Parkin S.S.P., More N., and Roche K.P., Oscillations in exchange coupling and magnetoresistance in metallic superlattice structures: Co/Ru, Co/Cr, and Fe/Cr, *Phys. Rev. Lett.*, **64**, 2304 (1990)

-
- [89] Parkin S.S.P. and Mauri D., Spin engineering: Direct determination of the Ruderman-Kittel-Kasuya-Yosida far-field range function in ruthenium, *Phys. Rev. B*, **44**, 7131 (1991)
- [90] Hartmann U., ed., *Magnetic Multilayers and Giant Magnetoresistance*, Springer (1999)
- [91] Jones B.A., Theory of exchange coupling in magnetic multilayers, *IBM J. Res. Dev.*, **42**, 25 (1998)
- [92] Bruno P., Theory of interlayer magnetic coupling, *Phys. Rev. B*, **52**, 411 (1995)
- [93] Shinjo T. and Yamamoto H., Large magnetoresistance of field-induced giant ferrimagnetic multilayers, *J. Phys. Soc. Jpn.*, **59**, 3061 (1990)
- [94] Dieny B., Szeles V.S., Parkin S.S.P., Gurney B.A., Wilhoit D.R., and Mauri D., Giant magnetoresistance in soft ferromagnetic multilayers, *Phys. Rev. B*, **43**, 1297 (1991)
- [95] van den Berg H., Clemens W., Gieres G., Rupp G., Schelter W., and Vieth M., Gmr sensor scheme with artificial antiferromagnetic subsystem, *IEEE T. Magn.*, **32**, 4624 (1996)
- [96] Leal J.L. and Kryder M.H., Spin valves exchange biased by Co/Ru/Co synthetic antiferromagnets, *J. Appl. Phys.*, **83**, 3720 (1998)
- [97] Kief M.T., Bresowar J., and Leng Q., Exchange coupling in sputtered giant magnetoresistance NiFe/Cu/CoFe/Cu multilayers, *J. Appl. Phys.*, **79**, 4766 (1996)
- [98] Parkin S.S.P., Origin of enhanced magnetoresistance of magnetic multilayers: Spin-dependent scattering from magnetic interface states, *Phys. Rev. Lett.*, **71**, 1641 (1993)
- [99] The samples were fabricated at the Institute of Photonic Technology Jena e.V.. The stacks were deposited by K. Kirsch and the patterning was conducted by U. Hübner.
- [100] The samples were fabricated by J. Paul at Sensitec / Mainz.

- [101] The preparation of the TEM lamella and the TEM imaging was performed by N. Schamelt and D. Hesse at the Institute of Microstructure Physics / Halle.
- [102] Wen C.P., Coplanar waveguide: A surface strip transmission line suitable for nonreciprocal gyromagnetic device applications, *IEEE Transactions on Microwave Theory And Techniques*, **12**, 1087 (1969)
- [103] Jahn S., Margraf M., Habchi V., and Jacob R., Qucs - technical paper (2011), URL <http://qucs.sourceforge.net/tech/node85.html>
- [104] Qiu Z.Q. and Bader S.D., Surface magneto-optic kerr effect, *Rev. Sci. Instrum.*, **71**, 1243 (2000)
- [105] Nakatani Y., Thiaville A., and Miltat J., Faster magnetic walls in rough wires, *Nat. Mater.*, **2**, 521 (2003)
- [106] Kim S.K., Lee J.Y., Choi Y.S., Guslienko K.Y., and Lee K.S., Underlying mechanism of domain-wall motions in soft magnetic thin-film nanostripes beyond the velocity-breakdown regime, *Applied Physics Letters*, **93**, 052503 (2008)
- [107] Glathe S., Mattheis R., and Berkov D.V., Direct observation and control of the walker breakdown process during a field driven domain wall motion, *Appl. Phys. Lett.*, **93**, 072508 (2008)
- [108] Glathe S., Zeisberger M., Hübner U., and Mattheis R., Splitting of a moving transverse domain wall in a magnetic nanostripes in a transverse field, *Phys. Rev. B*, **81**, 020412(R) (2010)
- [109] Glathe S., Berkov I., Mikolajick T., and Mattheis R., Experimental study of domain wall motion in long nanostrips under the influence of a transverse field, *Appl. Phys. Lett.*, **93**, 162505 (2008)
- [110] Glathe S., Zeisberger M., Mattheis R., and Hesse D., Influence of slanted nanostripe edges on the dynamics of magnetic domain walls, *Applied Physics Letters*, **97**, 112508 (2010)
- [111] ADR36x, *Low Power; Low Noise Voltage References with Sink/Source Capability*, URL <http://www.analog.com>

- [112] Heyne L., Rhensius J., Cho Y.J., Bedau D., Krzyk S., Dette C., Körner H.S., Fischer J., Laufenberg M., Backes D., Heyderman L.J., Joly L., Nolting F., Tatara G., Kohno H., Seo S., Rüdiger U., and Kläui M., Geometry-dependent scaling of critical current densities for current-induced domain wall motion and transformations, *Phys. Rev. B*, **80**, 184405 (2009)
- [113] Kim S.K., Lee J.Y., Choi Y.S., Guslienko K.Y., and Lee K.S., Underlying mechanism of domain-wall motions in soft magnetic thin-film nanostripes beyond the velocity-breakdown regime, *Appl. Phys. Lett.*, **93**, 052503 (2008)
- [114] Martinez E., Lopez-Diaz L., Torres L., Tristan C., and Alejos O., Thermal effects in domain wall motion: Micromagnetic simulations and analytical model, *Phys. Rev. B*, **75**, 174409 (2007)
- [115] Kunz A., Simulated domain wall dynamics in magnetic nanowires, *J. Appl. Phys.*, **99**, 08G107 (2006)
- [116] Kunz A., Simulating the maximum domain wall speed in a magnetic nanowire, *IEEE Transactions on Magnetics*, **42**, 3219 (2006)
- [117] Bryan M., Schrefl T., and Allwood D., Dependence of transverse domain wall dynamics on permalloy nanowire dimensions, *IEEE Transactions on Magnetics*, **46**, 1135 (2010)
- [118] Park C.M. and Bain J., Local degradation of magnetic properties in magnetic thin films irradiated by ga^+ focused-ion-beams, *Magnetics, IEEE Transactions on DOI - 10.1109/TMAG.2002.802681*, **38**, 2237 (2002)
- [119] Mascaro M.D., Nam C., and Ross C.A., Interactions between 180° and 360° domain walls in magnetic multilayer stripes, *Appl. Phys. Lett.*, **96**, 162501 (2010)
- [120] Hamming R.W., *Digital Filters, 3rd edition*, Dover Publications (1997)
- [121] Beach G., Tsoi M., and Erskine J., Current-induced domain wall motion, *J. Magn. Magn. Mater.*, **320**, 1272 (2008)
- [122] Pütter S., Mikuszeit N., Vedmedenko E.Y., and Oepen H.P., The effect of tilted edges on the shape anisotropy and stray field coupling of uniformly magnetized rectangular elements, *J. Appl. Phys.*, **106**, 043916 (2009)

- [123] Maranville B.B., McMichael R.R., and Abraham D.W., Variation of thin film edge magnetic properties with patterning process conditions in ni80fe20 stripes, *Appl. Phys. Lett.*, **90**, 232504 (2007)
- [124] McMichael R.D. and Maranville B.B., Edge saturation fields and dynamic edge modes in ideal and nonideal magnetic film edges, *Phys. Rev. B*, **74**, 024424 (2006)
- [125] Bailleul M., Olligs D., and Fermon C., Micromagnetic phase transitions and spinwave excitations in a ferromagnetic stripe, *Phys. Rev. Lett.*, **91**, 137204 (2003)
- [126] Osborn J.A., Demagnetizing factors of the general ellipsoid, *Phys. Rev.*, **67**, 351 (1945)
- [127] Himeno A., Ono T., Nasu S., Shigeto K., Mibu K., and Shinjo T., Dynamics of a magnetic domain wall in magnetic wires with an artificial neck, *J. Appl. Phys.*, **93**, 8430 (2003)
- [128] Ravelosona D., Lacour D., Katine J.A., Terris B.D., and Chappert C., Nanometer scale observation of high efficiency thermally assisted current-driven domain wall depinning, *Phys. Rev. Lett.*, **95**, 117203 (2005)
- [129] Klaui M., Ehrke H., Rudiger U., Kasama T., Dunin-Borkowski R.E., Backes D., Heyderman L.J., Vaz C.A.F., Bland J.A.C., Faini G., Cambril E., and Wernsdorfer W., Direct observation of domain-wall pinning at nanoscale constrictions, *Appl. Phys. Lett.*, **87**, 102509 (2005)
- [130] Hayashi M., Thomas L., Rettner C., Moriya R., Jiang X., and Parkin S.S.P., Dependence of current and field driven depinning of domain walls on their structure and chirality in permalloy nanowires, *Phys. Rev. Lett.*, **97**, 207205 (2006)
- [131] Tanigawa H., Koyama T., Bartkowiak M., Kasai S., Kobayashi K., Ono T., and Nakatani Y., Dynamical pinning of a domain wall in a magnetic nanowire induced by walker breakdown, *Phys. Rev. Lett.*, **101**, 207203 (2008)
- [132] Bedau D., Kläui M., Hua M.T., Krzyk S., Rüdiger U., Faini G., and Vila L., Quantitative determination of the nonlinear pinning potential for a magnetic domain wall, *Phys. Rev. Lett.*, **101**, 256602 (2008)

- [133] Atkinson D., Eastwood D.S., and Bogart L.K., Controlling domain wall pinning in planar nanowires by selecting domain wall type and its application in a memory concept, *Appl. Phys. Lett.*, **92**, 022510 (2008)
- [134] Eastwood D.S., King J.A., Bogart L.K., Cramman H., and Atkinson D., Chirality-dependent domain wall pinning in a multinotched planar nanowire and chirality preservation using transverse magnetic fields, *J. Appl. Phys.*, **109**, 013903 (2011)
- [135] Bogart L.K., Eastwood D.S., and Atkinson D., The effect of geometrical confinement and chirality on domain wall pinning behavior in planar nanowires, *J. Appl. Phys.*, **104**, 033904 (2008)

Acknowledgements

This thesis, of course, would not be possible without the help of many people during the last years. First of all I want to thank Dr. Mattheis for the opportunity to write my thesis in his group at the IPHT Jena in the field of domain wall dynamics. Beside the excellent facilities in his group Dr. Mattheis was always open for a lot of interesting discussions during the last years. I want to thank Prof. Dr. Seidel for his willingness to supervise my thesis at the University of Jena and for his support during my Ph.D.

For their support at the end of the thesis in terms of proof reading (which is really hard for non-physicists) I want to thank Dr. Mattheis, Prof. Seidel, Björn, Stefan, Matthias, my sister Katja and last but not least Laura.

The Applied Plasmonics group at the IPHT I want to acknowledge for the fantastic working atmosphere including the essential support with sweets for long days at the institute. Here my colleague Sabine Schmidt has to be announced, who was always in care, that we are well supplied with biscuits.

For many helpful discussions and the performing of dynamic simulations I thank M. Zeisberger and D.V. Berkov. Hardy and Dominique, our former electronics technicians, as well as Tom and John, the present ones, I want to thank for the patience in explaining me the electronic world. Especially their support in designing and realizing electronic circuits and measurement setups was extremely helpful for me. In this context I want to acknowledge my colleague Konstantin, too. For sample preparation I want to thank J. Paul (Sensitec), H. Roth, U. Hübner and Konstantin (IPHT). The interesting and unique conversations with Stefan I won't miss in the past three years.

My parents I cannot thank enough for their support throughout my entire life. Without their assistance in many parts of my life, this work would not be possible. Finally I want to thank Laura for her encouragement in hard times and understanding for long lab days. And more generally I am really glad to be on your side Laura.

It is most likely that I forget someone I wanted to thank for some kind of support. However, I think they know that I am very grateful for their support anyway.

Curriculum vitae

Name: Sascha Glathe

Birth: 27.12.1981 in Leipzig, Germany

School education: 34. POS Schule Leipzig, 09/1988 - 07/1992
Werner-Heisenberg-Gymnasium Leipzig, 09/1992 - 07/2000
Abitur 07/2000

University: Electronic and Sensor Materials, TU Freiberg, 10/2001 - 09/2007
Dipl. Ing. 10/2007

Professional Activities: research associate, 10/2007 - 03/2008

Jena, 22.06.2001

Sascha Glathe